

# **Design and Optimization of a Macro-micro Manipulator Featuring a 3-UPS Compliant Parallel Mechanism**

by

Benkai Liang

A Thesis Submitted in Partial Fulfillment  
of the Requirements for the Degree of

Master of Applied Science

in

The Faculty of Engineering and Applied Science  
Mechanical Engineering Program

University of Ontario Institute of Technology

Oct., 2016

© Benkai Liang, 2016

# Abstract

Micromanipulation in microtechnology is highly needed for microfabrication and biomedical applications. Specifically, high manipulation resolution combined with accurate macromotions plays a more crucial role especially in the production of semiconductors, assembly of integrated circuits as well as the accurate manipulation of cells and chromosomes. As a result, it is desired to design such a manipulator to be capable of achieving macro-micro manipulation with high accuracy and high reliability.

This thesis proposes a novel macro-micro manipulator system composed of two different parallel mechanisms which are responsible for the macro motion and the micro manipulation respectively. The macromanipulator is a 3-RRR planar parallel mechanism which has the mobility of 3 DOFs, namely two translational DOFs along  $x$ - and  $y$ -axis and one rotational DOF around the  $z$ -axis while the micromanipulator is a 3-UPS compliant parallel mechanism with an orthogonal structure of 3 translational DOFs.

The work in the thesis covers structural design of the macro-micro manipulator, kinematic modeling and inverse kinematic analysis, formulation of Jacobian matrix; micromanipulator-focused stiffness evaluation, workspace analysis and structural optimization of stiffness and workspace properties.

**Keywords:** Macro-micro manipulator, Micromanipulation, Compliant mechanism, Parallel orthogonal structure, Optimization

# Acknowledgements

First and foremost, I would like to thank my supervisor Dr. Dan Zhang for his guidance in this research, without which my thesis could have never been possible. And it is deemed to be a great honour for me to be able to work with him and have the opportunities to swap ideas and opinions around the problems under study. This is an invaluable experience that will stay in my mind throughout my whole lifetime.

I would also like to express my gratitude to my colleagues in Robotic and Automation Laboratory. Thanks for the time we spent together working in the lab office and making it a very nice environment to study and research.

Last but not least, I am deeply indebted to my family and friends in China for their endless support and encouragement.

# Table of Contents

Abstract.....	ii
Acknowledgements.....	iii
Table of Contents.....	iv
List of Figures.....	vii
List of Tables.....	ix
Nomenclature.....	x
Chapter 1 Introduction.....	1
1.1 Background.....	1
1.1.1 Microtechnology and Micromanipulation.....	1
1.1.2 Parallel Manipulators.....	3
1.1.3 Compliant Mechanisms.....	7
1.2 Literature Review.....	11
1.2.1 Micromanipulator.....	11
1.2.2 Macro-micro Manipulator.....	13
1.3 Contribution and Objective of the Study.....	14
1.4 Organization of the Thesis.....	15
Chapter 2 Inverse Kinematics and Jacobian Analysis.....	17
2.1 Introduction.....	17
2.2 Geometry of the Micromanipulator.....	19
2.3 Kinematic Analysis of the Micromanipulator.....	24
2.3.1 Mobility Analysis.....	24
2.3.2 Inverse Kinematic Analysis.....	26
2.3.3 Jacobian Formulation.....	26
2.4 Geometry of the Macromanipulator.....	27
2.5 Kinematics of the Macromanipulator.....	31
2.5.1 Inverse Kinematic Analysis.....	31
2.5.2 Jacobian Formulation.....	32
2.6 Conclusions.....	34

Chapter 3	Stiffness Analysis	35
3.1	Introduction	35
3.2	Stiffness and Compliance Matrices of Basic Compliant Elements	36
3.3	Stiffness Modeling for One Leg	40
3.3.1	Stiffness Modeling of Compliant Universal Joint	40
3.3.2	Stiffness Modeling of Compliant Translational Joint	41
3.3.3	Stiffness Modeling of Compliant Spherical Joint	42
3.3.4	Stiffness Modeling of One Leg	44
3.4	Stiffness Modeling for 3-UPS CPM	46
3.5	Compliance Mapping	48
3.6	Conclusions	51
Chapter 4	Workspace Evaluation	52
4.1	Introduction	52
4.2	Formulation of Workspace Constraints	53
4.2.1	Constraint Set I: Leg Length Limit	53
4.2.2	Constraint Set II: Compliant Joint Angular Limit	53
4.3	Computer Implementation	54
4.3.1	Formulation of Testing Function	55
4.3.2	Determination of Workspace Search Center and Vector	55
4.3.3	Workspace Boundary Search	57
4.3.4	Workspace Volume Evaluation	58
4.4	Discussion of Results and Plots	60
4.5	Conclusions	63
Chapter 5	Optimization of Micromanipulator	64
5.1	Introduction	64
5.2	Firefly Algorithm	66
5.2.1	Firefly Behaviour and Firefly Algorithm	66
5.2.2	Attractiveness Formulation	67
5.2.3	Distance and Firefly Movement	68
5.2.4	Rationale for Using FA	69

5.3 Stiffness Optimization .....	71
5.3.1 Optimization Criteria .....	71
5.3.2 Variables Selection and Results.....	72
5.4 Workspace Optimization .....	75
5.4.1 Optimization Criteria .....	75
5.4.2 Variables Selection and Results.....	77
5.5 Multi-Objective Optimization.....	78
5.5.1 Necessity for Multi-Objective Optimization .....	78
5.5.2 Implementation of Multi-Objective Optimization .....	79
5.5.3 Results.....	81
5.6 Conclusions.....	83
Chapter 6 Conclusions and Further Study .....	84
6.1 Conclusions.....	84
6.2 Further Study .....	86
References.....	87
Appendix.....	93
A Matlab Code.....	93
B Table of Pareto Optimal Set.....	103

# List of Figures

Figure 1-1: CAD model of the 5-DOF parallel mechanism (by Gabriel Coté).....	4
Figure 1-2: First spatial parallel mechanism (U.S. patent No. 1789680).....	5
Figure 1-3: First spatial industrial parallel robot (U.S. patent No. 2286571).....	5
Figure 1-4: First octahedral hexapod (left, the original Gough platform; right, the Gough platform for tire test).....	6
Figure 1-5: An octahedral hexapod parallel mechanism (U.S. patent No. 3295224).....	6
Figure 1-6: A compliant gripper (Courtesy of the CMRG at Brigham Young University) .....	7
Figure 1-7: Compliant rotational joints [37].....	9
Figure 1-8: Compliant translational joints [37] .....	9
Figure 1-9: Compliant universal joints [37] .....	10
Figure 1-10: Compliant spherical joints [37].....	10
Figure 1-11: CAD models of compliant joints adopted in the study (from left to right: CUJ, CPJ, CSJ) .....	10
Figure 2-1: CAD model of the designed macro-micromanipulator.....	18
Figure 2-2: CAD model of the 3-UPS micromanipulator.....	19
Figure 2-3: Kinematically equivalent model of the micromanipulator by PRB method	20
Figure 2-4: Establishment of the moving coordinate system .....	21
Figure 2-5: Schematic representation of closed vector loop of one leg.....	23
Figure 2-6: CAD Representation of links and joints in one leg.....	25
Figure 2-7: CAD model of the micromanipulator .....	27
Figure 2-8: Schematic representation of the macromanipulator.....	28
Figure 2-9: Schematic diagram of leg 1 for showing the vector loop closure.....	33
Figure 3-1: Basic compliant elements: a cantilever (left) and a right circular hinge (right) .....	37
Figure 3-2: Stiffness modeling of compliant universal joint .....	40
Figure 3-3: Stiffness modeling of upper end of the compliant translational joint.....	41
Figure 3-4: Stiffness modeling of lower end of the compliant translational joint.....	42
Figure 3-5: Stiffness modeling of compliant spherical joint .....	42

Figure 3-6: Stiffness analysis of leg 1 .....	44
Figure 3-7: Compliance mapping of factor $C_{f_x-u_x}$ versus $w$ and $r$ .....	48
Figure 3-8: Compliance mapping of factor $C_{f_y-u_y}$ versus $r$ and $l$ .....	49
Figure 3-9: Compliance mapping of factor $C_{f_z-u_z}$ versus $r$ and $t$ .....	49
Figure 3-10: Compliance mapping of factor $C_{M_x-\theta_x}$ versus $w$ and $l$ .....	50
Figure 3-11: Compliance mapping of factor $C_{M_y-\theta_y}$ versus $l$ and $t$ .....	50
Figure 3-12: Compliance mapping of factor $C_{M_z-\theta_z}$ versus $r$ and $w$ .....	51
Figure 4-1: Definition of workspace search vector .....	56
Figure 4-2: Pseudo code of expanding the search vector .....	57
Figure 4-3: Variation of workspace boundary search vector [75] .....	58
Figure 4-4: Pseudo code of workspace boundary search algorithm [75] .....	58
Figure 4-5: Volume calculation of a sector of workspace .....	59
Figure 4-6: Point cloud of workspace boundary with orientation of $\mathbf{R}_{PRY}(0^\circ, 0^\circ, 0^\circ)$ .....	61
Figure 4-7: Point cloud of workspace boundary with orientation of $\mathbf{R}_{PRY}(5^\circ, 0^\circ, 0^\circ)$ .....	61
Figure 4-8: Point cloud of workspace boundary with orientation of $\mathbf{R}_{PRY}(0^\circ, 5^\circ, 0^\circ)$ .....	62
Figure 4-9: Point cloud of workspace boundary with orientation of $\mathbf{R}_{PRY}(0^\circ, 0^\circ, 5^\circ)$ .....	62
Figure 5-1: Pseudo code of FA [80] .....	67
Figure 5-2: Convergence of global optimums in each generation for stiffness optimization .....	74
Figure 5-3: Convergence of global optimums in each generation for well-conditioned workspace optimization .....	77
Figure 5-4: Pseudo code of multi-objective FA [85] .....	80
Figure 5-5: Plot of Pareto front and initial fireflies in objective space .....	82
Figure 5-6: Pareto front of multi-objective optimization .....	82

# List of Tables

Table 3-1:	Parameters of basic compliance matrix [68].....	38
Table 3-2:	$k_2$ in prismatic beam twisting [68] .....	38
Table 4-1:	Comparison of workspace parameters for different orientations.....	63
Table 5-1:	Comparison of FA with Other Algorithms [80] .....	70

# Nomenclature

$[\cdot]^T$	The transpose of a vector or matrix
$c[\cdot]$	$\cos(\cdot)$
$s[\cdot]$	$\sin(\cdot)$
${}^o[\cdot]$	Items expressed in a local coordinate system $O_i - x_i y_i z_i$
$J$	Jacobian matrix
$c_{ii}$	Diagonal elements of compliance matrix
$\mathbf{I}$	Identity matrix
${}^o\mathbf{R}_p$	Rotation matrix of coordinate system $P-uvw$ with respect to coordinate system $O-xyz$
${}^o\mathbf{R}_G$	Rotation matrix of coordinate system $G-uv$ with respect to coordinate system $O-xy$
$\mathbf{R}_{[]}(\cdot)$	Rotation matrix of rotating angle $\cdot$ around the axis indicated by the subscript [ ]

## Greek Letters

$\mathbf{v}$	Linear velocity of the point on the moving platform
$\boldsymbol{\omega}$	Angular velocity of the moving platform
$\dot{\boldsymbol{\chi}}$	Twist velocity vector of the moving platform
$\theta_i$	Actuating or input joint angles (positive values when measured counterclockwise starting from $x$ -axis direction)
$\alpha_i$	Passive joint angles (positive values when measured counterclockwise)
$\varphi$	Orientation angle of macromanipulator's moving platform

$\alpha$	Randomization parameter of FA
$\beta$	Attractiveness of fireflies of FA
$\gamma$	Absorption coefficient of FA
$\eta_i$	Weight factor for each directional compliance whose relative value characterizes the priority concern of the compliance in corresponding direction
$\kappa_{ii}$	Diagonal elements of stiffness matrix
$\lambda_i$	Weight factor for each directional stiffness whose relative value characterizes the priority of the stiffness in corresponding direction
$\kappa$	Condition number of Jacobian matrix
$\eta$	Global index for a well-conditioned workspace

### **Acronyms**

CMRG	Compliant Mechanism Research Group
CPM	Compliant Parallel Manipulator
CRJ	Compliant Revolutinal Joint
CSJ	Compliant Spherical Joint
CTJ	Compliant Translational Joint
CUJ	Compliant Universal Joint
DOF	Degree of Freedom
EDM	Electrical Discharge Machining
FA	Firefly Algorithm
FEA	Finite Element Analysis
GA	Genetic Algorithm
IC	Integrated Circuit

MEMS Micro-Electro-Mechanical System  
PRB Pseudo-Rigid-Body Method  
PSO Particle Swarm Optimization  
PZT Piezoelectric  
SMA Shape Memory Alloy

# Chapter 1

## Introduction

### 1.1 Background

#### 1.1.1 Microtechnology and Micromanipulation

What is microtechnology? Microtechnology which revolutionizes the ways of manufacturing products and provides more possibilities of what people can do on a micro scale has been receiving more and more attention so far. While conventional industrial production is based on a series of motions such as drilling, milling, grinding, sawing, etc., enabled by large pieces of machinery, in modern electronic manufacturing fields like production of semi-conductors, assembly of integrated circuits and even in biomedical applications such as microsurgery, gene and chromosome manipulation, extremely accurate micro motions in a relatively small workspace are highly needed. It is noted that the micromanipulation plays a vital role in microtechnology applications, which involves

how to handle and manipulate components and structures dexterously at a micrometer level [1].

As electronic devices such as laptops, smart phones and various Apple products are playing a more and more starring role in our modern life, microtechnology and microfabrication as a fundamental prerequisite for that are of great significance in the electronic industry. Microfabrication is a process of fabricating minimal structures of micrometer scale [2], which was originally used for IC fabrication that can be dated back to 1954 when Texas Instruments established the first IC with germanium. From then on, miniaturization technology had advanced rapidly to satisfy the increasing demands on complex integrated circuits. In 1965, Gordon E. Moore ever described an observation that the number of transistors inside a densely arranged IC doubles almost every two years. This trend is still applicable today and in the five decades since that observation, the IC industry has been growing exponentially and had a profound impact on our today's life especially in this information age.[3] Nowadays, IC chips featuring continuously miniaturized size are becoming commercially available, which undoubtedly relies on the progress of microtechnology.

Additionally, microfabrication is also important to the production of MEMS devices. As the manufacturing industry is forwarding itself towards the direction of micrometer dimensions, MEMS presents a promising future for a wide range of applications in terms of functional performances and production costs compared with their macro counterparts. MEMS can be generally defined as miniaturized mechanical or eletro-mechanical elements, namely devices or structures that are created through the techniques of microfabrication.[4] The most notable MEMS elements are the microsensors and

microactuators, which can be appropriately categorized as transducers converting energy from one form to another. Over the past several decades, a drastically large number of microsensors have been developed by MEMS researchers. Surprisingly, although MEMS microactuators are in small size, they are able to generate effects comparable to those at the macro scale level. Then, it goes naturally that their physical dimensions require that the accuracy of the MEMS microfabrication must be guaranteed at a micrometer level.

In conclusion, microtechnology has been the dominant part in promoting the development of microfabrication of IC chips and MEMS devices. To accomplish the micromanipulation with high accuracy on micro scale which is totally different from macro manufacturing process, special micromanipulators must be taken into account with such requirements as micromotions with high precision resolution and fast transfer of the manipulator among different working sites.

### **1.1.2 Parallel Manipulators**

There are various mechanisms existing in the literature and studies. From the perspective of topology, mechanical mechanisms can be classified as serial mechanisms, parallel mechanisms and hybrid mechanisms. In terms of the way of motion transmission, there are mainly two categories, namely traditional rigid-body mechanisms and compliant mechanisms which can be further divided into those with distributed compliance and with concentrated compliance [5]. Based on the advantages of parallel and compliant mechanisms over their counterparts, the concept of parallel compliant mechanism with concentrated compliance is adopted in this thesis and corresponding material will be presented in the current and following subsections.

As Figure 1-1 shows, a parallel manipulator is typically composed of a moving platform which is connected to the fixed base by at least two kinematic chains generally called legs or limbs. The number of legs is typically equal to the number of DOFs of the moving platform such that each leg is actuated and controlled by one actuator and all the actuators are intended to be mounted at or near the fixed base. Compared with serial manipulators which consist of a single kinematic chain with rigid links connected one after another, parallel manipulators can avoid accumulative errors caused by each joint and thus they have higher positioning accuracy. Also, the external load applied to the moving platform can be shared by the actuators and therefore, parallel manipulators possess higher payload capacity and higher structural stiffness. Because of these notable advantages over serial manipulators, they have already received a wide range of applications.

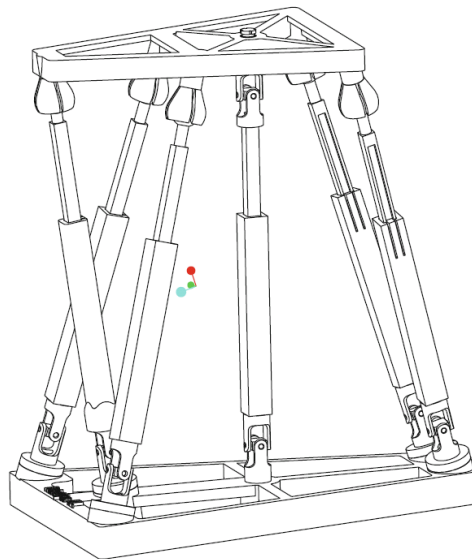


**Figure 1-1: CAD model of the 5-DOF parallel mechanism (by Gabriel Cot'e)**

The first spatial parallel mechanism is perhaps the spherical parallel robot (shown in Figure 1-2) invented by James E. Gwinnet in 1928 as a conceptual entertainment device.

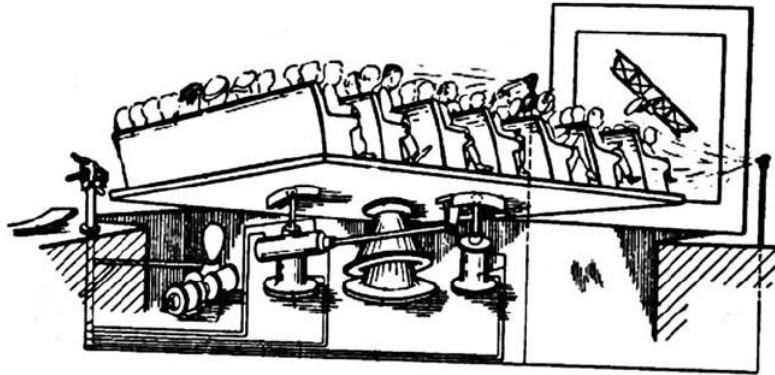


**Figure 1-2: First spatial parallel mechanism (U.S. patent No. 1789680)**

Ten years later after that, Willard L.V. Pollard formulated an original parallel robot for automatic spray painting. This three-legged parallel robot was considered as the first one of industrial application, which features 5 DOFs. Nevertheless, it wasn't built practically and it was Pollard's son, Willard L.V. Pollard Jr. who really designed and engineered the industrial parallel robot as presented in Figure 1-3. In 1947, a new 6-DOF parallel robot, called the first octahedral hexapod was invented by Dr. Eric Gough and deemed to revol-

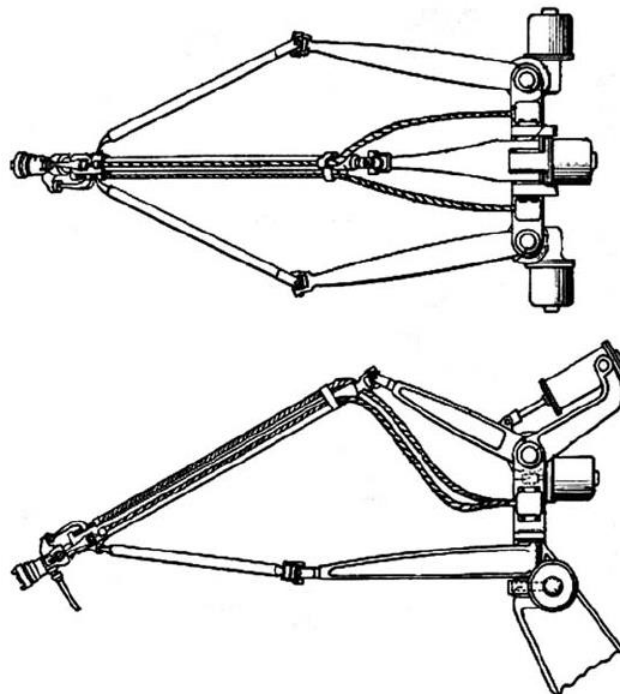


**Figure 1-3: First spatial industrial parallel robot (U.S. patent No. 2286571)**

utionize the robotic industry. It was then applied as a tire-testing equipment (shown in Figure 1-4 left) to discover properties of tires subjected to various loads. Figure 1-4 (right) displays the machine for practical use in 1954. In academia, Stewart published a paper proposing a 6-DOF motion platform that can be used as an aircraft simulator, which was the so-called Stewart platform whose schematic representation can be found in Figure 1-5. This work turned out to be a significant impact on the development of parallel mechanism. Actually it was the contribution of Gough that erected the milestone for the development of industrial parallel robots.



**Figure 1-4: First octahedral hexapod (left, the original Gough platform; right, the Gough platform for tire test)**

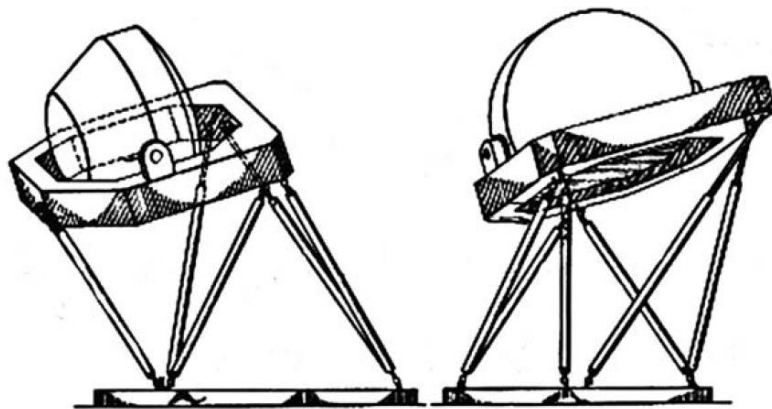


**Figure 1-5: An octahedral hexapod parallel mechanism (U.S. patent No. 3295224)**

Nowadays, parallel robots are receiving wider and wider range of practical applications. Instances being vehicle and aircraft simulators [6]-[10], adjustable articulated trusses [11]-[14], micro-robots [15]-[19], medical devices [20]-[23] and force/torque sensors [24]-[27]. Due to their characteristics of high stiffness and high accuracy, parallel robots have also been adopted in developing high precision machine tools [28]-[31], a typical one of which is the Hexapod machine tool [32],[33].

### 1.1.3 Compliant Mechanisms

Different from traditional rigid-body mechanisms which are composed of rigid links joined by movable joints and derive their motions from relative movement of rigid parts, compliant mechanisms are designed to rely on elastic deformations of flexible elements to obtain their mobility.[34] One example of a compliant gripper is shown in Figure 1-6.



**Figure 1-6: A compliant gripper (Courtesy of the CMRG at Brigham Young University)**

The input force and motion (two ends in the left opening in Figure 1-6) are transferred to the output port (the right opening in Figure 1-6) only by deformation of the flexible structure and a portion of input energy is stored in the flexible members as strain energy. This kind of compliant mechanism possesses distributed compliance and they accomplish the mobility entirely through the deformation of elastic elements. The other kind of

compliant mechanism with concentrated compliance features compliant joints that connect the rigid link to another. They behave much like classic rigid-link mechanisms owing to the fact that the kinematic movable joints are replaced by flexural hinges.[5] Also, they have advantages of both rigid-body mechanisms and compliant mechanisms, one being simplified analysis process by using pseudo-rigid-body method. [35]

Compliant mechanisms have a lot of advantages which make them suitable for many particular applications, in terms of cost reduction and better performances over their rigid-body counterparts. Since compliant mechanisms usually have a monolithic structure which can be fabricated from injection-moldable material or through advanced manufacturing technologies such as EDM and laser cutting, there is a dramatic reduction of required parts and shortened assembly time. Also, the manufacturing process can be largely simplified. Most importantly, they possess many improved performances compared with rigid-body mechanisms. The use of compliant elements which utilize the deflection to transfer motion, force and energy, removes the need for lubrication and eliminates mechanical friction and backlash. As a result, these features help to achieve high-precision in controlling their motions even on a micro or nano scale. Particularly, such precision is crucial to micro and nano manipulator designs. This is also why the compliant joints are adopted in this study.

Compliant joints, or flexural hinges are actually compliant elements and act as the same function as movable joints. But distinct from conventional movable joints, flexural hinges utilize inherent compliance or elastic deformation of material that complies with Hook's law to achieve their function. Resulting from the elimination of mechanical friction, backlash and wear, sub-micron accuracy can be easily reached, which is why

they are important to micro and nano manipulators. According to different motion types that compliant joints allow, there are mainly four classifications: CRJ (see Figure 1-7), CTJ (see Figure 1-8), CUJ (Figure 1-9), and CSJ (Figure 1-10). To design and select proper compliant joints for a specific application, a set of criteria have been mentioned for benchmark [36]: (i) the range of motion, (ii) the amount of axis drift, (iii) the ratio of off-axis stiffness to axial stiffness and (iv) stress concentration effects. Based on these considerations, proper compliant joints of CUS, CTJ, CSJ are selected for this thesis as shown in Figure 1-11.

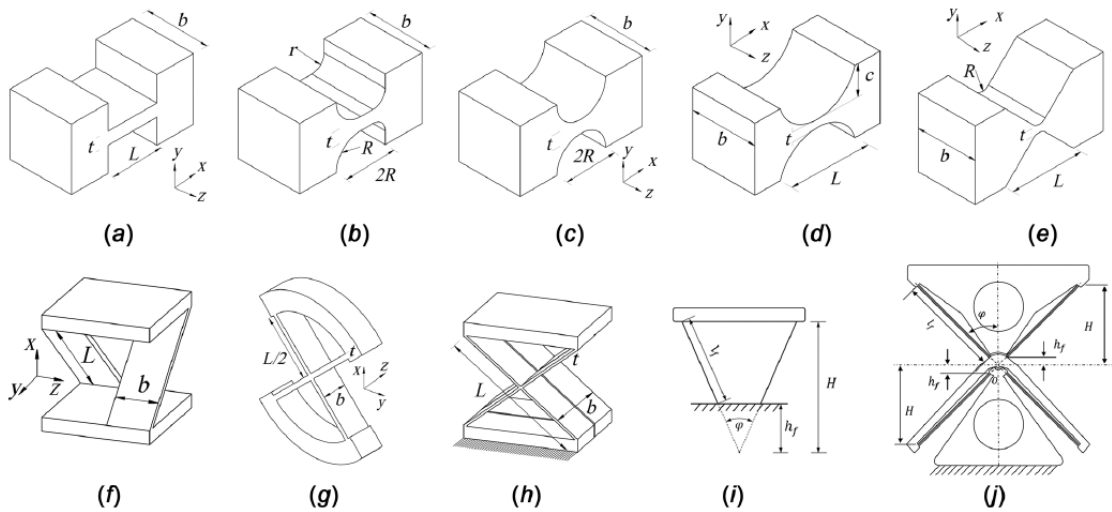


Figure 1-7: Compliant rotational joints [37]

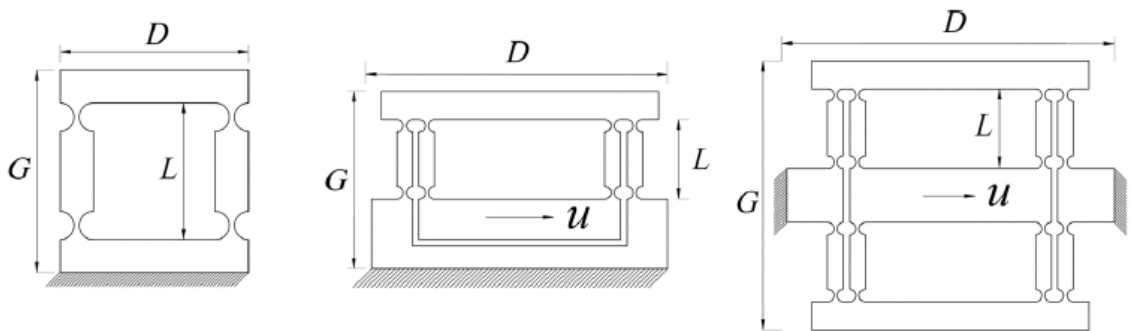


Figure 1-8: Compliant translational joints [37]

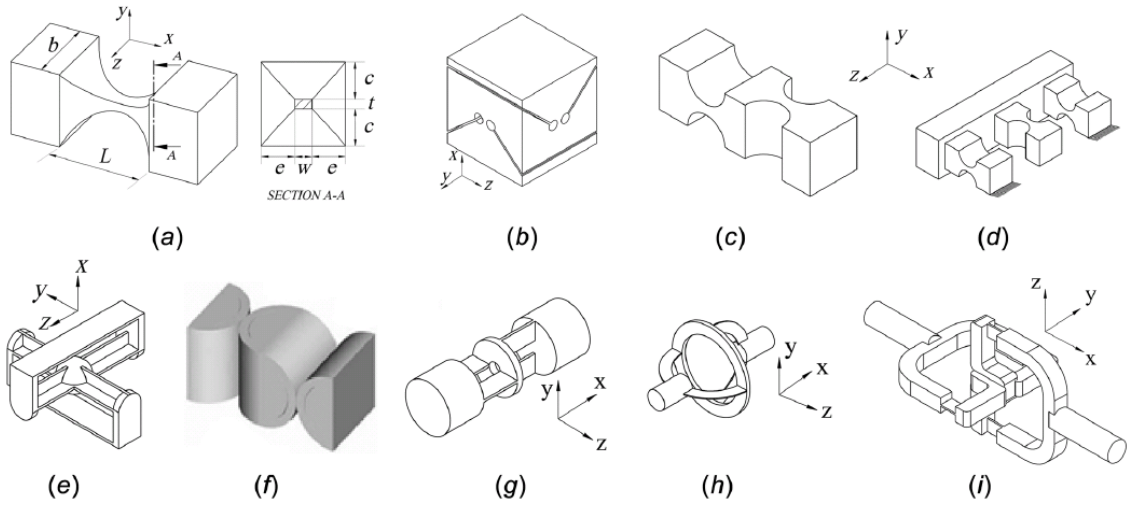


Figure 1-9: Compliant universal joints [37]

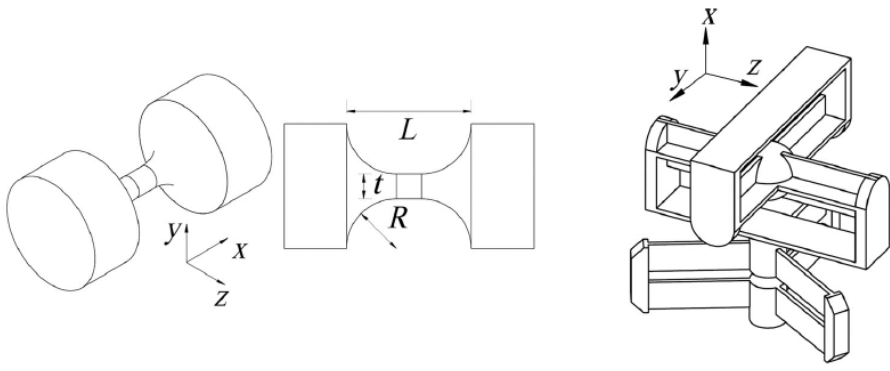


Figure 1-10: Compliant spherical joints [37]

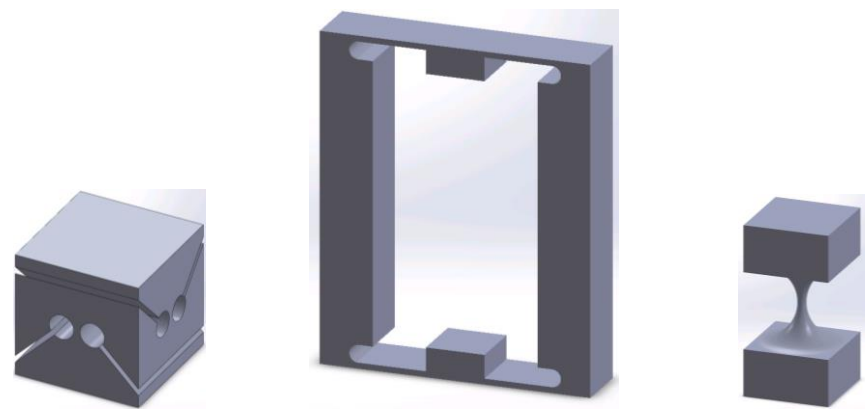


Figure 1-11: CAD models of compliant joints adopted in the study (from left to right: CUJ, CPJ, CSJ)

## 1.2 Literature Review

### 1.2.1 Micromanipulator

Micromanipulator features a micro-scale working range and nano-scale resolution and becomes more and more popular in modern science and technology fields such as microfabrication, micro-assembly, bioengineering and microsurgery. Many researchers have been dedicating themselves to the advances of this subject and extensive studies have already been implemented for micromanipulators covering mechanism configuration, compliant flexure hinges and actuation modes.

In many studies, micromanipulators constantly take the form of a combination of parallel and compliant mechanisms and the so-called CPM keeps the notable advantages of both as a result making it an undoubted candidate for micromanipulators. Parallel mechanisms are famous for high rigidity, high payload capacity and high positioning precision, all of which are beneficial from the moving platform connecting to the fixed base through several kinematic chains rather than a single one in the case of serial mechanisms.[38] Compliant mechanisms have a monolithic structure which utilizes deflection of flexible elements to transmit motion, force and energy, thus effectively avoiding Coulomb friction and backlash and achieving high-accuracy motions.[39]

Since Scire and Teague put forward to a 1-DOF vacuum-compatible micro-positioning stage for accurate measurement [40], many micromanipulators with different configurations have been developed. Under the inspiration of chopstick motions, Tanikawa and Arai proposed a micro-hand with two fingers, each having six DOFs.[41] And then they presented a micro-finger with 3 pure translational DOFs based on a 3-

RPPR mechanism.[42] Ryu and others developed a planar 3-DOF micro-wafer stage and the modeling and optimal design procedure of the micro-motion was also illustrated.[43] In 2009, Culpepper and Anderson created a nano-manipulator for ultra-precision fiber optic aligning using a 6-axis compliant mechanism.[44] Li and Xu designed a micro-manipulator starting from an XY-parallel mechanism and also built a full nonlinear kinematic model.[45] Besides proposing a flexure-based 3-RRR compliant micro-motion stage, Yong and others derived a kinetostatic model and showed the impact of the accuracy of flexure hinge compliance equations on output compliance.[46],[47] Tian and others proposed a 2-DOF flexure-based five-bar micromanipulator and further obtained the forward kinematics.[48],[49] Yue and others creatively presented several perpendicular parallel micro-manipulators of 3 DOFs and 6 DOFs. They studied the relationship among stiffness, payload, input force and displacement and they found the isotropy and decoupling characteristics of the proposed mechanism.[50],[51] Recently, Dong, Gao and Yue designed a novel planar 3-DOF micromanipulator with orthogonal structure and implemented an experimentally calibrated open-loop model to evaluate the performance of trajectory execution.[52] Moreover, conventional actuators like motors, hydraulic and pneumatic actuators are not proper to the micro-actuation in terms of their displacement resolution and accuracy. Starting from that Ellis proposed piezoelectric devices as micromanipulator actuators [53], they have been adopted commonly considering their small size, compact structure and high resolution.

Although many micromanipulators with different configurations have been developed and analyzed, most of them are dealing with planar cases facilitating most of planar

manipulation. Actually, multi-DOF manipulation in a 3-D space is much needed, which is what the 3-UPS micromanipulator in this thesis is addressing.

### **1.2.2 Macro-micro Manipulator**

Different from micromanipulators featuring high manipulation accuracy, macro-micro manipulator can include it as part of the configuration and it aims to enlarge the workspace range on the basis of precise motions. The concept of macro-micromanipulator system was first proposed by Sharon A. [54],[55] and it introduced the combination of macro and micro motions, involving the integration of the two types of manipulators.

Based on this idea, a series of researches have been conducted. William E. S. [56] developed a novel type of crane robot connecting two moving platforms in sequence, which is thought of a conceptual design for open-ocean cargo transfer. Dong W. [57] proposed a compliant parallel positioner dually driven by six PZT motors and six PZT ceramics. It is characterized as a stroke of 10 mm in three translational directions and 6 degrees in three rotational directions. Eric Ho [58] designed a single-axis macro-micro positioning system capable of a motion range of 200 mm and positioning resolution of less than 5  $\mu\text{m}$  and also explored the potential of SMA actuators for lower cost. Jialiang Z. [59] developed a macro-micro ultra-precision positioning stage and achieved the positioning accuracy of  $0.1 \pm 0.02 \mu\text{m}$  by using PZT actuators. In [60], by integrating two types of actuators, say DC servomotors for macro motion and PZT actuators for the micro motion in order to form one actuating motion, P. R. Ouyang applied a new design strategy with the elimination of the interaction of two sorts of motions. Jin F. and others

[61] developed a macro-micro parallel structure system for chromosome dissection with macro part based on a 6-PPPS orthogonal parallel manipulator actuated by six servo motors and micro part based on a 6-PSS orthogonal parallel manipulator driven by six PZT actuators. In [62], Qin and others incorporate enhanced Scott-Russell mechanisms into a 3-RRR manipulator in order to magnify PZT output displacement.

All these studies aforementioned prove that the macro-micro manipulator design is an excellent solution to obtaining large workspace with micro-level precision. To satisfy specific requirements for different applications, such as higher accuracy and stiffness, multiple DOFs with relatively large movement range, much more efforts are still ongoing, which are also the motivation of this study.

### **1.3 Contribution and Objective of the Study**

This thesis proposes a novel macro-micro manipulator for micromanipulation applications. The proposed manipulator has a large working range at centimeter level and a high accuracy manipulation at sub-micro meter level. It adopts a 3-UPS compliant parallel mechanism for micro and high accuracy manipulation which is pinpointed in the working range by a planar 3-RRR parallel mechanism of 3 DOFs. The micromanipulator utilizes an orthogonal parallel structure for the elimination of kinematic coupling among actuators. The way of combining the macro motion with micro motion is explored. The working session of the macro-micro manipulator can be described as follows: first positioning the micromanipulator in the operation site through macro motions and then implementing the required micromanipulation; whenever needed, the micromanipulator can travel fast among different locations in the working range.

The objective of this study is to put forward to: (1) a micromanipulator with a kinematically simple structure, high stiffness and accuracy in the end-effector (or moving platform); (2) a new way to incorporate the macro and micro motion to achieve the integration of large working range and high accuracy manipulation. This thesis covers the design, analysis and optimization of the proposed macro-micro manipulator, which are going to be detailed in next section.

## **1.4 Organization of the Thesis**

The remainder of the thesis is arranged as follows.

Chapter 2 gives a description of the geometry of the macro-micro manipulator and based on kinematic modeling, the inverse kinematic analysis is conducted separately for micromanipulator and macromanipulator. Furthermore, Jacobian matrices for both are also formulated.

Chapter 3 deals with the stiffness analysis of the micromanipulator. By different levels of stiffness modeling, the stiffness matrix and compliance matrix are obtained and compliance mapping is also presented, reflecting the relationship between directional stiffness and design variables. This chapter is also a prerequisite for later optimization.

Chapter 4 focuses on the workspace analysis. By performing a point search method for determination of workspace boundary, the workspace shape and volume of the micromanipulator is analyzed, which helps to further evaluate and optimize the micromanipulation's workspace properties.

Chapter 5 addresses the optimization with respect to design variables of the micromanipulator for better performance. Single-objective optimization for a single

performance criterion and multi-objective optimization for finding a set of trade-offs among different objectives are conducted, respectively. The optimization technique FA is introduced to implement the optimization and augment the proposed design.

Chapter 6 concludes the important work involved in the study and what has been achieved. Further study is also suggested to be done in the future.

# Chapter 2

## Inverse Kinematics and Jacobian Analysis

### 2.1 Introduction

Kinematic analysis deals with aspects of motion, not considering forces and torques causing it. In robotic manipulator kinematics, the joint variables (e.g. actuated leg angles or linear displacement of legs) are related to the position and orientation of the moving platform by the constraints imposed by joints and links. It is necessary to study the geometrical and time properties of the manipulator motion in order to find all possible sets of actuated joint variables together with their corresponding time derivatives for given poses (i.e. position and orientation) of moving platform in terms of inverse kinematics.

Jacobian matrix is an important part of kinematic analysis which provides the velocity mapping from moving platform space to joint variable space. The Jacobian matrix not only reveals the relation between actuated joint rates of a parallel manipulator and linear

and angular velocities of the moving platform, but also constructs the transformation from the external load exerted on the moving platform to the actuator forces and torques needed. Also, the condition number of Jacobian matrix provides a way to measure the amplification error between the actuators and the moving platform, which will be used to help formulate a criterion for optimizing the workspace quality in later chapter.

The CAD model of the macro-micro manipulator under study is provided in Figure 2-1. In this chapter, for both micromanipulator and macromanipulator, geometrical description will be first given and then based on the establishment of proper reference coordinate systems, the inverse kinematics and Jacobian formulation for both will be presented in detail. PRB model method is adopted for the micromanipulator which effectively avoids complex elliptic integral solutions for compliant mechanisms. Closed vector loop method is used to obtain kinematic constraints imposed by the mechanism.

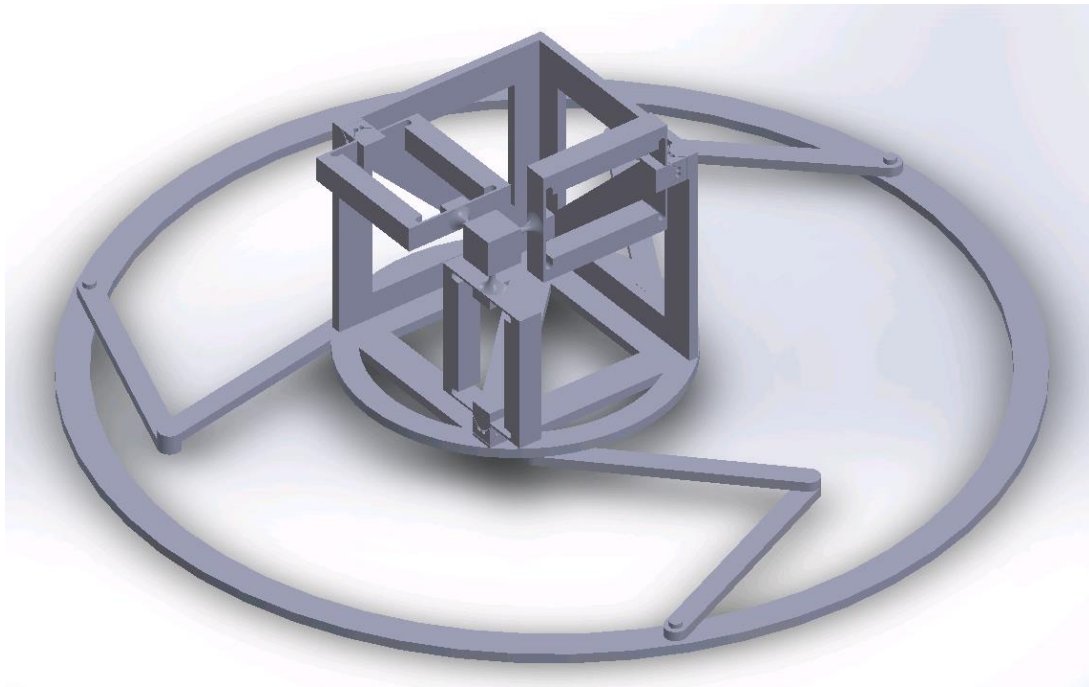


**Figure 2-1: CAD model of the designed macro-micromanipulator**

## 2.2 Geometry of the Micromanipulator

The micromanipulator is a spatial 3-UPS compliant parallel mechanism with an orthogonal structure as Figure 2-2 shows. It is composed of a moving platform and a fixed base which are connected by three orthogonally arranged legs of identical kinematic structure, each starting from the fixed base with a CUJ, followed by a CTJ and a CSJ to the moving platform. In the next, based on the kinematic model by using PRB method, the corresponding parameters and geometrical constraints are defined for the micromanipulator. It is noted that the PRB model simplifies the design and analysis of compliant mechanisms and facilitates knowledge of rigid-body analysis by using analogous rigid links attached by corresponding movable joints.[63]

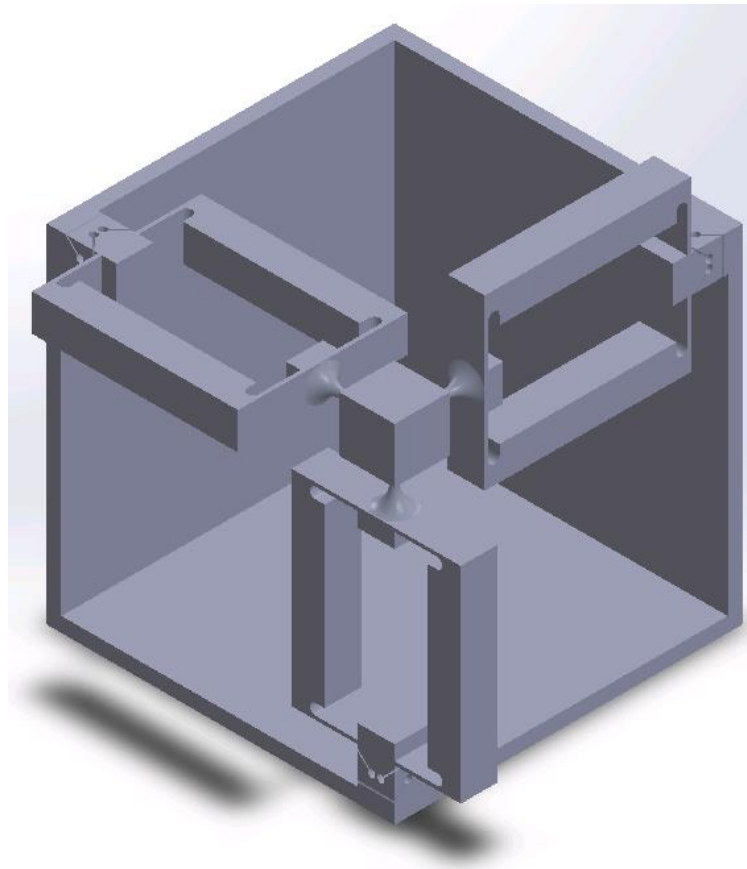


**Figure 2-2: CAD model of the 3-UPS micromanipulator**

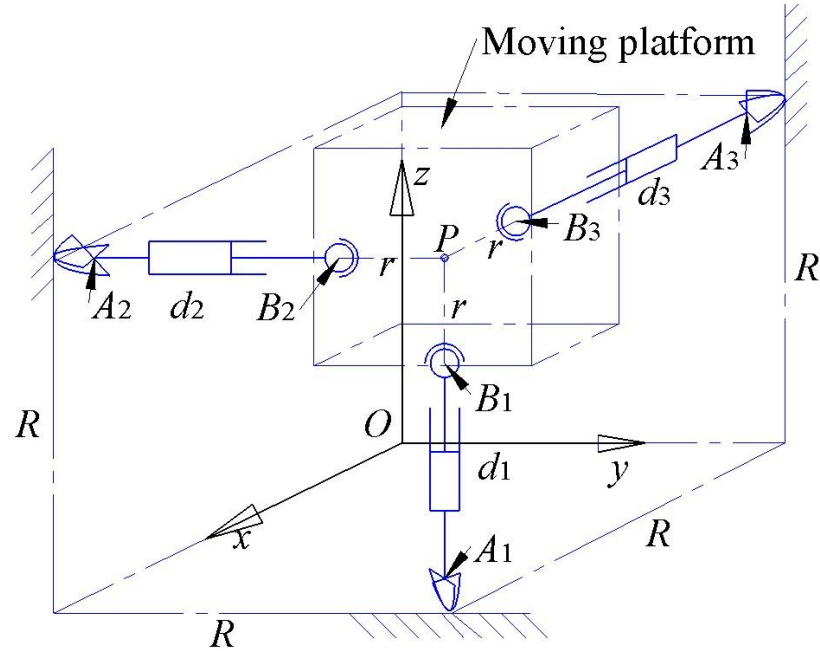


**Figure 2-3: Kinematically equivalent model of the micromanipulator by PRB method**

The PRB model is developed as depicted in Figure 2-3. Three kinematically identical legs connect the moving platform through spherical joints whose centers are denoted by  $B_i (i=1,2,3)$  to the fixed base through universal joints whose centers are denoted by  $A_i (i=1,2,3)$ . Each leg contains those upper and lower joints linked by a prismatic joint. The three prismatic joints are used as the inputs to the micromanipulator and thus the three legs have variable lengths  $d_i = \overline{A_i B_i} (i=1,2,3)$ .

For the purpose of analysis, two Cartesian coordinate systems, namely  $O-xyz$  (see Figure 2-3) and  $P-uvw$  (see Figure 2-4) are attached to the fixed base and the moving platform, respectively. The following assumptions are made. Points of attachment to the fixed base  $A_i$  are located in three orthogonal planes and on a sphere surface of radius  $R$ . Similarly, points of attachment to the moving platform  $B_i$  are in the center of three orthogonal faces of the cube and also on a sphere surface of radius  $r$ . For the fixed coordinate system, the origin  $O$  is at the intersection of the three orthogonal planes and

three coordinate axes satisfy  $\mathbf{z} = \mathbf{x} \times \mathbf{y}$ . For the moving coordinate system as shown in Figure 2-4,  $u$ -,  $v$ - and  $w$ - axis are directed along  $\overline{B_3P}$ ,  $\overline{B_2P}$  and  $\overline{B_1P}$ , respectively.

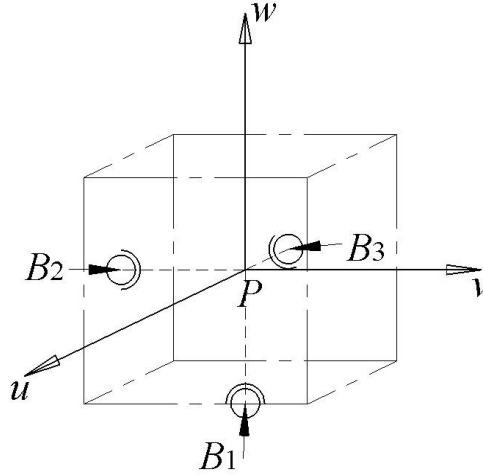


**Figure 2-4: Establishment of the moving coordinate system**

The transformation from the moving platform to the fixed base can be described by a position vector  $\mathbf{p} = \overline{OP} = [p_x \ p_y \ p_z]^T$ , and a 3 by 3 rotation matrix  ${}^o\mathbf{R}_p$ . Set  $\mathbf{u}, \mathbf{v}, \mathbf{w}$  be three unit vectors along the  $u$ -,  $v$ -,  $w$ -axis of the moving coordinate system  $P$ - $uvw$ , respectively. Then the rotation matrix can be represented in terms of the direction cosines of  $\mathbf{u}, \mathbf{v}, \mathbf{w}$  as

$${}^o\mathbf{R}_p = \begin{bmatrix} u_x & v_x & w_x \\ u_y & v_y & w_y \\ u_z & v_z & w_z \end{bmatrix}. \quad (2.1)$$

The elements of  ${}^o\mathbf{R}_p$  must satisfy the following orthogonal conditions [64]:

$$u_x^2 + u_y^2 + u_z^2 = 1, \quad (2.2)$$

$$v_x^2 + v_y^2 + v_z^2 = 1, \quad (2.3)$$

$$w_x^2 + w_y^2 + w_z^2 = 1, \quad (2.4)$$

$$u_x v_x + u_y v_y + u_z v_z = 0, \quad (2.5)$$

$$u_x w_x + u_y w_y + u_z w_z = 0, \quad (2.6)$$

$$v_x w_x + v_y w_y + v_z w_z = 0, \quad (2.7)$$

Let  $\mathbf{a}_i$  and  $\mathbf{b}'_i$  be the position vector of points  $A_i$  and  $B_i$  in the coordinate system  $O$ - $xyz$  and  $P$ - $uvw$ , respectively. Then

$$\mathbf{a}_1 = [R, R, 0]^T, \quad (2.8)$$

$$\mathbf{a}_2 = [R, 0, R]^T, \quad (2.9)$$

$$\mathbf{a}_3 = [0, R, R]^T, \quad (2.10)$$

$$\mathbf{b}'_1 = [0, 0, -r], \quad (2.11)$$

$$\mathbf{b}'_2 = [0, -r, 0], \quad (2.12)$$

$$\mathbf{b}'_3 = [-r, 0, 0]. \quad (2.13)$$

The position vector  $\mathbf{b}_i$  of points  $B_i$  with respect to the fixed coordinate system can be obtained by the following transformation:

$$\mathbf{b}_i = \mathbf{p} + {}^O\mathbf{R}_p \cdot \mathbf{b}'_i, \quad (2.14)$$

Substituting (2.2) and (2.12) through (2.14) into (2.15) yields

$$\mathbf{b}_1 = \begin{bmatrix} p_x - w_x r \\ p_y - w_y r \\ p_z - w_z r \end{bmatrix}, \quad (2.15)$$

$$\mathbf{b}_2 = \begin{bmatrix} p_x - v_x r \\ p_y - v_y r \\ p_z - v_z r \end{bmatrix}, \quad (2.16)$$

$$\mathbf{b}_3 = \begin{bmatrix} p_x - u_x r \\ p_y - u_y r \\ p_z - u_z r \end{bmatrix}. \quad (2.17)$$



$$d_2^2 = p_x^2 + p_y^2 + p_z^2 + r^2(v_x^2 + v_y^2 + v_z^2) - 2r(p_x v_x + p_y v_y + p_z v_z) + 2R^2 - 2R(p_x - v_x r) - 2R(p_z - v_z r), \quad (2.23)$$

$$d_3^2 = p_x^2 + p_y^2 + p_z^2 + r^2(u_x^2 + u_y^2 + u_z^2) - 2r(p_x u_x + p_y u_y + p_z u_z) + 2R^2 - 2R(p_y - u_y r) - 2R(p_z - u_z r), \quad (2.24)$$

Equations of (2.23), (2.24), (2.25) relate the leg lengths to the position and orientation of the moving platform.

## 2.3 Kinematic Analysis of the Micromanipulator

### 2.3.1 Mobility Analysis

The mobility describes the number of DOFs of the mechanism. Generally, the Chebychev-Grübler-Kutzbach formula (2.25) can provide a preliminary prediction of the mobility of a kinematic chain.

$$M = d(n - g - 1) + \sum_{i=1}^g f_i \quad (2.25)$$

where

$M$  is the number of DOF or mobility of the mechanism,

$d$  is the number of DOF of each unconstrained individual body (6 for the spatial case, 3 for the planar case),

$n$  is the number of rigid bodies or links in the mechanism,

$g$  is the number of joints,

$f_i$  is the number of DOFs allowed by the  $i$ th joint.

But for the micromanipulator under study which has compliant joints and an orthogonal configuration, it is much more appropriate to determine the mobility directly from exami-

ning the links' and the joints' characteristics.

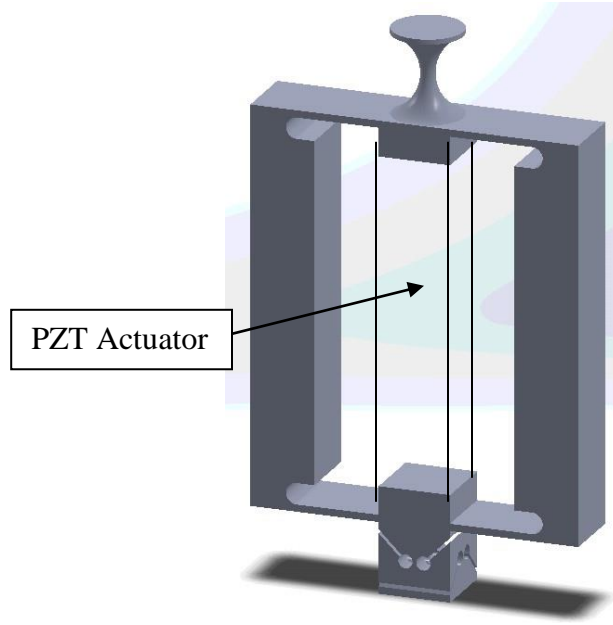


**Figure 2-6: CAD Representation of links and joints in one leg**

Referring to Figure 2-6, the intermediate PZT actuator is connected to the moving platform through a compliant spherical joint which has 3 DOFs and is connected to the fixed base through a compliant universal joint which has 2 DOFs. Before connected together, each individual body of the mechanism has six DOFs relative to the fixed base. Therefore, excluding the fixed base, four individual bodies in the micromanipulator, say one moving platform and three PZT actuators, have  $6 \times 4 = 24$  DOFs. Introducing a joint would reduce the number of DOFs that the joint can be able to constrain. The compliant spherical joint is able to constrain 3 DOFs while the compliant universal joint is able to constrain 4 DOFs. Therefore, after subtracting constraints of all joints from the total DOFs of the individual bodies, the mobility of the micromanipulator can be obtained by

$$M = 6n - 3j_3 - 4j_2 = 6 \times 4 - 3 \times 3 - 3 \times 4 = 3 \quad (2.26)$$

where

$n$  denotes the number of individual bodies except the fixed base,

$j_3$  denotes the number of constraint DOFs by the spherical joint,

$j_2$  denotes the number of constraint DOFs by the universal joint.

In addition, because of the special parallel structure with three kinematic chains configured in three mutually orthogonal directions, the three translational DOFs along  $x$ -,  $y$ -,  $z$ -axis respectively, can be figured out.

### 2.3.2 Inverse Kinematic Analysis

The inverse kinematic problem can be described as: provided the location and orientation of the moving platform, find the actuated joint variable values. For the micromanipulator, that is, given the position vector  $\mathbf{p}$  and the rotation matrix  ${}^o\mathbf{R}_p$  of the moving platform, find the leg lengths  $d_i (i = 1, 2, 3)$ . This is straightforward by computing the square roots of (2.23) through (2.25) for three legs respectively and obviously only the positive values for leg length are physically realizable.

### 2.3.3 Jacobian Formulation

The Jacobian matrix of the micromanipulator relates the 6-D twist velocity vector of the moving platform  $\dot{\boldsymbol{\chi}}$  to that of actuated joint rates  $\dot{\mathbf{d}}$ , such that [65]

$$\dot{\mathbf{d}} = J \dot{\boldsymbol{\chi}}. \quad (2.27)$$

The joint rate input vector is given by  $\dot{\mathbf{d}} = [\dot{d}_1, \dot{d}_2, \dot{d}_3]^T$ . The twist vector of the moving platform can be described by the velocity of the point  $P$   $\mathbf{v}_p = [v_{px}, v_{py}, v_{pz}]^T$  and the angular velocity of the moving platform  $\boldsymbol{\omega}_p = [\omega_x, \omega_y, \omega_z]^T$ . Thus, it can be written as

$$\dot{\boldsymbol{\chi}} = \begin{bmatrix} \mathbf{v}_p \\ \boldsymbol{\omega}_p \end{bmatrix} = [v_{px}, v_{py}, v_{pz}, \omega_x, \omega_y, \omega_z]^T. \quad (2.28)$$

To derive the velocity loop closure, differentiate (2.20) with respect to time and replace  $\mathbf{d}_i$  with  $d_i \hat{\mathbf{s}}_i$ , one has

$$\dot{d}_i \hat{\mathbf{s}}_i + d_i (\boldsymbol{\omega}_i \times \hat{\mathbf{s}}_i) = \mathbf{v}_p + \boldsymbol{\omega} \times {}^o \mathbf{R}_p \mathbf{b}'_i \quad (i=1,2,3) \quad (2.29)$$

where  $\hat{\mathbf{s}}_i$  is the unit vector along  $\mathbf{d}_i$ ,  $\boldsymbol{\omega}_i$  is the angular velocity of the  $i$ th leg with respect to the fixed coordinate system. To eliminate  $\boldsymbol{\omega}_i$ , dot-multiply both sides of (2.28) by  $\hat{\mathbf{s}}_i$ :

$$\dot{d}_i = \mathbf{v}_p \cdot \hat{\mathbf{s}}_i + [{}^o \mathbf{R}_p \mathbf{b}'_i \times \hat{\mathbf{s}}_i]^T \cdot \boldsymbol{\omega}. \quad (2.30)$$

Writing the above equation three times for each leg in a vector form as that in equation (2.26) yields the Jacobian matrix of the micromanipulator

$$J = \begin{bmatrix} \hat{\mathbf{s}}_1^T & ({}^o \mathbf{R}_p \mathbf{b}'_1 \times \hat{\mathbf{s}}_1)^T \\ \hat{\mathbf{s}}_2^T & ({}^o \mathbf{R}_p \mathbf{b}'_2 \times \hat{\mathbf{s}}_2)^T \\ \hat{\mathbf{s}}_3^T & ({}^o \mathbf{R}_p \mathbf{b}'_3 \times \hat{\mathbf{s}}_3)^T \end{bmatrix}_{3 \times 6}. \quad (2.31)$$

## 2.4 Geometry of the Micromanipulator

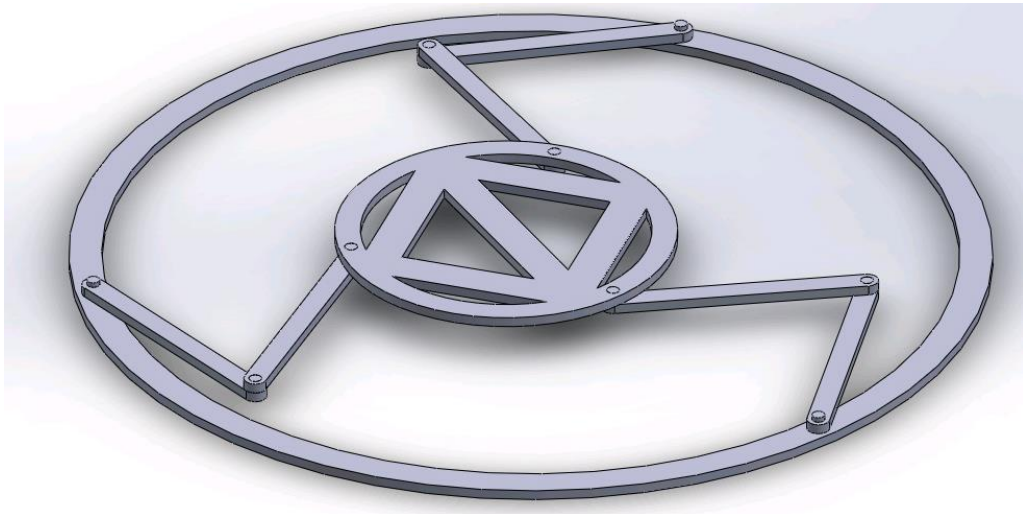
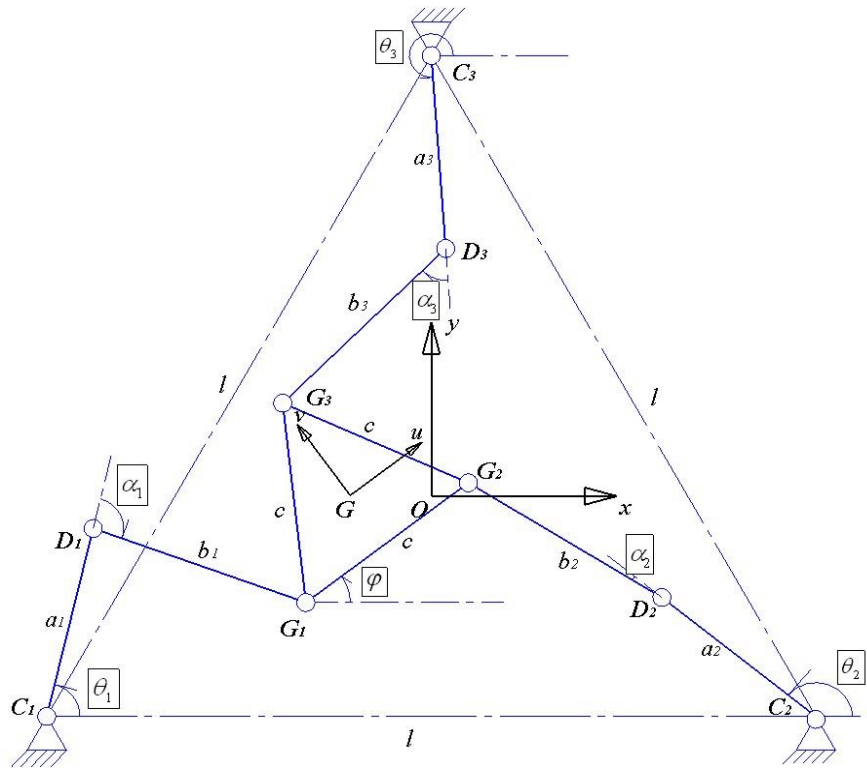


Figure 2-7: CAD model of the micromanipulator

The macromanipulator is a 3-RRR planar parallel mechanism whose CAD model is shown in Figure 2-7. It consists of the inner moving platform and the outer fixed base connected by three legs which share the similar kinematic structure. Every two links are joined by a revolute joint. The mobility of the mechanism can be calculated based on the Chebychev-Grübler-Kutzbach formula:

$$M = d(n - g - 1) + \sum_{i=1}^g f_i = 3(8 - 9 - 1) + (1 + 1 + 1) \times 3 = 3. \quad (2.32)$$

Therefore, this 3-RRR planar parallel mechanism has 3 planar DOFs, namely two translational DOFs along  $x$ - and  $y$ -axis and one rotational DOF around  $z$ -axis.



**Figure 2-8: Schematic representation of the macromanipulator**

Referring to Figure 2-8, three legs connect the moving platform at points  $G_1, G_2, G_3$  to the fixed base at points  $C_1, C_2, C_3$  by revolute joints. For the purpose of analysis, two reference coordinate systems are established: the fixed coordinate system  $O$ - $xy$  is

attached to the fixed base and the origin  $O$  is located at the center of the equilateral triangle  $\Delta C_1 C_2 C_3$  with the edge length of  $l$ ,  $x$ -axis pointing along the direction of  $\overline{C_1 C_2}$  and perpendicular to  $y$ -axis; the coordinate system  $G-uv$  is attached to the moving platform and the point  $G$  is the center of the equilateral triangle  $\Delta G_1 G_2 G_3$  with the edge length of  $c$ ,  $u$ -axis pointing along the direction of  $\overline{G_1 G_2}$  and perpendicular to  $v$ -axis.

For each leg,  $a_i$  and  $b_i (i=1,2,3)$  are link lengths and  $\theta_i (i=1,2,3)$  are the input or actuation angles. The location and orientation of the moving platform can be described by the position vector

$$\mathbf{g} = \overline{OG} = [x_g, y_g]^T \quad (2.33)$$

and the rotation matrix

$${}^o \mathbf{R}_G = \mathbf{R}_z(\varphi) = \begin{bmatrix} c\varphi & -s\varphi \\ s\varphi & c\varphi \end{bmatrix}. \quad (2.34)$$

where  $\varphi$  is the orientation angle of the moving platform with respect to the  $x$ -axis.

Coordinates of point  $C_i$  with respect to the fixed coordinate system  $O-xy$  are given:

$$\overline{OC_1} = \left[ \frac{\sqrt{3}}{3} l \cdot \cos\left(-\frac{5\pi}{6}\right), \frac{\sqrt{3}}{3} l \cdot \sin\left(-\frac{5\pi}{6}\right) \right]^T = \left[ -\frac{l}{2}, -\frac{\sqrt{3}}{6} l \right]^T, \quad (2.35)$$

$$\overline{OC_2} = \left[ \frac{\sqrt{3}}{3} l \cdot \cos\left(-\frac{5\pi}{6} + \frac{2\pi}{3}\right), \frac{\sqrt{3}}{3} l \cdot \sin\left(-\frac{5\pi}{6} + \frac{2\pi}{3}\right) \right]^T = \left[ \frac{l}{2}, -\frac{\sqrt{3}}{6} l \right]^T, \quad (2.36)$$

$$\overline{OC_3} = \left[ \frac{\sqrt{3}}{3} l \cdot \cos\left(-\frac{5\pi}{6} + \frac{4\pi}{3}\right), \frac{\sqrt{3}}{3} l \cdot \sin\left(-\frac{5\pi}{6} + \frac{4\pi}{3}\right) \right]^T = \left[ 0, \frac{\sqrt{3}}{3} l \right]^T, \quad (2.37)$$

Similar process applied to the calculation of the coordinates of point  $G_i$  with respect to the moving coordinate system  $G-uv$  yields

$${}^{(G-uv)} \overline{GG_1} = \left[ \frac{\sqrt{3}}{3} c \cdot \cos\left(-\frac{5\pi}{6}\right), \frac{\sqrt{3}}{3} c \cdot \sin\left(-\frac{5\pi}{6}\right) \right]^T = \left[ -\frac{c}{2}, -\frac{\sqrt{3}}{6} c \right]^T \quad (2.38)$$

$${}^{(G-uv)}\overline{GG}_2 = \left[ \frac{\sqrt{3}}{3}c \cdot \cos\left(-\frac{5\pi}{6}\right), \frac{\sqrt{3}}{3}c \cdot \sin\left(-\frac{5\pi}{6} + \frac{2\pi}{3}\right) \right]^T = \left[ \frac{c}{2}, -\frac{\sqrt{3}}{6}c \right]^T \quad (2.39)$$

$${}^{(G-uv)}\overline{GG}_3 = \left[ \frac{\sqrt{3}}{3}c \cdot \cos\left(-\frac{5\pi}{6} + \frac{4\pi}{3}\right), \frac{\sqrt{3}}{3}c \cdot \sin\left(-\frac{5\pi}{6} + \frac{4\pi}{3}\right) \right]^T = \left[ 0, \frac{\sqrt{3}}{3}c \right]^T \quad (2.40)$$

To obtain the coordinates of points  $G_i$  with respect to the fixed coordinate system, a transformation must be utilized:

$$\overline{OG}_i = \mathbf{g} + {}^o\mathbf{R}_G {}^{(G-uv)}\overline{GG}_i \quad (i=1,2,3). \quad (2.41)$$

Then

$$\overline{OG}_1 = [G_{1x}, G_{1y}]^T = \left[ x_g - \frac{c}{2} \cdot c\varphi + \frac{\sqrt{3}}{6}c \cdot s\varphi, y_g - \frac{c}{2} \cdot s\varphi - \frac{\sqrt{3}}{6}c \cdot c\varphi \right]^T \quad (2.42)$$

$$\overline{OG}_2 = [G_{2x}, G_{2y}]^T = \left[ x_g + \frac{c}{2} \cdot c\varphi + \frac{\sqrt{3}}{6}c \cdot s\varphi, y_g + \frac{c}{2} \cdot s\varphi - \frac{\sqrt{3}}{6}c \cdot c\varphi \right]^T \quad (2.43)$$

$$\overline{OG}_3 = [G_{3x}, G_{3y}]^T = \left[ x_g - \frac{\sqrt{3}}{3}c \cdot s\varphi, y_g + \frac{\sqrt{3}}{3}c \cdot c\varphi \right]^T \quad (2.44)$$

A vector-loop equation can be written for three legs in a general form

$$\overline{OG}_i = \overline{OC}_i + \overline{C}_i\overline{D}_i + \overline{D}_i\overline{G}_i \quad (i=1,2,3) \quad (2.45)$$

Substituting (2.34) and (2.41) into (2.44), noticing

$$\overline{C}_i\overline{D}_i = \begin{bmatrix} a_i \cdot c\theta_i \\ a_i \cdot s\theta_i \end{bmatrix}, \overline{D}_i\overline{G}_i = \begin{bmatrix} b_i \cdot c(\theta_i + \alpha_i) \\ b_i \cdot s(\theta_i + \alpha_i) \end{bmatrix}, \quad (2.46)$$

one has the following for the first leg:

$$G_{1x} = -\frac{l}{2} + a_1 c\theta_1 + b_1 c(\theta_1 + \alpha_1), \quad (2.47)$$

$$G_{1y} = -\frac{\sqrt{3}}{6}l + a_1 s\theta_1 + b_1 s(\theta_1 + \alpha_1). \quad (2.48)$$

To eliminate the passive joint angle  $\alpha_1$ , summing the square of both (2.46) and (2.47)

and sorting out the result yields

$$(2a_1G_{1y} - \frac{\sqrt{3}}{3}a_1l) \cdot s\theta_1 - (2a_1G_{1x} + a_1l) \cdot c\theta_1 + G_{1x}^2 + G_{1y}^2 + lG_{1x} + \frac{\sqrt{3}}{3}lG_{1y} + \frac{l^2}{3} + a_1^2 - b_1^2 = 0 \quad (2.49)$$

Similarly, two additional equations can be derived for leg 2 and 3:

$$(2a_2G_{2y} - \frac{\sqrt{3}}{3}a_2l) \cdot s\theta_2 + (a_2l - 2a_2G_{2x}) \cdot c\theta_2 + G_{2x}^2 + G_{2y}^2 - lG_{2x} + \frac{\sqrt{3}}{3}lG_{2y} + \frac{l^2}{3} + a_2^2 - b_2^2 = 0 \quad (2.50)$$

$$(\frac{2\sqrt{3}}{3}a_3l - 2a_3G_{3y})s\theta_2 + G_{3y}^2 + \frac{l^2}{3} + a_3^2 - b_3^2 = 0 \quad (2.51)$$

## 2.5 Kinematics of the Macromanipulator

### 2.5.1 Inverse Kinematic Analysis

For the inverse kinematics of the planar parallel mechanism,  $x_g, y_g, \varphi$  are given and the actuated joint angles  $\theta_i (i=1,2,3)$  are aimed to be found. This can be accomplished on a leg-by-leg basis. For leg 1, rearrange the closed vector loop equation (2.48) in such a form

$$e_1 s\theta_1 + e_2 c\theta_1 + e_3 = 0 \quad (2.52)$$

where

$$e_1 = 2a_1G_{1y} - \frac{\sqrt{3}}{3}a_1l,$$

$$e_2 = -(2a_1G_{1x} + a_1l),$$

$$e_3 = G_{1x}^2 + G_{1y}^2 + lG_{1x} + \frac{\sqrt{3}}{3}lG_{1y} + \frac{l^2}{3} + a_1^2 - b_1^2.$$

Substituting the trigonometric identities  $s\theta_i = \frac{2t_i}{1+t_i^2}$  and  $c\theta_i = \frac{1-t_i^2}{1+t_i^2}$  where  $t_i = \tan \frac{\theta_i}{2}$

into (2.51) gives

$$(e_3 - e_2)t_1^2 + 2e_1t_1 + (e_2 + e_3) = 0 \quad (2.53)$$

Solving (2.52) for  $t_1$ , one has

$$\theta_1 = 2 \operatorname{atan} \frac{-e_1 \pm \sqrt{e_1^2 + e_2^2 - e_3^2}}{e_3 - e_2} \quad (2.54)$$

Therefore, for each required moving platform pose, there are generally two solutions of  $\theta_1$  and accordingly two configurations of leg 1. When (2.51) yields no real root, the specified moving platform pose is considered to be not reachable.

Following the same procedure, the other two leg configurations can be worked out. It is noted that generally there are totally eight possible overall leg configurations corresponding to a certain moving platform pose.

## 2.5.2 Jacobian Formulation

The Jacobian matrix of the macromanipulator relates the actuated joint rates to the moving platform linear and angular velocities, which can be represented in a vector equation [65]

$$\dot{\mathbf{q}} = J \cdot \dot{\boldsymbol{\chi}} \quad (2.55)$$

where  $\dot{\mathbf{q}} = [\dot{\theta}_1, \dot{\theta}_2, \dot{\theta}_3]^T$  describes the input joint rates by differentiating the actuated joint

position vector  $\mathbf{q}$  while  $\dot{\boldsymbol{\chi}} = \begin{bmatrix} \mathbf{v}_G \\ \boldsymbol{\omega}_G \end{bmatrix} = [\dot{x}_g, \dot{y}_g, \dot{\varphi}]^T$  is the moving platform output twist

reflecting the linear velocity  $\mathbf{v}_G$  and angular velocity  $\boldsymbol{\omega}_G$  of the moving platform.



$$J_q = \begin{bmatrix} x_{a1}y_{b1} - y_{a1}x_1 & 0 & 0 \\ 0 & x_{a1}y_{b1} - y_{a1}x_1 & 0 \\ 0 & 0 & x_{a1}y_{b1} - y_{a1}x_1 \end{bmatrix}. \quad (2.60)$$

And then the Jacobian matrix of the macromanipulator is [66]

$$J = J_q^{-1} J_x \quad (2.61)$$

## 2.6 Conclusions

This chapter focuses on the kinematic analysis of the macro-micromanipulator. Based on a detailed geometrical description of micromanipulator and macromanipulator, including the setup of corresponding parameters and kinematic constraints on them, the inverse kinematic problem is addressed using the closed vector loop equation method in a simple and straightforward manner. Under these fundamentals, the Jacobian formulation is actually the differential kinematics and the Jacobian matrices are also derived.

# Chapter 3

## Stiffness Analysis

### 3.1 Introduction

When the moving platform of a manipulator is performing a specific task in contact with external environment, deflections will appear at the contact point as a result of the reaction forces from the external environment. The amount of deflections is influenced by the applied forces and the manipulator structural stiffness. Therefore, the stiffness of a manipulator can have a direct impact on the manipulation and positioning accuracy.

This chapter is going to address problems associated with stiffness and compliance which are two closely related concepts. The overall stiffness of a manipulator is affected by several factors, such as the dimension and material of the links, the transmission mechanism, the actuators and even the controller. However, for the compliant mechanisms the stiffness of compliant joints plays a dominant role. In what follows, it is assumed that the moving platform and connecting links are perfectly rigid and the compliant joints are the main sources of compliance.

The objective and attention of this thesis is mainly directed towards the micromanipulator. In the following the stiffness analysis of the micromanipulator will be dealt with in detail following the sequence of stiffness modeling of basic compliant elements, one kinematic chain or leg and eventually the whole manipulator.

## 3.2 Stiffness and Compliance Matrices of Basic Compliant Elements

First of all, there is the definition related to external load and the corresponding infinitesimal deflection. A wrench vector  $\mathbf{F}$  is used to define the external load containing the distributive components of force and moment in/around three coordinate axes in space, which takes the form

$$\mathbf{F} = [F_x, F_y, F_z, \tau_x, \tau_y, \tau_z]^T. \quad (3.1)$$

Accordingly, the concept of twist  $\Delta\mathbf{X}$  describes the linear and angular infinitesimal displacement caused by the force component and moment component of  $\mathbf{F}$ , which conforms to the form

$$\Delta\mathbf{X} = [\delta_x, \delta_y, \delta_z, \Delta\theta_x, \Delta\theta_y, \Delta\theta_z]^T. \quad (3.2)$$

When a wrench acts on a specific point of a compliant element, an infinitesimal twist at that point results and their relationship is as the following equations show: [67]

$$\mathbf{F} = \mathbf{K}\Delta\mathbf{X} \quad (3.3)$$

$$\Delta\mathbf{X} = \mathbf{C}\mathbf{F} \quad (3.4)$$

where  $\mathbf{K}$  and  $\mathbf{C}$  are called stiffness matrix and compliance matrix respectively which are regular and symmetric and have the relation

$$\mathbf{K} = \mathbf{C}^{-1}. \quad (3.5)$$

For basic compliant elements as shown in Figure 3-1, a local coordinate system is firstly established and the resultant compliance matrix takes the form [68]

$$\mathbf{C} = \begin{bmatrix} c_1 & 0 & 0 & 0 & c_3 & 0 \\ 0 & c_2 & 0 & -c_4 & 0 & 0 \\ 0 & 0 & c_5 & 0 & 0 & 0 \\ 0 & -c_4 & 0 & c_6 & 0 & 0 \\ c_3 & 0 & 0 & 0 & c_7 & 0 \\ 0 & 0 & 0 & 0 & 0 & c_8 \end{bmatrix} \quad (3.6)$$

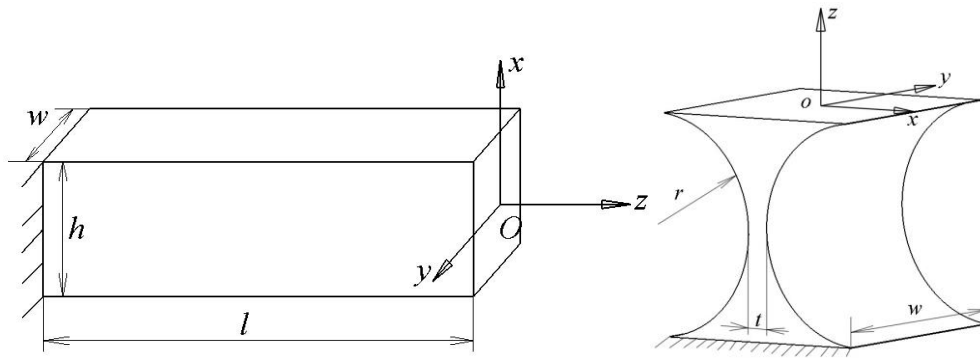


**Figure 3-1: Basic compliant elements: a cantilever (left) and a right circular hinge (right)**

where  $c_1$  to  $c_8$  are shown in Table 3-1 for the flexible beam and right circular hinge, which are frequently used in flexure mechanism calculation, hereinafter recognizing their compliance matrices as  $\mathbf{C}_{beam}$  and  $\mathbf{C}_{hinge}$ , respectively. In Table 3-1, the  $E$  and  $G$  denote modulus of longitudinal elasticity (i.e. Young's modulus) and modulus of transverse elasticity, respectively. The parameter  $k_2$  is determined by the value of  $w/h$  (see Table 3-2).

As may be noticed, (3.6) only expresses the compliance matrix in a local coordinate system. In most cases, the overall stiffness and compliance matrices expressed in a certain reference coordinate system is much needed and therefore a transformation of both the twist and the wrench between these two coordinate systems should be obtained. In the following, items with respect to a local coordinate system are denoted by a

superscript  $^o_i[\cdot]$  while items with respect to a reference coordinate system denoted by corresponding letters directly.

	Prismatic Beam	Circular Notched Hinge
$c_1$	$\frac{4l^3}{Eh^3w}$	$\frac{9\pi r^{\frac{5}{2}}}{2Ebt^{\frac{5}{2}}} + \frac{3\pi r^{\frac{3}{2}}}{2Ebt^{\frac{3}{2}}}$
$c_2$	$\frac{4l^3}{Ehw^3}$	$\frac{12\pi r^2}{Eb^3} \left( \sqrt{\frac{r}{t}} - \frac{1}{4} \right)$
$c_3$	$\frac{6l^2}{Eh^3w}$	$\frac{9\pi r^{\frac{3}{2}}}{2Ebt^{\frac{5}{2}}}$
$c_4$	$\frac{6l^2}{Ehw^3}$	$\frac{12r}{Eb^3} \left( \pi \sqrt{\frac{r}{t}} - \frac{2+\pi}{2} \right)$
$c_5$	$\frac{l}{Ehw}$	$\frac{1}{Eb} \left( \pi \sqrt{\frac{r}{t}} - \frac{\pi}{2} \right)$
$c_6$	$\frac{12l}{Ehw^3}$	$\frac{12}{Eb^3} \left( \pi \sqrt{\frac{r}{t}} - \frac{2+\pi}{2} \right)$
$c_7$	$\frac{12l}{Eh^3w}$	$\frac{9\pi r^{\frac{1}{2}}}{2Ebt^{\frac{5}{2}}}$
$c_8$	$\frac{l}{Gk_2h^3w}$	$\frac{9\pi r^{\frac{1}{2}}}{4Gbt^{\frac{5}{2}}}$

**Table 3-1: Parameters of basic compliance matrix [68]**

$w/h$	1.00	2.00	10.00	$\infty$
$k_2$	0.141	0.229	0.312	0.333

**Table 3-2:  $k_2$  in prismatic beam twisting [68]**

The elastic deflection  ${}^0_i \Delta \mathbf{X}_i$  observed in the local coordinate system  $O_i - x_i y_i z_i$  can be transformed to that  $\Delta \mathbf{X}_i$  of the reference coordinate system through a 6 by 6 transformation matrix  $\mathbf{J}_i$

$$\Delta \mathbf{X}_i = \mathbf{J}_i \cdot {}^0_i \Delta \mathbf{X}_i. \quad (3.7)$$

The transformation matrix  $\mathbf{J}_i$  can be derived as in [69]

$$\mathbf{J}_i = \begin{bmatrix} \mathbf{R}_i & -\mathbf{R}_i \mathbf{S}(\mathbf{r}_i) \\ \mathbf{0} & \mathbf{R}_i \end{bmatrix} \quad (3.8)$$

where  $\mathbf{R}_i$  denotes the rotation matrix of the local coordinate system with respect to the reference coordinate system,  $\mathbf{r}_i = \overline{O_i O} = [r_{ix}, r_{iy}, r_{iz}]^T$  is a position vector of the origin of the reference coordinate system with respect to the local coordinate system, and  $\mathbf{S}(\cdot)$  is a skew-symmetric operator representing

$$\mathbf{S}(\mathbf{r}_i) = \begin{bmatrix} 0 & -r_{iz} & r_{iy} \\ r_{iz} & 0 & -r_{ix} \\ -r_{iy} & r_{ix} & 0 \end{bmatrix}. \quad (3.9)$$

The transformation of the wrench exerted on the compliant element is given by [70] as

$${}^0_i \mathbf{F}_i = \mathbf{J}_i^T \cdot \mathbf{F}_i. \quad (3.10)$$

From (3.4) (3.7) and (3.10), the compliance matrix expressed in the reference coordinate system is

$$\mathbf{C} = \mathbf{J}_i \cdot {}^0_i \mathbf{C} \cdot \mathbf{J}_i^T. \quad (3.11)$$

Accordingly, noticing (3.5) one has

$$\mathbf{K} = \mathbf{J}_i^{-T} \cdot {}^0_i \mathbf{K} \cdot \mathbf{J}_i^{-1}. \quad (3.12)$$

### 3.3 Stiffness Modeling for One Leg

Three legs of the micromanipulator have similar kinematic structure, composed of a compliant universal joint, a compliant translational joint and a compliant spherical joint. In the next, the stiffness and compliance matrices of the micromanipulator will be calculated by using basic compliant elements firstly and then integrating them into a kinematic chain in preparation for the whole mechanism stiffness modeling.

#### 3.3.1 Stiffness Modeling of Compliant Universal Joint

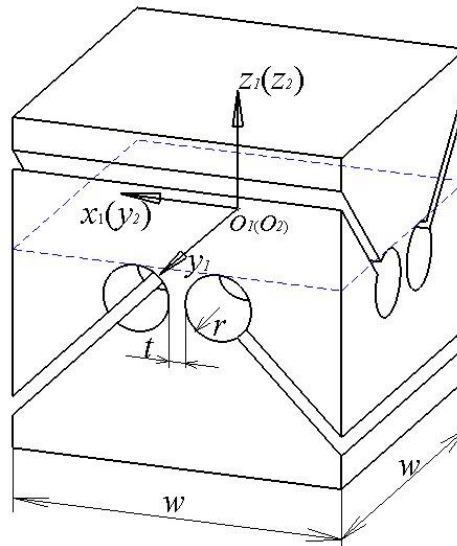


**Figure 3-2: Stiffness modeling of compliant universal joint**

The compliant translational joint as shown in Figure 3-2 is kinematically equivalent to two basic right circular hinges connected in sequence. For the purpose of stiffness analysis, two reference coordinate systems are established in terms of each componential right circular hinge following Figure 3-1. The origins of the two frames is located at the center of the cross-section plane which is bounded in dashed lines shown in Figure 3-2

and is tangent to circularly filleted outlines. Thus, the compliance matrices of two component hinges are

$$\mathbf{C}_1 = \mathbf{C}_2 = \mathbf{C}_{hinge} \quad (3.13)$$

### 3.3.2 Stiffness Modeling of Compliant Translational Joint

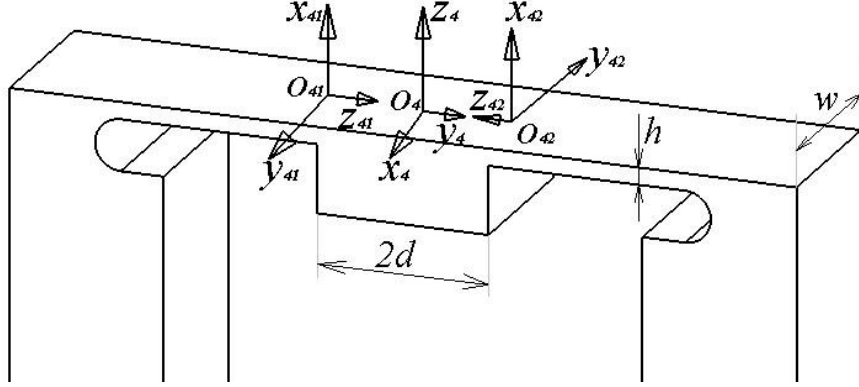


Figure 3-3: Stiffness modeling of upper end of the compliant translational joint

From Figure 3-3, the upper end of the CT includes two flexible cantilevers connected in parallel and the transformation matrices of their respective local coordinate systems  $O_{41} - x_{41}y_{41}z_{41}$  and  $O_{42} - x_{42}y_{42}z_{42}$  to the reference coordinate system  $O_4 - x_4y_4z_4$  are

$$\mathbf{J}_{41} = \begin{bmatrix} \mathbf{R}_z(-\frac{\pi}{2})\mathbf{R}_x(-\frac{\pi}{2}), -\mathbf{R}_z(-\frac{\pi}{2})\mathbf{R}_x(-\frac{\pi}{2})\mathbf{S}(\mathbf{r}_{41}) \\ \mathbf{0} \quad , \quad \mathbf{R}_z(-\frac{\pi}{2})\mathbf{R}_x(-\frac{\pi}{2}) \end{bmatrix}, \quad (3.14)$$

$$\mathbf{J}_{42} = \begin{bmatrix} \mathbf{R}_z(\frac{\pi}{2})\mathbf{R}_x(-\frac{\pi}{2}), -\mathbf{R}_z(\frac{\pi}{2})\mathbf{R}_x(-\frac{\pi}{2})\mathbf{S}(\mathbf{r}_{42}) \\ \mathbf{0} \quad , \quad \mathbf{R}_z(\frac{\pi}{2})\mathbf{R}_x(-\frac{\pi}{2}) \end{bmatrix}. \quad (3.15)$$

where  $\mathbf{r}_{41} = \overline{O_{41}O_4} = [0, 0, d]^T$  and  $\mathbf{r}_{42} = \overline{O_{42}O_4} = [0, 0, d]^T$ . Then the compliance matrices of these two cantilevers expressed in the coordinate system  $O_4 - x_4y_4z_4$  are

$$\mathbf{C}_{41} = \mathbf{J}_{41}\mathbf{C}_{beam}\mathbf{J}_{41}^T \quad \text{and} \quad \mathbf{C}_{42} = \mathbf{J}_{42}\mathbf{C}_{beam}\mathbf{J}_{42}^T. \quad (3.16)$$

The compliance matrix of the upper end of the CT is the summation of  $C_{41}$  and  $C_{42}$  :

$$C_4 = C_{41} + C_{42} \quad (3.17)$$

Since the compliant translational joint is structurally symmetric about a middle horizontal axis, stiffness analysis of the lower end of the CT as shown in Figure 3-4 can be analogously obtained:

$$C_3 = C_{31} + C_{32} = \mathbf{J}_{41} C_{beam} \mathbf{J}_{41}^T + \mathbf{J}_{42} C_{beam} \mathbf{J}_{42}^T. \quad (3.18)$$

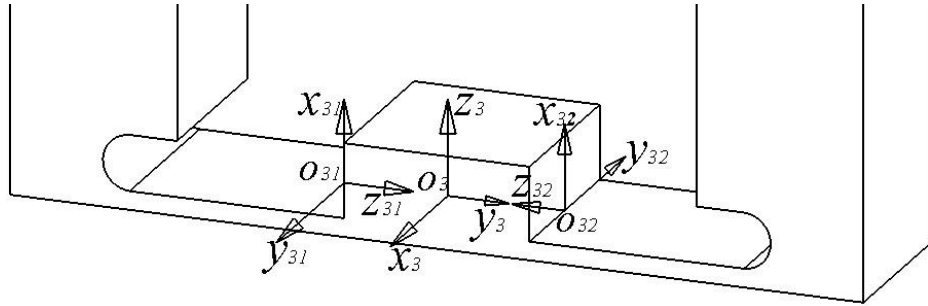


Figure 3-4: Stiffness modeling of lower end of the compliant translational joint

### 3.3.3 Stiffness Modeling of Compliant Spherical Joint

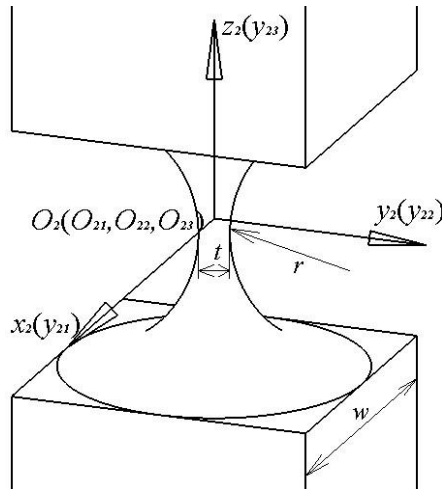


Figure 3-5: Stiffness modeling of compliant spherical joint

The compliant spherical joint in Figure 3-5 is kinematically equivalent to three right circular hinges connected serially achieving a combination of rotations around three

spatial orthogonal axes. The reference coordinate system  $O_5 - x_5 y_5 z_5$  is shown in Figure 3-5. Three local coordinate systems  $O_{51} - x_{51} y_{51} z_{51}$ ,  $O_{52} - x_{52} y_{52} z_{52}$  and  $O_{53} - x_{53} y_{53} z_{53}$  are established in such a way that their origins coincide with the origin of the reference coordinate system and  $y$ -axes are along three mutually orthogonal rotation axes as presented in Figure 3-5. Accordingly, the first two local  $z$ -axes are collinear with the  $z$ -axis of the reference coordinate system and the third one is along its  $x$ -axis. The local  $x$ -axes can be determined according to right hand law.

Noticing  $\mathbf{r}_{51} = \mathbf{r}_{52} = \mathbf{r}_{53} = \mathbf{0}$ , the three transformation matrices from each local coordinate system to the reference coordinate system are

$$\mathbf{J}_{51} = \begin{bmatrix} \mathbf{R}_z(-\frac{\pi}{2}), & \mathbf{0} \\ \mathbf{0} & \mathbf{R}_z(-\frac{\pi}{2}) \end{bmatrix} \quad (3.19)$$

$$\mathbf{J}_{52} = \begin{bmatrix} \mathbf{I} & \mathbf{0} \\ \mathbf{0} & \mathbf{I} \end{bmatrix} \quad (3.20)$$

$$\mathbf{J}_{53} = \begin{bmatrix} \mathbf{R}_x(\frac{\pi}{2})\mathbf{R}_y(\frac{\pi}{2}), & \mathbf{0} \\ \mathbf{0} & , \mathbf{R}_x(\frac{\pi}{2})\mathbf{R}_y(\frac{\pi}{2}) \end{bmatrix} \quad (3.21)$$

Then the compliance matrix of the compliant spherical joint expressed in the reference coordinate system  $O_5 - x_5 y_5 z_5$  is

$$\mathbf{C}_5 = \sum_{i=1}^3 \mathbf{C}_{5i} = \sum_{i=1}^3 \mathbf{J}_{5i} \mathbf{C}_{hinge} \mathbf{J}_{5i}^T \quad (3.22)$$

### 3.3.4 Stiffness Modeling of One Leg

When analyzing the stiffness or compliance matrix of a single leg, the transformation of each joint compliance matrix from the joint reference coordinate system to the leg reference coordinate system  $P$ - $xyz$  with the origin  $P$  placed at the center of the moving platform as shown in Figure 3-6 is needed. Based on the previous establishment of each joint reference coordinate system and continuing the previous notation, the compliance transformation matrices for leg 1 can be identified as:

$$\mathbf{J}_1 = \begin{bmatrix} \mathbf{I} & -\mathbf{S}(\mathbf{r}_1) \\ \mathbf{0} & \mathbf{I} \end{bmatrix}, \quad \mathbf{J}_2 = \begin{bmatrix} \mathbf{R}_z(\frac{\pi}{2}), -\mathbf{R}_z(\frac{\pi}{2})\mathbf{S}(\mathbf{r}_2) \\ \mathbf{0}, \mathbf{R}_z(\frac{\pi}{2}) \end{bmatrix}, \quad (3.23)$$

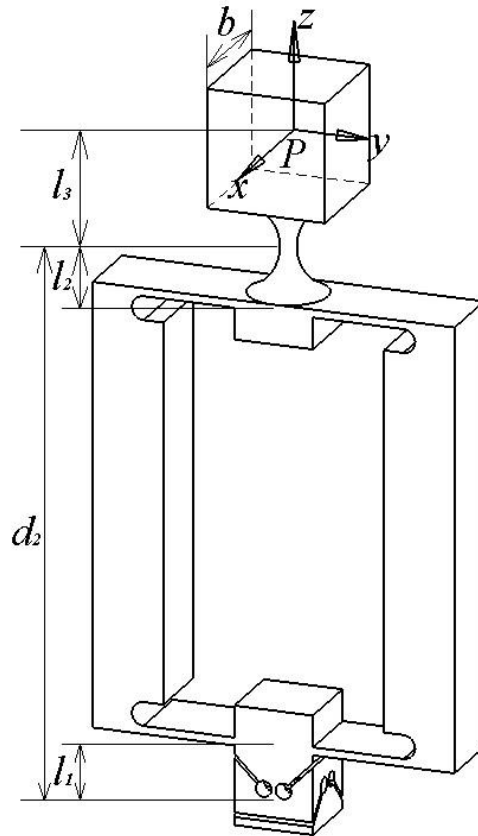


Figure 3-6: Stiffness analysis of leg 1

$$\mathbf{J}_3 = \begin{bmatrix} \mathbf{I} & -\mathbf{S}(\mathbf{r}_3) \\ \mathbf{0} & \mathbf{I} \end{bmatrix}, \quad \mathbf{J}_4 = \begin{bmatrix} \mathbf{I} & -\mathbf{S}(\mathbf{r}_4) \\ \mathbf{0} & \mathbf{I} \end{bmatrix}, \quad (3.24)$$

$$\mathbf{J}_5 = \begin{bmatrix} \mathbf{I} & -\mathbf{S}(\mathbf{r}_5) \\ \mathbf{0} & \mathbf{I} \end{bmatrix}, \quad (3.25)$$

where the position vectors are

$$\mathbf{r}_1 = \mathbf{r}_2 = [0, 0, d_i + l_3]^T, \quad (3.26)$$

$$\mathbf{r}_3 = [0, 0, d_i - l_1 + l_3]^T, \quad \mathbf{r}_4 = [0, 0, l_2 + l_3]^T, \quad (3.27)$$

$$\mathbf{r}_5 = [0, 0, l_3]^T. \quad (3.28)$$

The compliance matrix of leg 1 expressed in the leg reference coordinate system  $P$ -xyz takes the form

$$\mathbf{C}_{l1} = \mathbf{J}_{l1} \mathbf{C}^* \mathbf{J}_{l1}^T. \quad (3.29)$$

where  $\mathbf{J}_{l1} = [\mathbf{J}_1 \mathbf{J}_2 \mathbf{J}_3 \mathbf{J}_4 \mathbf{J}_5]_{6 \times 30}$  incorporates the five transformation matrices of joints and

$\mathbf{C}^* = \text{diag}(\mathbf{C}_1, \mathbf{C}_2, \mathbf{C}_3, \mathbf{C}_4, \mathbf{C}_5)$  is a  $30 \times 30$  diagonal matrix.

Likewise, the compliance matrix associated with the other two legs can be determined and a minor difference in the transformation matrices are going to be shown as follows.

For leg 2, one has

$$\mathbf{J}_1 = \begin{bmatrix} \mathbf{R}_x(-\frac{\pi}{2}) & -\mathbf{R}_x(-\frac{\pi}{2})\mathbf{S}(\mathbf{r}_1) \\ \mathbf{0} & \mathbf{R}_x(-\frac{\pi}{2}) \end{bmatrix}, \quad \mathbf{J}_2 = \begin{bmatrix} \mathbf{R}_x(-\frac{\pi}{2})\mathbf{R}_z(\frac{\pi}{2}), -\mathbf{R}_x(-\frac{\pi}{2})\mathbf{R}_z(\frac{\pi}{2})\mathbf{S}(\mathbf{r}_2) \\ \mathbf{0} & \mathbf{R}_x(-\frac{\pi}{2})\mathbf{R}_z(\frac{\pi}{2}) \end{bmatrix}, \quad (3.30)$$

$$\mathbf{J}_3 = \begin{bmatrix} \mathbf{R}_x(-\frac{\pi}{2}) & -\mathbf{R}_x(-\frac{\pi}{2})\mathbf{S}(\mathbf{r}_3) \\ \mathbf{0} & \mathbf{R}_x(-\frac{\pi}{2}) \end{bmatrix}, \quad \mathbf{J}_4 = \begin{bmatrix} \mathbf{R}_x(-\frac{\pi}{2}) & -\mathbf{R}_x(-\frac{\pi}{2})\mathbf{S}(\mathbf{r}_4) \\ \mathbf{0} & \mathbf{R}_x(-\frac{\pi}{2}) \end{bmatrix}, \quad (3.31)$$

$$\mathbf{J}_5 = \begin{bmatrix} \mathbf{R}_x(-\frac{\pi}{2}) & -\mathbf{R}_x(-\frac{\pi}{2})\mathbf{S}(\mathbf{r}_5) \\ \mathbf{0} & \mathbf{R}_x(-\frac{\pi}{2}) \end{bmatrix}. \quad (3.32)$$

Therefore, the compliance matrix of leg 2 expressed in the leg reference coordinate system  $P$ -xyz is

$$\mathbf{C}_{l2} = \mathbf{J}_{l2} \mathbf{C}^* \mathbf{J}_{l2}^T. \quad (3.33)$$

For leg 3, one has

$$\mathbf{J}_1 = \begin{bmatrix} \mathbf{R}_y(\frac{\pi}{2}) & -\mathbf{R}_y(\frac{\pi}{2})\mathbf{S}(\mathbf{r}_1) \\ \mathbf{0} & \mathbf{R}_y(\frac{\pi}{2}) \end{bmatrix}, \quad \mathbf{J}_2 = \begin{bmatrix} \mathbf{R}_y(\frac{\pi}{2})\mathbf{R}_z(\frac{\pi}{2}), -\mathbf{R}_y(\frac{\pi}{2})\mathbf{R}_z(\frac{\pi}{2})\mathbf{S}(\mathbf{r}_2) \\ \mathbf{0} & \mathbf{R}_y(\frac{\pi}{2})\mathbf{R}_z(\frac{\pi}{2}) \end{bmatrix}, \quad (3.34)$$

$$\mathbf{J}_3 = \begin{bmatrix} \mathbf{R}_y(\frac{\pi}{2}) & -\mathbf{R}_y(\frac{\pi}{2})\mathbf{S}(\mathbf{r}_3) \\ \mathbf{0} & \mathbf{R}_y(\frac{\pi}{2}) \end{bmatrix}, \quad \mathbf{J}_4 = \begin{bmatrix} \mathbf{R}_y(\frac{\pi}{2}) & -\mathbf{R}_y(\frac{\pi}{2})\mathbf{S}(\mathbf{r}_4) \\ \mathbf{0} & \mathbf{R}_y(\frac{\pi}{2}) \end{bmatrix}, \quad (3.35)$$

$$\mathbf{J}_5 = \begin{bmatrix} \mathbf{R}_y(\frac{\pi}{2}) & -\mathbf{R}_y(\frac{\pi}{2})\mathbf{S}(\mathbf{r}_5) \\ \mathbf{0} & \mathbf{R}_y(\frac{\pi}{2}) \end{bmatrix}. \quad (3.36)$$

Hence, the compliance matrix of leg 3 expressed in the leg reference coordinate system  $P$ -xyz is

$$\mathbf{C}_{l3} = \mathbf{J}_{l3} \mathbf{C}^* \mathbf{J}_{l3}^T. \quad (3.37)$$

### 3.4 Stiffness Modeling for 3-UPS CPM

For a compliant parallel manipulator with  $n$  compliant serial chains, the stiffness matrix is given in [67] as

$$\mathbf{K} = \sum_{i=1}^n \mathbf{J}_{ci}^{-T} \mathbf{K}_{li} \mathbf{J}_{ci}^{-1} \quad (3.38)$$

where  $\mathbf{J}_{ci}$  is the transformation matrix of the  $i$ th leg from the leg reference coordinate system to the overall reference coordinate system,  $\mathbf{K}_{li}$  is the stiffness matrix of the corresponding leg expressed in the leg reference coordinate system.

Following previous sections, the overall reference coordinate system can be selected as the coordinate system  $P$ -xyz which is same as the leg reference coordinate system and thus simplifies the analysis process. Consequently,  $\mathbf{J}_{ci}(i=1,2,3)$  become identity matrices and the stiffness matrix for the 3-UPS CPM becomes

$$\mathbf{K}_P = \sum_{i=1}^3 \mathbf{K}_{li} \quad (3.39)$$

Since the stiffness and compliance matrices have a close relationship as shown in (3.5), it is easy to switch between two:

$$\mathbf{C} = \mathbf{K}^{-1} = \sum_{i=1}^n \mathbf{J}_{ci} \mathbf{C}_{li} \mathbf{J}_{ci}^T. \quad (3.40)$$

Furthermore, the stiffness matrix with respect to other overall reference coordinate system can be also derived based on the knowledge of  $\mathbf{K}_P$ . For instance, the stiffness matrix in another overall coordinate system  $E$ -xyz that lies right above the  $P$ -xyz and in the top plane of the moving platform, can be described as

$$\mathbf{K}_E = \mathbf{J}_P^{-T} \mathbf{K}_P \mathbf{J}_P^{-1}, \quad (3.41)$$

where

$$\mathbf{J}_P = \begin{bmatrix} \mathbf{I} & -\mathbf{S}(\mathbf{r}) \\ \mathbf{0} & \mathbf{I} \end{bmatrix} (\mathbf{r} = \overline{PE}). \quad (3.42)$$

### 3.5 Compliance Mapping

The overall stiffness model developed for the 3-UPS compliant micromanipulator is now adopted to obtain the mapping among the compliance and the structural parameters. Keeping two structural parameters of interest varying within a certain range and simultaneously others constant can facilitate compliance mesh and contour graphs, which helps to intuitively observe the tendency of compliance change and assess the influence of each structural parameter.

In these figures (Figure 3-7 through Figure 3-12), based on [71] the compliance factors are derived from the diagonal elements of overall compliance matrix shown in equation (3-41). They represent the pure compliance in each direction, which reflect the compliance of the micromanipulator more directly and clearly.

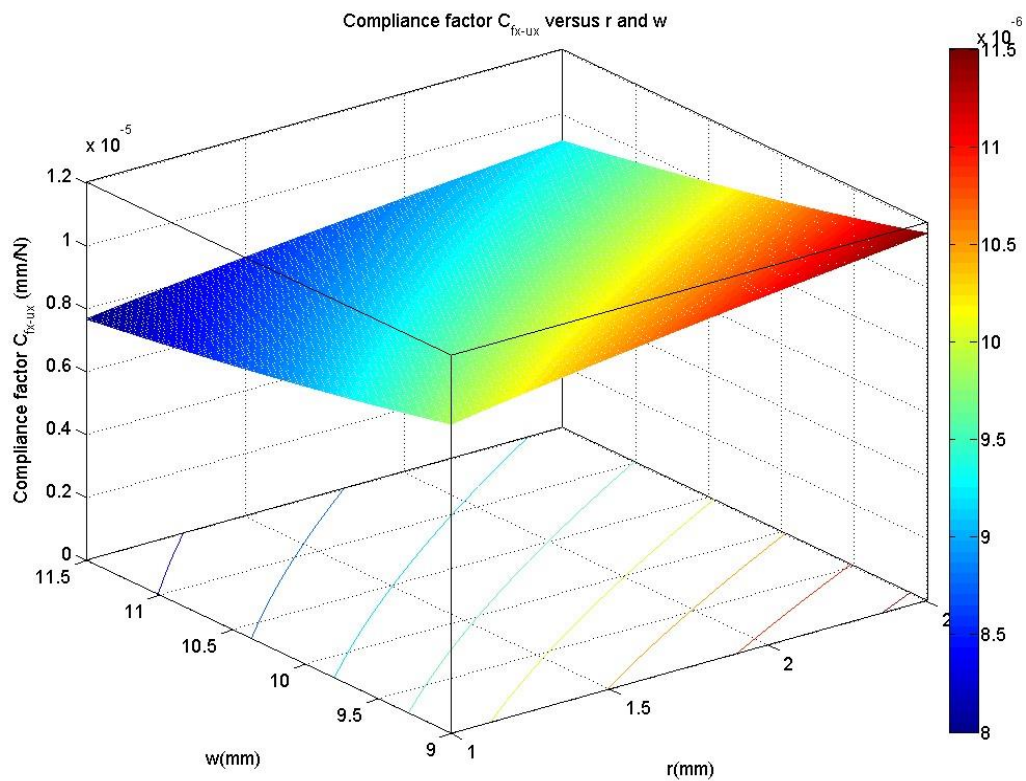


Figure 3-7: Compliance mapping of factor  $C_{fx-ux}$  versus  $w$  and  $r$

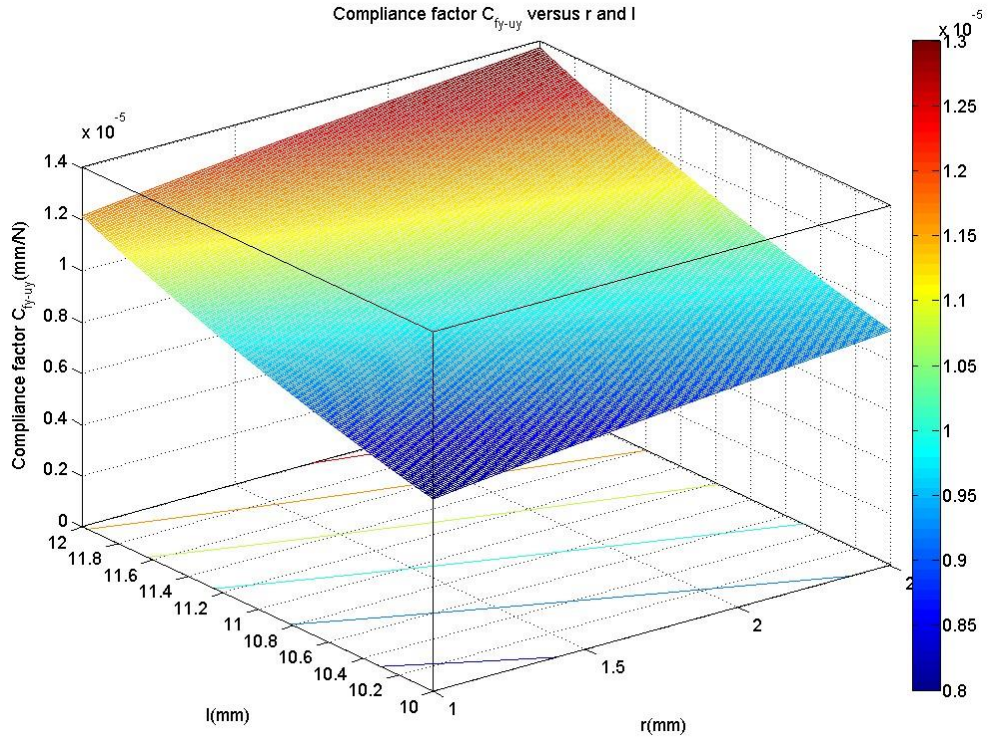


Figure 3-8: Compliance mapping of factor  $C_{fy-uy}$  versus  $r$  and  $l$

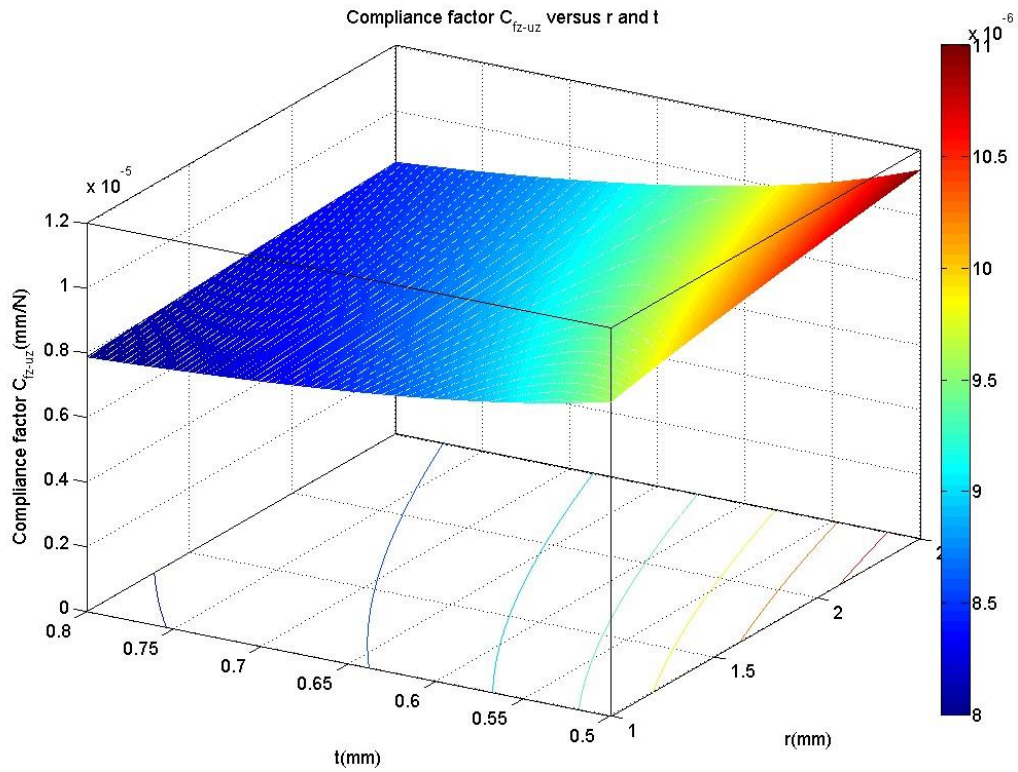


Figure 3-9: Compliance mapping of factor  $C_{fz-uz}$  versus  $r$  and  $t$

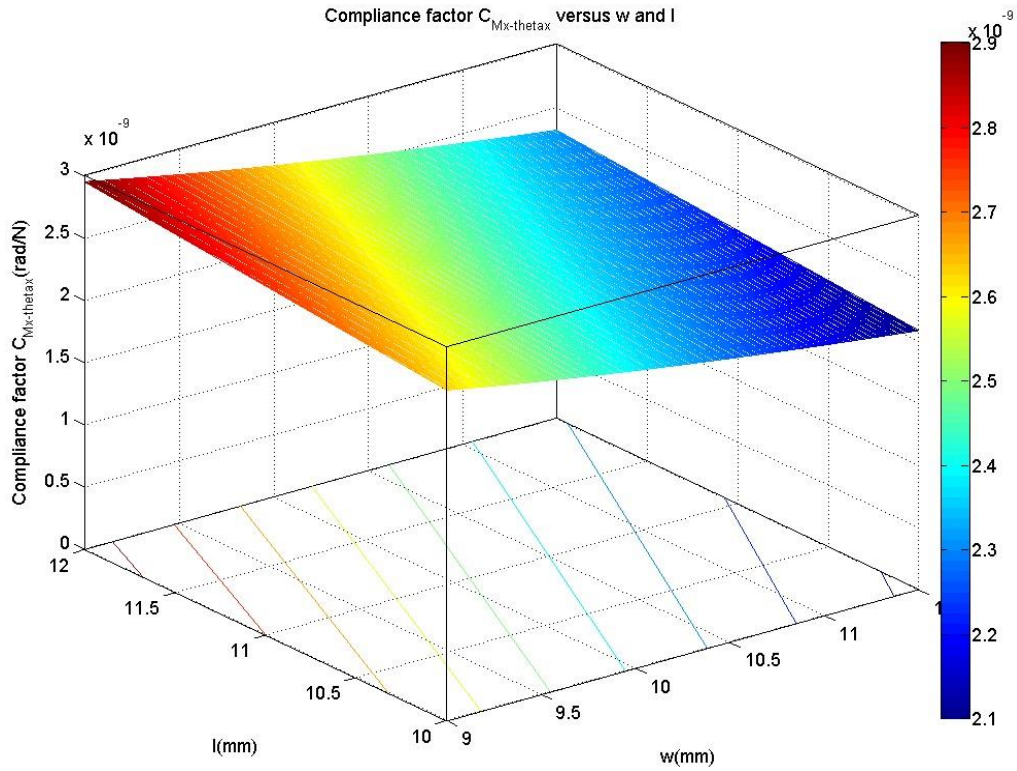


Figure 3-10: Compliance mapping of factor  $C_{Mx-\theta_x}$  versus  $w$  and  $l$

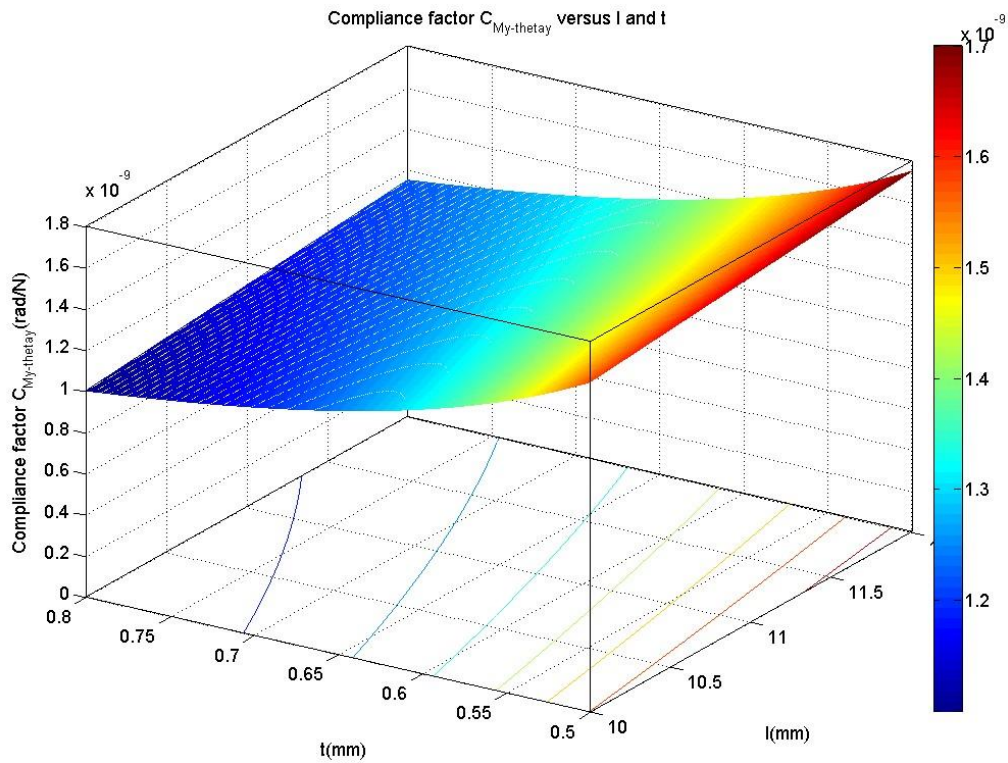
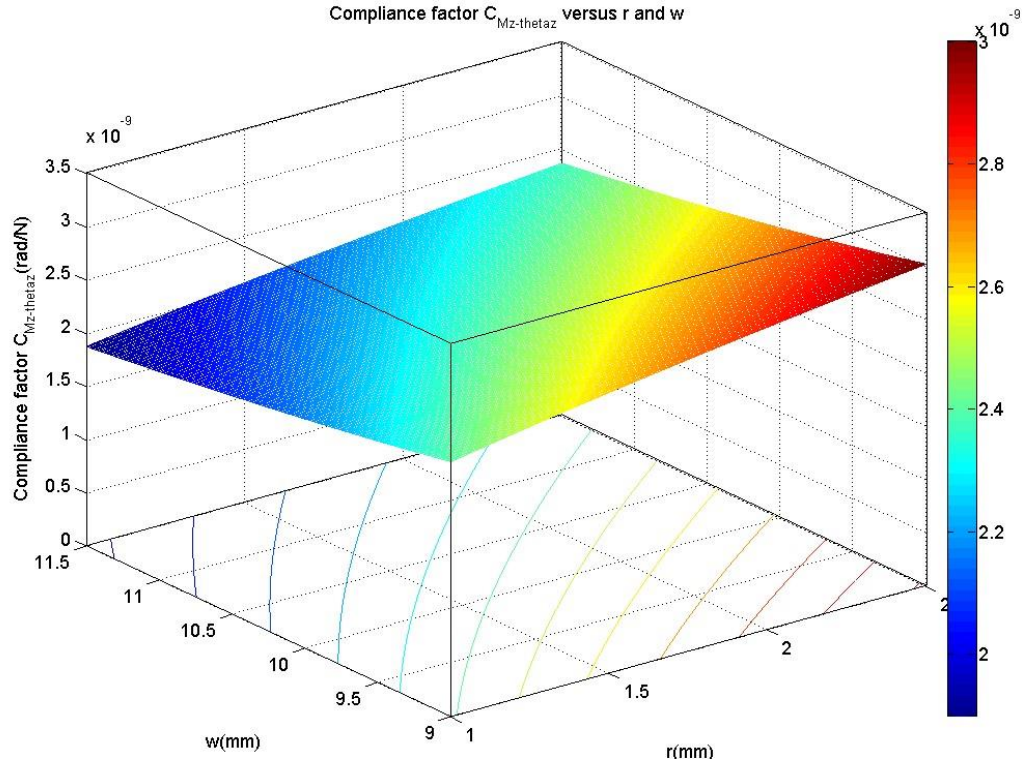


Figure 3-11: Compliance mapping of factor  $C_{My-\theta_y}$  versus  $l$  and  $t$



**Figure 3-12: Compliance mapping of factor  $C_{Mz-\theta_z}$  versus  $r$  and  $w$**

### 3.6 Conclusions

Stiffness is an important criterion of manipulator design and higher stiffness ensures higher accuracy of the moving platform. Due to the characteristics of the compliant mechanism, the process of stiffness analysis takes three levels: compliant joints, one single leg and the overall micromanipulator. The analytical form of the overall stiffness of the micromanipulator is obtained following these steps. Additionally, the compliance mapping reflecting the relationship of compliance and structural variables is shown graphically. This chapter also forms the basis for further optimization of the design variables for higher stiffness.

# Chapter 4

## Workspace Evaluation

### 4.1 Introduction

Workspace is where the moving platform of a manipulator implements specific tasks and its volume size determines the work range and capability. Workspace is usually defined as a reachable space inside which every point can be reached in terms of the reference point of the moving platform and it is one of the most important criteria for evaluating manipulator's performance.

Generally, compared with their serial counterparts parallel manipulators are capable of a relatively small workspace and thus their working capacity is largely limited. A lot of studies have been directed at analysis of the shape and volume of the workspace aiming to enhance parallel manipulator applications.[72-74] In this study, the workspace volume of the micromanipulator is desired as small as possible because that means the manipulator can implement an extremely micro manipulation which is exactly needed for micro- and even nano- applications.

In the current chapter, the workspace evaluation of the micromanipulator will be conducted based on a methodology presented in [75] and through a prototype the shape and volume of the micromanipulator's workspace will be also numerically calculated and graphically presented by a developed Matlab program (see Appendix A). Since the workspace is influenced by several factors such as actuator stroke and limitation of compliant joints' displacement, the constraints will be clarified first so that consequent computational calculation and visualization can be facilitated. The aim is to obtain a basic sense of the volume and shape of the micromanipulator workspace.

## 4.2 Formulation of Workspace Constraints

### 4.2.1 Constraint Set I: Leg Length Limit

Assume the CTJs are displaced by PZT actuators whose stroke is  $s$  and originally the PZT actuators are in the half stroke with the leg length being  $d_0$ . Then, the leg lengths must satisfy

$$d_0 - \frac{s}{2} < d_i < d_0 + \frac{s}{2} \quad (i = 1, 2, 3) \quad (4.1)$$

The equation above describes the physical limit exerted on each of three leg lengths.

### 4.2.2 Constraint Set II: Compliant Joint Angular Limit

The compliant joint angular limit can be obtained according to mechanics of the material in analyzing the compliant elements. Let  $\delta_{\max}$  be the maximum angular displacement of compliant flexural hinges (see Figure 3-1) with respect to their normal position. The

maximum angular deflection  $\delta_{\max}$  occurs accompanying the maximum stress  $\sigma_{\max}$  which is actually the yield strength of the material adopted for the compliant element. Referring to the point that is farthest from the neutral axis in the cross section with the minimum thickness  $t$ , one can write [76]

$$\sigma_{\max} = \frac{M \cdot (t/2)}{I} = \frac{K\delta_{\max} \cdot (t/2)}{I} = \sigma_y \quad (4.2)$$

where  $I = \frac{ht^3}{12}$  is the moment of inertia of the cross-sectional area about the neutral axis,  $\sigma_y$  is the yield strength of material, and the stiffness  $K$  can be calculated from [77]

$$K = \frac{2Eht^{\frac{5}{2}}}{9\pi r^{\frac{1}{2}}}. \quad (4.3)$$

Then, the following can be derived:

$$\delta_{\max} = \frac{3\pi r^{\frac{1}{2}}\sigma_y}{4Et^{\frac{1}{2}}}. \quad (4.4)$$

Therefore, the compliant angular displacement  $\delta_i$  must satisfy the constraint:

$$-\delta_{\max} < \delta_i < \delta_{\max}. \quad (4.5)$$

### 4.3 Computer Implementation

The algorithm adopted in this thesis for workspace evaluation is developed with the aid of Matlab software. Referring to [75], the complete implementation in this study contains five steps:

1. Define a testing function that is able to test the validity of a point and returns the evaluation result in the form of either true or false;

2. Perform a search to find an approximate workspace center;
3. Perform an error criterion to decide the workspace boundary;
4. Determine the workspace volume;
5. Graphically visualize the workspace.

### 4.3.1 Formulation of Testing Function

The testing function is a Boolean function that is used to test a point at which whether the position and orientation of the moving platform meets the constraints via inverse kinematics calculation. For a given pose of the moving platform, say, the position vector  $\mathbf{p}$  and the rotation matrix  ${}^o\mathbf{R}_p$ , the testing function takes the form

$$\text{True(or False)} = \text{TestPose}(\mathbf{p}, {}^o\mathbf{R}_p). \quad (4.6)$$

The function actually computes the inverse kinematic equations (2.23) through (2.25) and ensures that the leg length limit and the compliant angle deflection limit hold. If both of the constraints are satisfied, the function returns true value. Otherwise, it returns a value of false. Also, one can understand it in the way that the value of true obtained by the function  $\text{TestPose}(\ )$  tells that the given position and orientation of the moving platform can be reached by the reference point of the moving platform.

### 4.3.2 Determination of Workspace Search Center and Vector

The workspace search algorithm works by searching numerous points to determine the workspace of the micromanipulator with a given orientation, say in the Pitch-Roll-Yaw Euler Angles representation [78]

$$\begin{aligned} \mathbf{R}_{PRY}(\alpha, \beta, \gamma) &= \mathbf{R}_z(\gamma)\mathbf{R}_y(\beta)\mathbf{R}_x(\alpha) \\ &= \begin{bmatrix} c\beta c\gamma & s\alpha s\beta c\gamma - c\alpha s\gamma & c\alpha s\beta c\gamma + s\alpha s\gamma \\ c\beta s\gamma & s\alpha s\beta s\gamma + c\alpha c\gamma & c\alpha s\beta s\gamma - s\alpha c\gamma \\ -s\beta & s\alpha c\beta & c\alpha c\beta \end{bmatrix}. \end{aligned} \quad (4.7)$$

What first needs to do is to determine an approximate workspace center to initialize the workspace search. This can be accomplished by searching a 3-D grid comprising all possible positions of the reference point of the moving platform within the work volume of the micromanipulator. For the positions located at the center of the cuboid in grid, the TestPose( ) function is utilized to check for all constraint violations. The approximate center of the workspace can be decided from all point results obtained by the test function.

The approximate workspace center is mainly used as the origin of a spherical coordinate system which helps to define the actual workspace boundary. The process of how it works is as follows. As demonstrated in Figure 4-1, the workspace search vector  $\mathbf{v}$  is defined in the spherical coordinate system as  $\mathbf{v} = \{\rho, \theta, \phi\}$ . To achieve searching the entire space, the search vector rotates in discrete intervals  $\Delta\theta$  and  $\Delta\phi$ . The search vector is considered to be on or close to the workspace boundary when the following conditions are met:

$$\begin{aligned} \text{TestPose}(\rho, \theta, \phi, \mathbf{R}_{PRY}) &= \text{TRUE} \\ \text{TestPose}(\rho + \varepsilon, \theta, \phi, \mathbf{R}_{PRY}) &= \text{FALSE} \end{aligned} \quad (4.8)$$

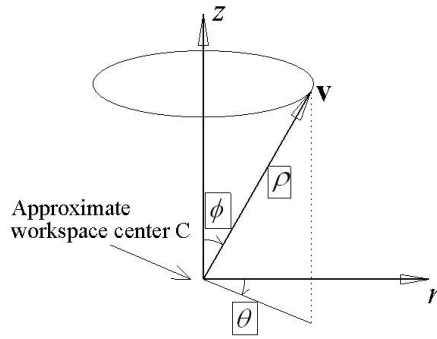


**Figure 4-1: Definition of workspace search vector**

The algorithm of expanding the search vector expressed in pseudo code:

```
 $\theta = 0^\circ$   
loop while  $\theta < 360^\circ$   
   $\phi = 0^\circ$   
  loop while  $\phi < 180^\circ$   
    find  $\rho$  that satisfying (4.8)  
     $\phi = \phi + \Delta\phi$   
  end loop  
   $\theta = \theta + \Delta\theta$   
end loop
```

Figure 4-2: Pseudo code of expanding the search vector

### 4.3.3 Workspace Boundary Search

The workspace search algorithm is mainly predicated on searching a  $\rho$  that represents the boundary of the workspace. As a successive approximation approach, the workspace boundary algorithm can be further utilized based on an assumption that if a point  $P(\theta, \phi, \rho_1)$  violates the constraints, all points having  $\rho_2 > \rho_1$  will violate the constraints as well.

At the final stage of the workspace boundary search process, Figure 4-3 shows the variation of the search vector  $\mathbf{v}$  in order to help assess the accuracy of the search result.

The search vector  $\mathbf{v}$  changes the length  $\rho$  until  $\Delta\rho \leq \frac{\varepsilon}{2}$ , where  $\varepsilon$  guarantees that  $\rho$  is within a deviation of  $\pm\varepsilon$  with respect to the workspace boundary. If necessary, subtract the final value of  $\rho$  by  $\varepsilon$  to guarantee that the search vector  $\mathbf{v}$  is within the workspace boundary. The error of such a search algorithm at every point is between 0 and  $-\varepsilon$ . Figure 4-4 shows the pseudo code of the workspace boundary search algorithm.

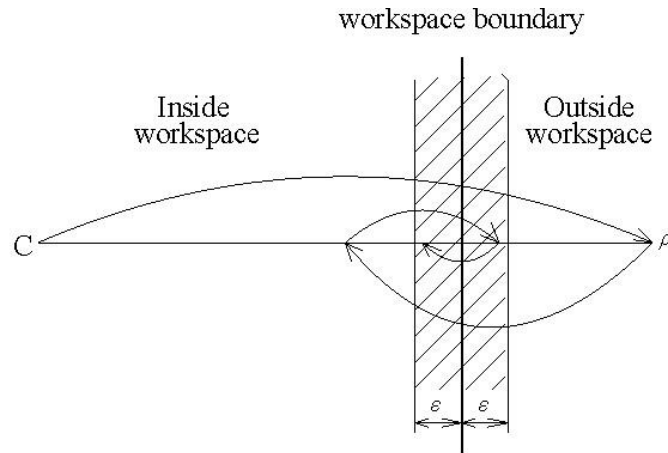


Figure 4-3: Variation of workspace boundary search vector [75]

```

Give  $\rho$  a value beyond the workspace
 $\Delta\rho = \frac{\rho}{2}$ 
loop while  $\Delta\rho < \frac{\varepsilon}{2}$ 
  if TestPose( $\theta, \phi, \rho, R_{PRY}$ ) = TRUE
     $\rho = \rho + \Delta\rho$ 
  otherwise
     $\rho = \rho - \Delta\rho$ 
   $\Delta\rho = \frac{\Delta\rho}{2}$ 
end loop
if TestPose( $\theta, \phi, \rho, R_{PRY}$ ) = FALSE
   $\rho = \rho - \varepsilon$ 

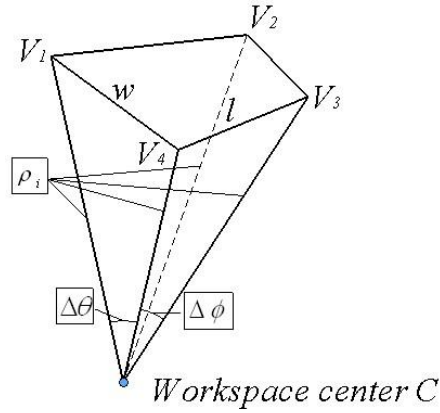
```

Figure 4-4: Pseudo code of workspace boundary search algorithm [75]

#### 4.3.4 Workspace Volume Evaluation

The workspace obtained eventually is defined by a lot of boundary points around the search origin C. To evaluate its volume, the calculation method is mainly based on accumulation. Define a sector by four adjacent workspace data points  $V_1, V_2, V_3, V_4$  and the

workspace search origin C as shown in Figure 4-5. Then by summing the volume of all unique sectors, the total volume of the workspace can be determined.



**Figure 4-5: Volume calculation of a sector of workspace**

The volume of the sector can be regarded as a four-sided pyramid whose volume can be calculated in five steps [75]:

1. Determine the average length of the four edges

$$\rho_{ave} = \frac{\rho_1 + \rho_2 + \rho_3 + \rho_4}{4}. \quad (4.9)$$

2. Approximate the arc lengths as the two adjacent edges of the bottom plane of the pyramid

$$l = \Delta\phi \cdot \rho_{ave}, \quad w = \Delta\theta \cdot \rho_{ave}. \quad (4.10)$$

3. The height of the pyramid can be determined in this way:

$$h = \sqrt{\rho_{ave}^2 - \frac{l^2 + w^2}{2}}. \quad (4.11)$$

4. The volume of the sector can be computed in the way of calculating that of a pyramid

$$V = \frac{1}{3} \cdot lwh. \quad (4.12)$$

5. The total workspace volume is obtained by the summation of volume of all individual sectors

$$V_w = \sum_{i=1}^n V_i . \quad (4.13)$$

## 4.4 Discussion of Results and Plots

Based on the method presented in the previous sections, implementation for micromanipulator workspace analysis is conducted in Matlab environment. Through a spherical coordinate search and inverse kinematic check, 65,160 points are found to show the workspace boundary definition for a certain orientation of the moving platform. All these points are obtained from the perspective of the reference point  $P$  of the moving platform. Four typical orientations, namely in Pitch-Roll-Yaw form  $\mathbf{R}_{PRY}(0^\circ, 0^\circ, 0^\circ)$ ,  $\mathbf{R}_{PRY}(5^\circ, 0^\circ, 0^\circ)$ ,  $\mathbf{R}_{PRY}(0^\circ, 5^\circ, 0^\circ)$ ,  $\mathbf{R}_{PRY}(0^\circ, 0^\circ, 5^\circ)$  and the corresponding workspace are studied. To make the workspace shape visually available and help to learn the basic properties of the workspace, each case is graphically plotted as shown in Figure 4-6 through Figure 4-9.

As noticed in all these plots, the workspace is basically cuboid-shaped which results from the mutually orthogonal arrangement of three legs of the micromanipulator. The coordinates of all these boundary points are with respect to the fixed coordinate system as established in section 2.2. The PZT actuators are chosen as the drivers which are embedded in CTJs due to their high accuracy and fast response. They have a stroke of  $280 \mu m$  and resolution of  $1.4 nm$ . The original position of the reference point  $P$  of the moving platform is  $(89.5, 89.5, 89.5)$  with the three PZT actuators in half stroke. A

comparison of workspace parameters for different orientations under study is made in Table 4-1.

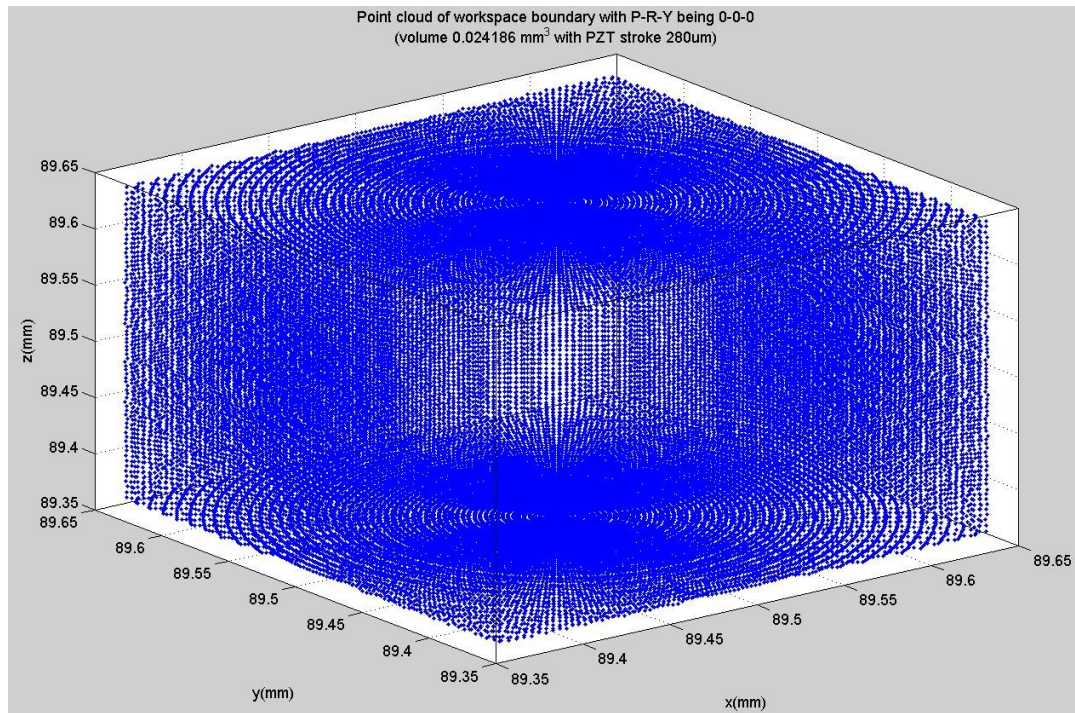


**Figure 4-6: Point cloud of workspace boundary with orientation of  $\mathbf{R}_{PRY}(0^\circ, 0^\circ, 0^\circ)$**

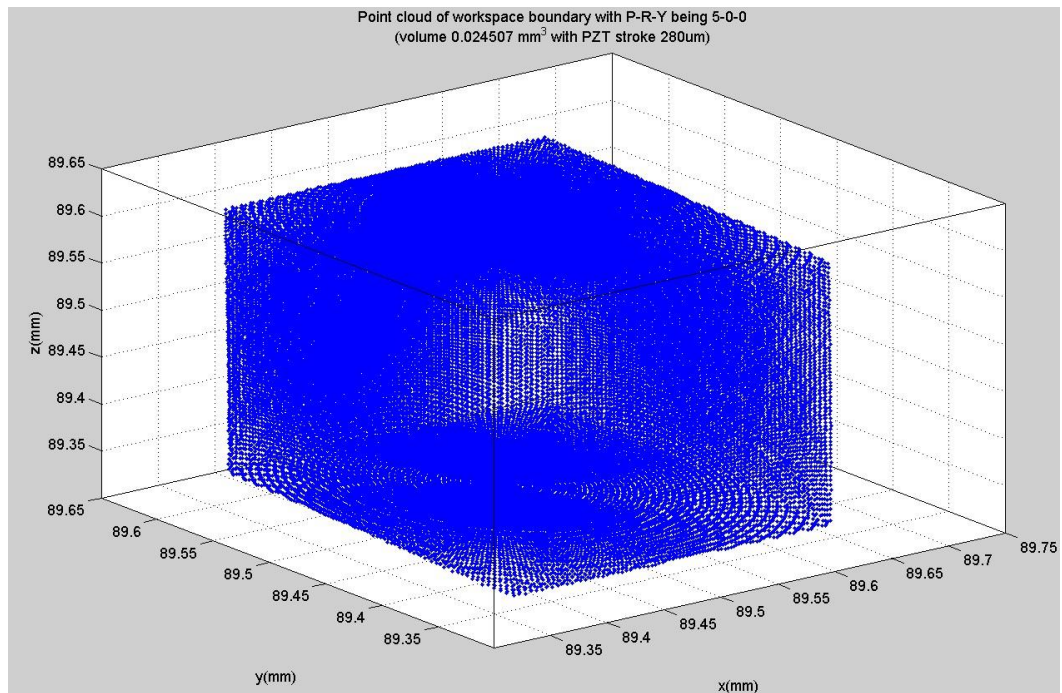


**Figure 4-7: Point cloud of workspace boundary with orientation of  $\mathbf{R}_{PRY}(5^\circ, 0^\circ, 0^\circ)$**

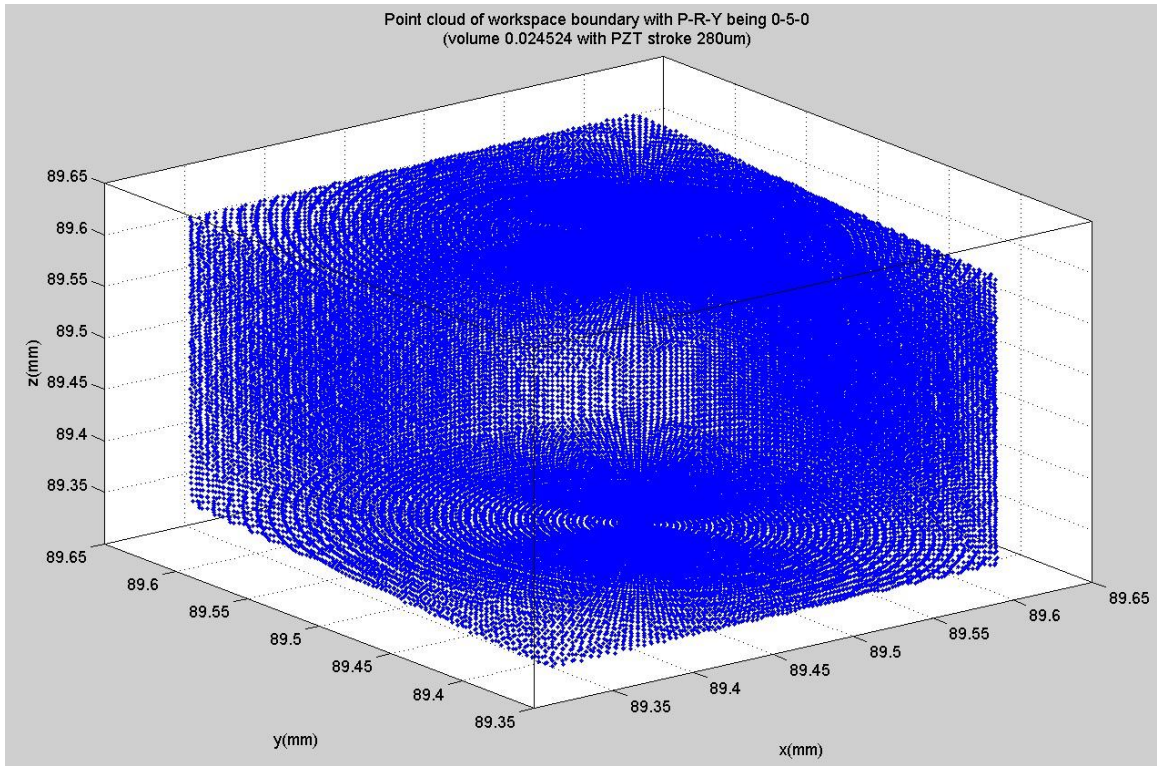


**Figure 4-8: Point cloud of workspace boundary with orientation of  $R_{PRY}(0^\circ, 5^\circ, 0^\circ)$**

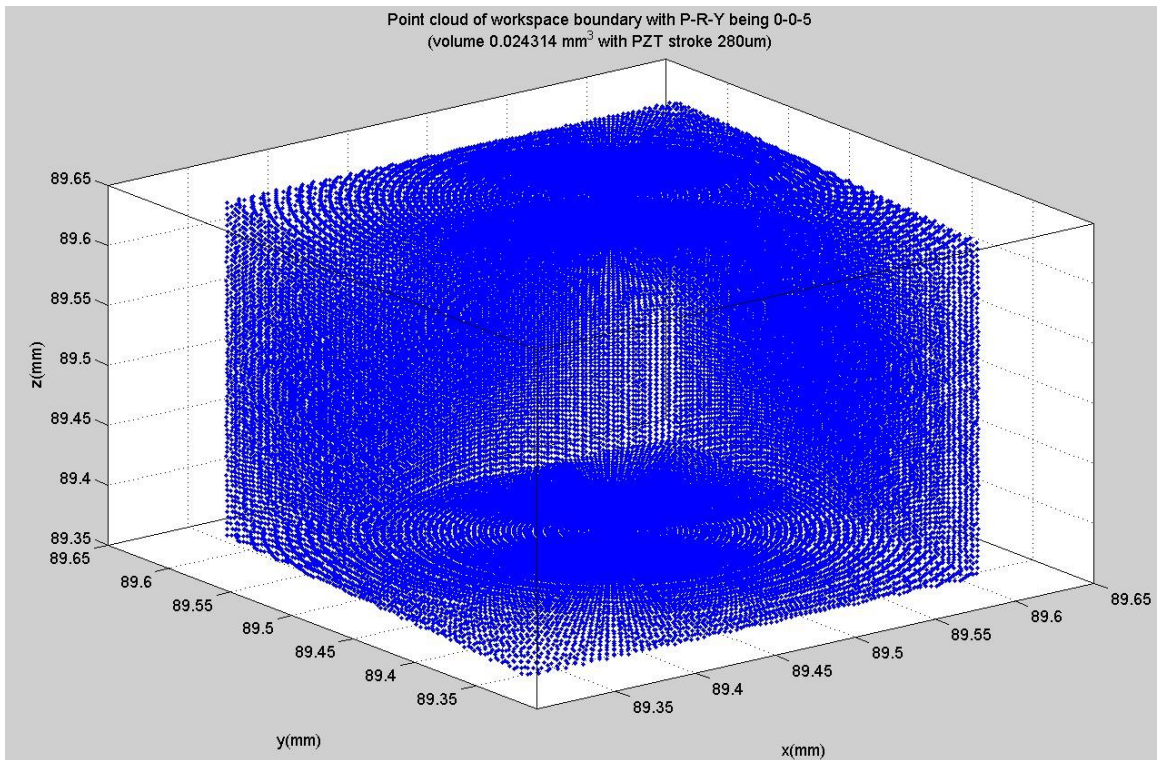


**Figure 4-9: Point cloud of workspace boundary with orientation of  $R_{PRY}(0^\circ, 0^\circ, 5^\circ)$**

Orientations (Pitch-Roll-Yaw)	Characteristic parameters of workspace			
	x range (mm)	y range (mm)	z range (mm)	vol (mm <sup>3</sup> )
(0°,0°,0°)	89.6534- 89.3464	89.6404- 89.3596	89.6402- 89.3596	0.024186
(5°,0°,0°)	89.6506- 89.3436	89.6099- 89.3270	89.6100- 89.3278	0.024507
(0°,5°,0°)	89.6259- 89.3173	89.6404- 89.3595	89.6099- 89.3270	0.024524
(0°,0°,5°)	89.6243- 89.3175	89.6101- 89.3277	89.6402- 89.3596	0.024314

**Table 4-1: Comparison of workspace parameters for different orientations**

## 4.5 Conclusions

In this chapter, problems associated with workspace evaluation of the micromanipulator have been explored. The motion of the moving platform is confined mainly by its structural constraints. In order to determine the workspace, a search method for boundary points is adopted in which the inverse kinematics discussed in Chapter 2 plays a key role. Through Matlab program developed by following the workspace search algorithm, the shape and corresponding properties such as the volume, boundary range are studied.

# Chapter 5

## Optimization of Micromanipulator

### 5.1 Introduction

Optimization plays a crucial role in addressing engineering design problems in which it copes with maximizing or minimizing an objective function with a couple of design variables. For the micromanipulator studied here, higher end-effector's stiffness and well-conditioned workspace are desired. Because higher stiffness achieves higher rigidity and minor deflections and thus it ensures a higher manipulation precision. Well-conditioned workspace represents the quality of micromanipulation within the range of the workspace, including the dexterity and manipulability at each point within the workspace and also including improved accuracy due to the optimized amplification error between the actuators and the end-effector.

In this chapter, the focus is placed on the optimization of design variables with respect to two optimization criteria. Single-objective optimization for each criterion will be implemented first to know the relationship of design variables with different

performance criteria when considering only one performance. Then with more practical significance, a multi-objective optimization considering several objectives together will be aimed to provide acceptable trade-offs for decision-makers. Since the optimization issue discussed here is non-linear and multi-variable based, an optimization technique called Firefly Algorithm is applied and will be illustrated first. Then based on the establishment of two optimization criteria, optimizations for different objective functions are performed in the Matlab environment and illustrative graphics for explaining results are provided.

For manipulator optimization problems, the objective functions are closely related to the topology and geometry of the manipulator, the general methodology of optimization features these following steps:[79]

1. Analyse requirements, such as stiffness, mechanical interference and workspace properties, etc.
2. Analyse constraints, like geometric size and properties;
3. Create a reasonable initial guess of the mechanism geometry and then use a numerical optimization to further improve kinematic properties so as to obtain optimal characteristics.
4. Eventually, a developed program offers a potential solution to allow verifying the important properties.

In this chapter, following the above procedure, the optimization study of the micromanipulator is explored.

## 5.2 Firefly Algorithm

### 5.2.1 Firefly Behaviour and Firefly Algorithm

Firefly Algorithm (hereafter FA) is a nature-inspired algorithm newly developed by Xinsheng Yang for multimodal optimization applications.[80] Not like Genetic Algorithm, the FA is much simpler and it does not involve mutation and crossover operators. Instead, it utilizes real-number randomness and global attractiveness among fireflies. Particle Swarm Optimization developed by Kennedy and Eberhart [81] is also a popular metaheuristic algorithm but it is proved that PSO is just a special class of the FA. In dealing with multimodal functions, FA is more promising and behaves more naturally and efficiently.

The way the FA works mainly relies on the characteristic behaviours of fireflies to converge to a global solution. The flashing light is typical of fireflies and it has certain functions in firefly species. The notable one is to attract other fireflies. The light intensity  $I$  decreases as the distance  $r$  from the light source increases in terms of inverse square law  $I \propto \frac{1}{r^2}$ . Additionally, the air can absorb the light so as to weaken the light as distance increases. These two factors are combined to make fireflies visible to a certain distance. For two fireflies, the less brighter one will move towards the much brighter one. In a maximization problem, the brightness can be defined proportional to the value of the objective function, the same role as the fitness function in GA.

When applying and understanding the FA, three idealized rules are given in [80], which are as follows:

1. All fireflies will be attracted to other fireflies regardless of their sex;
2. The brightness of a firefly is only determined or affected by the objective function.
3. Attractiveness is proportional to the brightness and decreases as distance increases.

If there is no brighter one than a specific firefly, it will move around randomly.

The pseudo code of the FA is shown in Figure 5-1.

```

Objective function  $f(\mathbf{x})$ ,  $\mathbf{x} = (x_1, x_2, \dots, x_d)^T$ 
Generate initial population of fireflies  $\mathbf{x}_i (i = 1, 2, \dots, n)$ 
Light intensity  $I_i$  at  $\mathbf{x}_i$  is determined by  $f(\mathbf{x}_i)$ 
Define light absorption coefficient  $\gamma$ 
while ( $t < \text{MaxGeneration}$ )
  for  $i = 1:n$  //all  $n$  fireflies
    for  $j = 1:i$  //all  $i$  fireflies
      if ( $I_j > I_i$ )
        Move firefly  $i$  towards  $j$  in  $d$  – dimension;
      end if
      Attractiveness changes accordingly with distance  $r$  via  $\exp[-\gamma r]$ 
      Evaluate new solutions and update light intensity
    end for  $j$ 
  end for  $i$ 
  Rank the fireflies and find the current best
end while
Postprocess results and visualization

```

**Figure 5-1: Pseudo code of FA [80]**

## 5.2.2 Attractiveness Formulation

Two important issues for FA are the variation of light intensity and formulation of the attractiveness. It is always assumed that the attractiveness of a firefly is related directly to its brightness which is closely associated with the objective function. In the case of

maximum optimization, for simplicity the brightness of  $I$  of a firefly at location  $\mathbf{x}$  can be chosen as  $I(\mathbf{x}) \propto f(\mathbf{x})$  which is treated as the original light intensity at  $r=0$ . Besides, light intensity gets reduced with the distance  $r$  from its source and also note that the light is absorbed in the media. Such a compounded effect of both the inverse square law and light absorption can be taken into account in formulating the relationship between light intensity  $I$  and distance  $r$ :

$$I(r) = I_0 e^{-\gamma r^2} \quad (5.1)$$

where  $I_0$  is the original light intensity at  $r=0$  and  $\gamma$  is the absorption coefficient.

Then the attractiveness of a firefly seen by an adjacent firefly is proportional to the light intensity and can be defined by

$$\beta(r) = \beta_0 e^{-\gamma r^2} \quad (5.2)$$

where  $\beta_0$  is the attractiveness at  $r=0$ . In addition, the actual form of attractiveness function  $\beta(r)$  can take forms of any monotonically decreasing functions like

$$\beta(r) = \beta_0 e^{-\gamma r^m} \quad (m \geq 1). \quad (5.3)$$

The attractiveness function plays the role to determine the location of a firefly after movement because of the attraction of another more attractive (or brighter) firefly.

### 5.2.3 Distance and Firefly Movement

The distance between any two fireflies, say,  $\mathbf{x}_i$  and  $\mathbf{x}_j$ , is the Cartesian distance

$$r_{ij} = \|\mathbf{x}_i - \mathbf{x}_j\| = \sqrt{\sum_{k=1}^d (x_{i,k} - x_{j,k})^2} \quad (5.4)$$

where  $x_{i,k}$  is the  $k$ th component of  $\mathbf{x}_i$  of  $i$ th firefly. As a matter of fact, the distance  $r$  is not limited to the Euclidean distance. According to the type of problems of interest, other forms of distance in the  $n$ -dimensional hyperspace can also be defined.

After comparison of light intensity of two fireflies, the movement representing one firefly attracted to another more attractive (or brighter) one takes place. Assuming that firefly  $i$  is attracted to firefly  $j$ , the new location of firefly  $i$  is determined by

$$\mathbf{x}_i^{t+1} = \mathbf{x}_i^t + \beta_0 e^{-\gamma r_{ij}^2} (\mathbf{x}_j^t - \mathbf{x}_i^t) + \alpha_t \boldsymbol{\varepsilon}_i^t. \quad (5.5)$$

There are three terms in the addition where the first term is the current location of the firefly, the second term results from the attraction while the third term accounts for randomization with  $\alpha_t$  as the gradually reduced randomization parameter.  $\boldsymbol{\varepsilon}_i^t$  is a random vector with components in a uniform distribution in  $[0,1]$ .

#### **5.2.4 Rationale for Using FA**

Similar to other metaheuristic algorithms, the FA has the advantages of good convergence properties and robustness. These competitive characteristics are concluded in [79] as follows:

1. They do not require knowledge of gradient information about the optimization problems. They are able to solve any kind of objective functions and any kind of constraints of being linear or non-linear, on discrete or continuous or both spaces.
2. Discontinuities existing in the optimization problems do not affect the overall optimization performance.
3. They can perform global search effectively instead of solving for local optima.
4. They can handle large-scale optimization problems.

5. They are suitable to a wide range of optimization problems.

In addition, based on the comparison of FA with GA and PSO made by Xin-She Yang [80], it is seen that FA is a lot more efficient in finding the global optima with a higher success rate. Various standard test functions are adopted and a population size of 40 is kept in all simulations for comparison purpose. For GA, they used a standard version with mutation probability 0.05 and a crossover probability 0.95. For the PSO, they also used the standard version with the learning parameters being 2. Table 5-1 shows the details about the results. Each algorithm was run at least 100 times in Matlab environment to obtain meaningful statistical analysis and the data in Table 5-1 are in such a format: average number of evaluations  $\pm$  standard deviation (success rate of finding the global optima). This comparison confirms the efficiency and large potential of FA in finding a global optima.

Functions /Algorithms	GA	PSO	FA
Rosenbrock's(d=16)	55723 $\pm$ 8901(90%)	32756 $\pm$ 5325(98%)	7792 $\pm$ 2923(99%)
Michalewicz's(d=16)	89325 $\pm$ 7914(95%)	6922 $\pm$ 537(98%)	3752 $\pm$ 725(99%)
Schwefel's(d=128)	227329 $\pm$ 7572(95%)	14522 $\pm$ 1275(97%)	9902 $\pm$ 592(100%)
De Jong's (d=256)	25412 $\pm$ 1237(100%)	17040 $\pm$ 1123(100%)	7217 $\pm$ 730(100%)
Ackley's(d=128)	32720 $\pm$ 3327(90%)	23407 $\pm$ 4325(92%)	5293 $\pm$ 4920(100%)
Rastrigin's	110523 $\pm$ 5199(77%)	79491 $\pm$ 3715(90%)	15573 $\pm$ 4399(100%)
Easom's	19239 $\pm$ 3307(92%)	17273 $\pm$ 2929(90%)	7925 $\pm$ 1799(100%)
Griewank's	70925 $\pm$ 7652(90%)	55970 $\pm$ 4223(92%)	12592 $\pm$ 3715(100%)
Shubert's	54077 $\pm$ 4997(89%)	23992 $\pm$ 3755(92%)	12577 $\pm$ 2356(100%)
Yang's	27923 $\pm$ 3025(83%)	14116 $\pm$ 2949(90%)	7390 $\pm$ 2189(100%)

**Table 5-1: Comparison of FA with Other Algorithms [80]**

In the present study, there are many parameters to be optimized, involving complex matrix computations and it is hard to show analytical expressions for the targeted performances, say, stiffness and well-conditioned workspace. Actually, the traditional optimization methods only reach a local optima through a step-by-step procedure where they compare values of next points and then move to the relative optimal points with prerequisites strictly satisfied (e.g. gradient, Hessian, linearity, continuity). FA is a type of metaheuristic algorithms and more efficient in searching for a global optima compared with its likes due to the fact that their broadcasting ability of the current best estimates guarantees quicker and more effective convergence towards the optimality. Therefore, it is selected as the best candidate for the optimization studied here.

## **5.3 Stiffness Optimization**

### **5.3.1 Optimization Criteria**

The stiffness can be expressed by stiffness matrix (3.38) or compliance matrix (3.40) and is configuration-dependent and directionally distinguished for a mechanism as analysed in Chapter 3. As the stiffness matrix and compliance matrix describe the same thing—the stiffness of the end-effector from different perspectives, the following shall take the compliance matrix for illustration.

The diagonal entries of the compliance matrix represent the mechanism's pure compliance in each of Cartesian directions for a given configuration. To obtain the highest stiffness in each direction, accordingly the smallest compliance in each direction, the objective function can take the form of equation (5.6) to maximize the negative of

weighted summation of compliance elements; or take the form of equation (5.7) to maximize the weighted summation of stiffness elements.

$$\max -\sum_{i=1}^6 \eta_i c_{ii} \quad (5.6)$$

$$\max \sum_{i=1}^6 \lambda_i \kappa_{ii} \quad (5.7)$$

where

$c_{ii}$  is the diagonal element of the micromanipulator's compliance matrix,

$\kappa_{ii}$  is the diagonal element of the micromanipulator's stiffness matrix,

$\eta_i$  is the weight factor for each directional compliance whose relative value characterizes the priority concern of the compliance in corresponding direction,

$\lambda_i$  is the weight factor for each directional stiffness whose relative value characterizes the priority of the stiffness in corresponding direction.

Note although this is going to maximize the sum of diagonal elements rather than each diagonal element individually, it is still possible to optimize each directional stiffness by strategically assigning different weighting factors  $\eta_i$  or  $\lambda_i$ . In the following, we simply assign  $\eta_i = 1$  ( $i = 1, 2, \dots, 6$ ) and assume the moving platform is in the home position with Pitch-Roll-Yaw being  $\mathbf{R}_{PRY}(0^\circ, 0^\circ, 0^\circ)$ .

### 5.3.2 Variables Selection and Results

Structural parameters represent the geometry of the micromanipulator and they have an influence on the performance of a mechanism while material, geometrical shape and

control system are also factors for that which are beyond current study. So it's possible to improve the stiffness performance by modifying these structural variables with the optimization technique in order to obtain the optimal architecture. Here based on the analysis done previously, three design variables are selected. Referring to Figure 3-6 the vector of optimization variables is

$$\mathbf{s} = [l_1, l_2, r] \quad (5.8)$$

where

$l_1$  is the distance of the CUJ center to the lower end of the CTJ,

$l_2$  is the distance of the CSJ center to the upper end of the CTJ,

$r$  is the distance of the centroid or the reference point of the moving platform to its faces, representing the size of the moving platform.

Their bounds are respectively

$$l_1 \in [4, 6], l_2 \in [5, 8], r \in [5, 9]. \text{ (mm)}$$

In the implementation of FA, the objective function (5.6) is going to be maximized and actually the compliance is minimized. The following parameters are set:

$$\gamma = 1.0, \quad \beta_0 = 1.0, \quad \alpha = 0.5.$$

The number of fireflies is 60 and the maximum number of generations is 40. The FA is implemented in Matlab to search for the optimal solution. Figure 5-2 shows the evolution of global optimums for 40 generations. The design variables searched by the FA after 40 generations are

$$\mathbf{s} = [l_1, l_2, r] = [4, 5, 5] \text{ (mm)} \quad (5.9)$$

and the pure compliance in each direction is

$$\begin{aligned}
& [c_{11}, c_{22}, c_{33}, c_{44}, c_{55}, c_{66}] \\
& = [0.0785, 1.009, 0.0897, 2.59 \times 10^{-4}, 1.71 \times 10^{-4}, 2.14 \times 10^{-4}] \times 10^{-5} \text{ mm} / N
\end{aligned} \tag{5.10}$$

Their sum is  $2.6910 \times 10^{-5}$ . Before the optimization, these variables are originated as

$$\mathbf{s}' = [l_1, l_2, r] = [5.5, 6.5, 7.5] \text{ (mm)} \tag{5.11}$$

and the compliance in each direction is

$$\begin{aligned}
& [c'_{11}, c'_{22}, c'_{33}, c'_{44}, c'_{55}, c'_{66}] \\
& = [0.882, 1.06, 0.973, 2.59 \times 10^{-4}, 1.70 \times 10^{-4}, 2.15 \times 10^{-4}] \times 10^{-5} \text{ mm} / N
\end{aligned} \tag{5.12}$$

Their sum is  $2.9209 \times 10^{-5}$ . It can be easily seen that the stiffness is optimized with the compliance decreased.

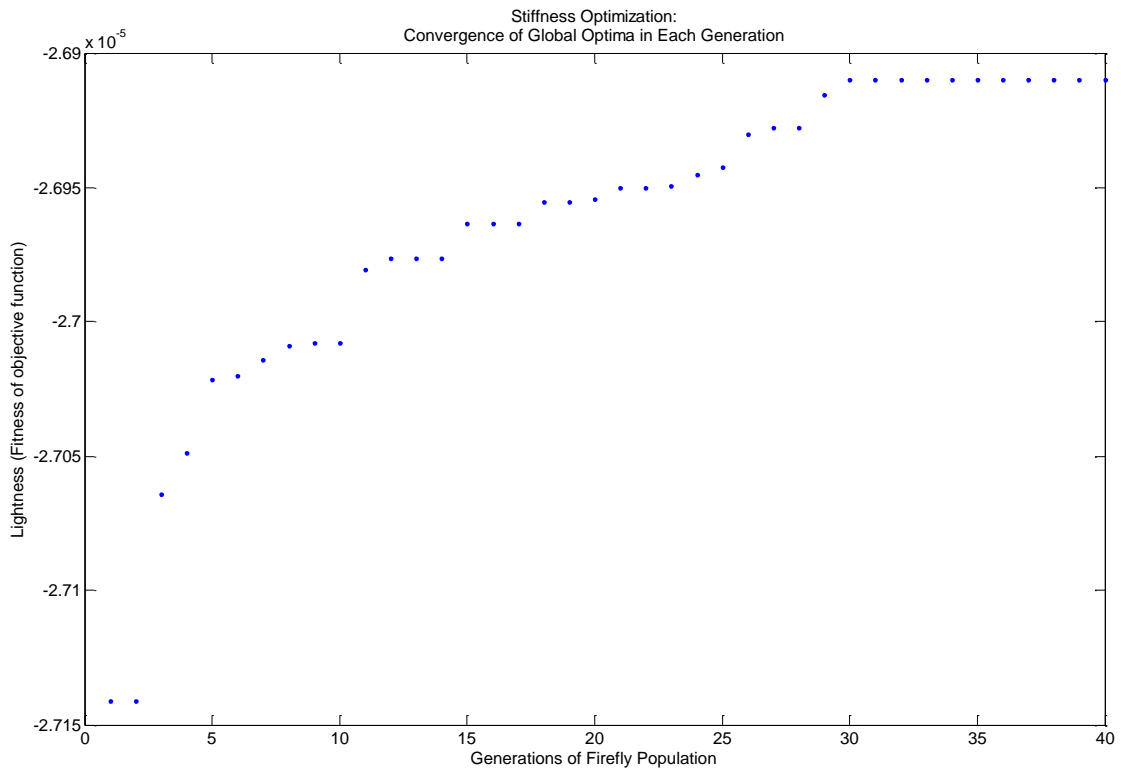


**Figure 5-2: Convergence of global optimums in each generation for stiffness optimization**

## 5.4 Workspace Optimization

### 5.4.1 Optimization Criteria

In terms of parallel manipulators, although they have many advantages over their serial counterparts their workspace is relatively small, which doesn't lead to a shortcoming for micromanipulation. However, a parallel manipulator designed for maximum workspace could not be a practical optimum because the design solely with the consideration of workspace volume always results in poor kinematic characteristics, including bad dexterity and manipulability. Therefore, for the micromanipulator studied here it is necessary to perform an optimization for a workspace with better properties.

The measure of a well-conditioned workspace based on the condition number of manipulator's Jacobian matrix which maps the velocity of the moving platform to the actuated joint rates as analysed in section 2.3.2, will be adopted. A global condition index developed by Gosselin and Angeles [82] considers the dexterity of a manipulator over the entire workspace and can be a good one as the optimization criteria. It is formulated based on the integration of the reciprocal of the condition number of Jacobian matrix over entire workspace. In this study, due to the complexity of obtaining a closed-form solution to the integration, a numerical technique of summation will be used which is going to be presented in detail in the following.

The global condition index  $\eta$  for a well-conditioned workspace is ideally the integration

$$\eta = \int_w \frac{1}{\kappa} dW, \quad (5.13)$$

where  $W$  represents the workspace of a manipulator,  $\kappa$  is the condition number of the Jacobian matrix which takes the 2-norm form of Jacobian matrix

$$\kappa = \|J\| \cdot \|J^{-1}\|. \quad (5.14)$$

Following the above, a Monte Carlo method [83] for approximation of the integration is utilized and outlined as follows:

1. A closed space, often a hemisphere of volume  $V$  is defined which encases entire possible workspace.
2. Randomly generate a large number of points within the hemisphere, namely  $N$  points.
3. Determine  $n$  points that fall within the workspace by testing each point using inverse kinematics.
4. The condition index sum  $S$  is determined by the summation of the reciprocal of the condition number of each point obtained in step 3

$$S = \sum_{i=1}^n \frac{1}{\kappa_i}. \quad (5.15)$$

5. The global condition index  $\eta$  is figured out as

$$\eta = \frac{S}{n} \cdot \frac{n}{N} \cdot V \quad (5.16)$$

The objective function for well-conditioned workspace optimization is formulated according to these five procedures. The objective is to maximize equation (5.16), which is actually minimize all condition numbers  $\kappa_i$  of Jacobian matrix over entire workspace, also providing a means of minimizing the amplification error between the actuators and the end-effector.

## 5.4.2 Variables Selection and Results

In this optimization, design variables and their bounds are set to be the same as shown in (5.8) as in stiffness. For the implementation of FA, the parameters setup is as follows:

$$\gamma = 1.0, \quad \beta_0 = 1.0, \quad \alpha = 0.4 \quad (5.17)$$

The number of fireflies is 60 and generations 30.

Figure 5-3 shows the evolution of global optimums for 30 generations. The design variables searched by the FA after 30 generations are

$$\mathbf{s} = [l_1, l_2, r] = [5.02, 7.51, 5.01] \text{ (mm)} \quad (5.18)$$

while they are originally

$$\mathbf{s}' = [l_1, l_2, r] = [5.5, 6.5, 7.5] \text{ (mm)}. \quad (5.19)$$

For the global condition index  $\eta$ , the value is 0.0139 originally while after optimization 0.0175.

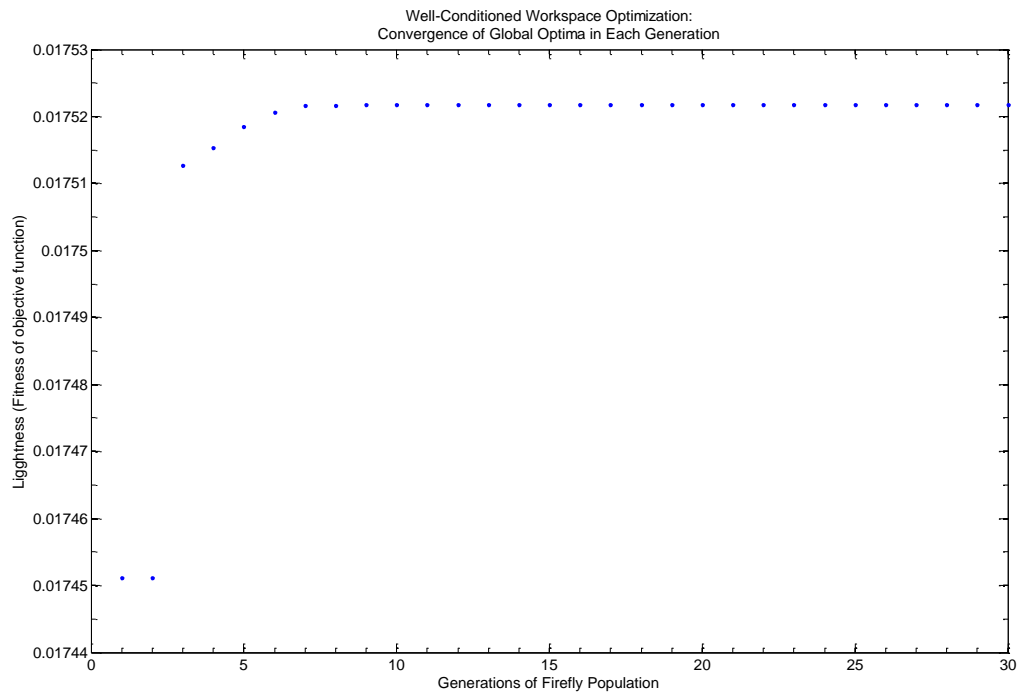


**Figure 5-3: Convergence of global optimums in each generation for well-conditioned workspace optimization**

Additionally, it can be found that the set of optimized design variables in both stiffness optimization and well-conditioned workspace optimization takes different set of values. These two objectives conflict with each other and cannot reach the optimum at the same time. The single-objective optimization only concerns about one objective and the solution usually causes unacceptable results for other considerations. Therefore, it is worthwhile to take the two performance criteria into account to explore multi-objective optimization.

## **5.5 Multi-Objective Optimization**

### **5.5.1 Necessity for Multi-Objective Optimization**

Multi-optimization is a necessary and complicated part of design process. Design problems in engineering always involve many design variables with multiple objectives which often conflict with each other. Optimized set of design variables with respect to a single objective often causes unacceptable results with respect to the other objectives. Therefore, multi-objective problems must be handled properly so that the solutions found satisfy the objectives at an acceptable level. Instead of returning a single global best solution in the case of single-objective optimization, multi-objective optimization methods examine trade-offs of different objectives and provide a set of solutions from which decision-makers can choose with their priorities in considering multiple objectives.

The final goal of multi-objective optimization is to identify a set of solutions named Pareto optimal set which is associated with the corresponding objective function values in objective space called Pareto front. The Pareto optimal set contains all non-dominated

feasible solutions in the variable space. Without loss of generality, for a minimization problem which has an  $n$ -dimensional variable space and  $k$ -dimensional objective space, a solution vector  $\mathbf{x} = (x_1, \dots, x_n)^T$  is said to dominate another one  $\mathbf{y} = (y_1, \dots, y_n)^T$  if and only if

$$\forall i \in \{1, \dots, k\}, f_i(\mathbf{x}) \leq f_i(\mathbf{y}) \text{ and } \exists i \in \{1, \dots, k\}, f_i(\mathbf{x}) < f_i(\mathbf{y}) \quad (5.20)$$

which is denoted by  $\mathbf{x} \prec \mathbf{y}$ . Thus, a solution vector is called a non-dominated solution if no solutions can dominate it.[84]

For current section of study, the stiffness individually optimized in section 5.3 and well-conditioned workspace individually optimized in section 5.4 shall be considered simultaneously as a multi-objective problem. A further developed FA for multi-objective optimization will be adopted to identify the Pareto optimal set.

### 5.5.2 Implementation of Multi-Objective Optimization

Keeping the two performance criteria in mind, namely end-effector stiffness and well-conditioned workspace, the two corresponding objective functions  $f_1$  and  $f_2$  are formulated following equation (5.6) and (5.16), respectively. The design variables are as in expression (5.8) and their bounds are kept same as provided previously. Multi-objective FA developed by extending ideas of basic FA offers a much more efficient search for the Pareto optimal set for the two-objective optimization problem under study. The pseudo code of the multi-objective FA is shown in Figure 5-4.

```

Define objective functions  $f_1(\mathbf{x}), \dots, f_k(\mathbf{x})$  where  $\mathbf{x} = (x_1, x_2, \dots, x_d)^T$ 
Generate initial population of fireflies  $\mathbf{x}_i (i = 1, 2, \dots, n)$ 
while ( $t < \text{MaxGeneration}$ )
  for  $i, j = 1:n$  //all  $n$  fireflies
    if  $\mathbf{x}_j$  dominates  $\mathbf{x}_i$ 
      Move firefly  $i$  towards  $j$  using equation (5.5);
      Generate new ones if the moves don't satisfy all the constraints
    end if
  if no dominated solutions can be found
    Generate random weights  $w_1, \dots, w_k (\sum_{i=1}^k w_i = 1)$ 
    Find the best solution  $\mathbf{g}^t$  (among all fireflies) to  $\min \mathbf{f}(\mathbf{x}) = \sum_{i=1}^k w_i f_i(\mathbf{x})$ 
    Random walk around  $\mathbf{g}^t$  using  $\mathbf{x}_i^{t+1} = \mathbf{g}^t + \alpha_t \boldsymbol{\varepsilon}_i^t$ 
    ( $\alpha_t \boldsymbol{\varepsilon}_i^t$  represent randomness,  $\alpha_t = \alpha_0 0.9^t$  to gradually reduce randomness)
  end if
  Update and pass the non – dominated solutions to next iterations
end
Sort and find the current best approximation to the Pareto front
Update  $t \leftarrow t + 1$ 
end while
Postprocess results and visualization

```

**Figure 5-4: Pseudo code of multi-objective FA [85]**

The algorithm of multi-objective FA is developed in Matlab environment and the major code is seen in Appendix A. Referring to Figure 5-4, the procedure starts with the initialization of a population of  $n$  fireflies. For the diversity of final solutions, the population of fireflies generated initially should distribute in the search space as uniformly as possible and in this study uniform distribution as a sampling technique is used. Then, the iteration begins with the evaluation of objective values of all fireflies and based on the comparison of each pair of fireflies in terms of Pareto optimal set a move of

a firefly can be determined. If a firefly is not dominated by any other fireflies, it would do random walk around the current best  $\mathbf{g}^t$  which minimizes a combined objective function of a weighted sum over all current fireflies. It is worth noting that the weights are generated randomly at each iteration in order that the final non-dominated solutions can distribute diversely along the Pareto front.

The setup of algorithm parameters is as follows.

$$\beta_0 = 1.0, \alpha_0 = 0.25, \gamma = 1.0 \quad (5.21)$$

The number of fireflies in a population is 80 and the maximum generation is 20. In the following section, the results from the algorithm shall be presented and discussed.

### 5.5.3 Results

The weighted sum of the two objectives is treated as a maximum optimization and hence the objective function of compliance takes negative values simply by placing a '-' ahead of the function expression. Since the magnitude values of the two objective functions are largely different, normalization is necessary.

Figure 5-5 shows an initial population of fireflies distributed in the objective space and the Pareto front associated with identified Pareto optimal set of fireflies by the algorithm. It can be seen that the multi-objective FA effectively reaches a good approximation of Pareto front with respect to a large group of fireflies. In Figure 5-6, a plot for Pareto front is presented which represents the best trade-offs. The table of design variables corresponding to each point in Pareto front is provided in Appendix B.

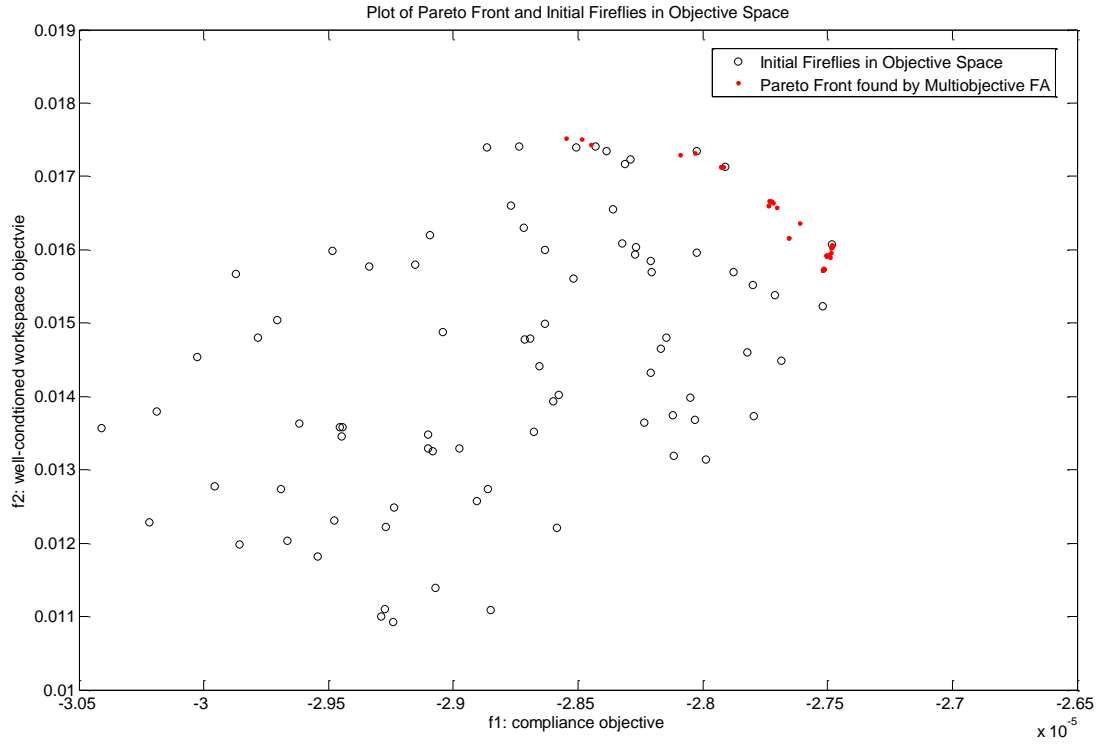


**Figure 5-5: Plot of Pareto front and initial fireflies in objective space**

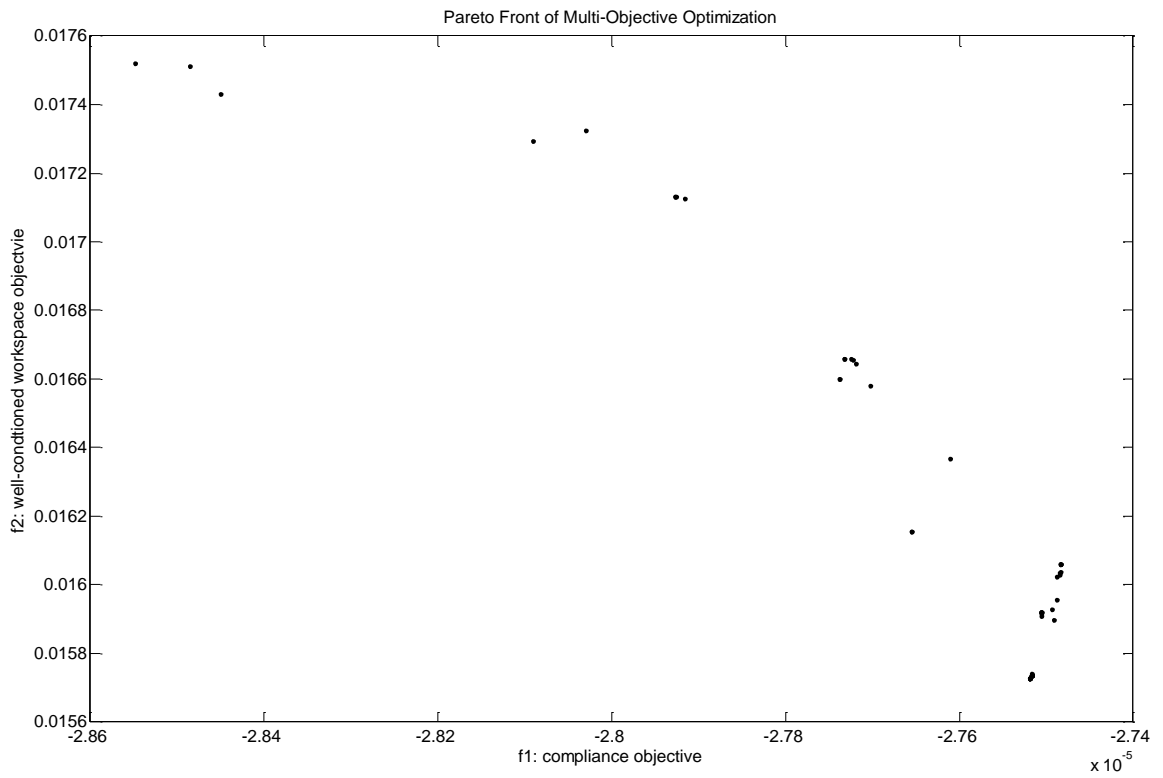


**Figure 5-6: Pareto front of multi-objective optimization**

## **5.6 Conclusions**

Previous analysis of stiffness and workspace has been an essential part of this chapter and by exploring the performance optimization the design variables have been further optimized and determined. It can be seen that different values of design variables have distinct influence on multiple performance criteria. Through optimization, the stiffness and working properties of the micromanipulator are improved. Also, for different tasks with different requirements on each of performance criteria multi-objective optimization offers the best trade-offs to choose from. The process of how to use the optimization technique FA is presented and it turns out to be a powerful tool for addressing this kind of problems.

# Chapter 6

## Conclusions and Further Study

### 6.1 Conclusions

A novel macro-micromanipulator is proposed in the thesis which is used for performing micromanipulation in manufacturing and biomedical fields. There are two different parallel mechanisms in the system where the micromanipulator characterized by a parallel compliant 3-UPS mechanism is designed to perform high accuracy motions while the planar 3-RRR parallel mechanism is able to achieve large range transfer from one working site to another. The micromanipulator has been given intense focus in the study. In this last chapter, all important work that the current study covers is going to be reviewed and some remarks for further study are provided.

1. Based on the geometrical description of the manipulators proposed, kinematic analysis is implemented for both macromanipulator and micromanipulator. From kinematic analysis, the mobility, inverse kinematic solution and Jacobian matrix

are derived. Such information helps to define the mechanism more fully and also paves the way for further analysis like workspace evaluation.

2. Performance analysis and evaluation is a necessary part after the design is defined.

For the micromanipulator under study, the accuracy and reliability of the motion transfer from actuators to the end-effector are highly of attention and two performance analyses are conducted. Stiffness criterion describing the amount of deflections of end-effector is quantified by stiffness/compliance matrix. It establishes a relationship among the stiffness and the design variables, and compliance mapping visibly shows the relationship for design variables with values in a certain range. Workspace shape and volume of the micromanipulator is analyzed by using inverse kinematics. The method used is based on point search. Approximation of the actual workspace is visualized by mathematical plots in Matlab environment.

3. Optimization serves to modify the structural design variables with the aim of augmenting performances. FA is selected, which turns out to be a more efficient and powerful tool. Two single-objective optimization processes for higher stiffness and well-conditioned workspace are performed, respectively. It can be seen from the single-objective optimization results that these two objectives conflict with each other, which is very common in dealing with engineering design problems. More practically, multi-objective optimization resulting in a set of solutions of different trade-offs, i.e. Pareto optimal set, provides decision-makers with solutions at different acceptable levels for each objective.

## 6.2 Further Study

The study presented in this thesis is primarily about kinematic structure design, analysis and optimization for the manipulator proposed. No subjects involving its dynamic behaviour, simulation and control issues are taken into consideration. In order to make the macro-micromanipulator system commercially available, the future study is suggested here.

1. Dynamic analysis and simulation. This deals with the forces and torques needed to generate motions of a system of bodies, i.e. the macromanipulator and the micromanipulator. The final results can be evaluated by simulation and further evaluated by experimentation in preparation for a real-time, model-based control.
2. Control system and control strategy development. If PZT actuators are adopted, the algorithm of alleviating the effect of hysteresis need to be developed in order to improve the end-effector accuracy and reduce response time. The robustness and stability of the control system must also be considered.
3. Fabrication of components of the micromanipulator. There are some compliant joints which play a crucial part in achieving micro and accurate motion transfer. The fabrication requirements of these components are different from others and particularly, smaller error tolerance in dimensions is required. Therefore, advanced fabrication technology can be explored and the modularity design is suggested.

# References

- [1] M. Sitti, "Survey of nanomanipulation systems," in *Proc. of the 2001 1st IEEE Conf. on Nanotechnology*, Maui, HI, 2001, pp. 75-80.
- [2] Microtechnology. Available: <http://en.wikibooks.org/wiki/Microfabrication>
- [3] H. Li, "Microfabrication techniques for producing freestanding multi-dimensional microstructures," *Microsystem Tehcnologies*, vol. 22, iss. 2, pp. 223-237, 2016.
- [4] MEMS and Nanotechnology Exchange®, What is MEMS?. Available: [http://www.memsnet.org/mems/what\\_is.html](http://www.memsnet.org/mems/what_is.html)
- [5] A. E. Alejandro, *et al.*, "A REVIEW ON DESIGN METHODS FOR COMPLIANT MECHANISMS," *Mecánica Computacional*, vol. XXIX, pp. 59-72, 2010.
- [6] T. Akima, S. Tarao, M. Uchiyama, "Hybrid micro-gravity simulator consisting of a high-speed parallel robot," in *Proc. of IEEE Int. Conf. on Robotics and Automation*, Michigan, 1999, pp. 901-906.
- [7] Ares Jon, Brazales Alfonso, Busturia Jesus M., "Tuning and validation of the motion platform washout filter parameters for a driving simulator," in *Driving Simulation Conf.*, Sophia-Antipolis, France, 2001, pp. 295-304.
- [8] I. Hostens, J. Anthonis, H. Ramon, "New design for a 6 dof vibration simulator with improved reliability and performance," *Mech. Syst. Signal Process*, vol. 19, pp. 105-122, 2005.
- [9] J. Y. Huang, C. Y. Gau, "A pc cluster high-fidelity mobile crane simulator," *Tamkang J. Sci. Eng.*, vol. 5, pp. 7-20, 2002.
- [10] C. C. Nguyen, *et al.*, "Adaptive control of a Stewart platform-based manipulator," *J. Robot Syst.*, vol. 10, pp. 657-687, 1993.
- [11] G. S. Chirikjian, "Hyper-redundant manipulator dynamics: a continuum approximation," *Adv. Robotics*, vol. 9, pp. 217-243, 1995.
- [12] M. Hafez, M. D. Lichter, S. Dubowsky, "Optimized binary modular reconfigurable robotic devices," *IEEE Trans. Mechatron.*, vol. 8, pp. 152-162, 2003.
- [13] V. A. Sujana, S. Dubowsky, "Design of lightweight hyper-redundant deployable binary manipulator," *ASME J. Mech. Des.*, vol. 126, pp. 29-39, 2004.
- [14] Li-Ju Xu, Shou-Wen Fan, H. Li, "Analytical model method for dynamics of n-celled tetrahedron variable geometry truss manipulators," *Mech. Mach. Theory*, vol. 36, pp. 1271-1279, 2001.

- [15] M. L. Culpepper, G. Anderson, "Design of a low-cost nano-manipulator which utilizes a monolithic, spatial compliant mechanism," *J. Precision Eng.*, vol. 28, pp. 469-482, 2004.
- [16] M. L. Culpepper, M. V. Kartik, C. DiBiasio, "Design of integrated mechanisms and exact constraint fixtures for micron-level repeatability and accuracy," *J. Precision Eng.*, vol. 29, pp. 65-80, 2005.
- [17] K. A. Jensen, C. P. Lusk, L. L. Howell, "An xyz micromanipulator with three translational degrees of freedom," *Robotica*, vol. 24, pp. 305-314, 2006.
- [18] Q. Xu, Y. Li, "A novel design of a 3-prc compliant parallel micromanipulator for nanomanipulation," *Robotica.*, vol. 24, pp. 521-528, 2006.
- [19] B. Yi, *et al.*, "Design and experiment of a 3-dof parallel micromechanism utilizing flexure hinges," *IEEE Robot. Automat. Mag.*, vol. 19, pp. 604-612, 2003.
- [20] G. Carbone, M. Ceccarelli, "A serial-parallel robotic architecture for surgical tasks," *Robotica*, vol. 23, pp. 345-354, 2005.
- [21] T. Li, S. Payandeh, "Design of spherical parallel mechanisms for application to laparoscopic surgery," *Robotica*, vol. 20, pp. 133-138, 2002.
- [22] G. Rosati, P. Gallina, S. Masiero, "Design, implementation and clinical test of a wirebased robot for neuro rehabilitation," *IEEE Trans. Neural Syst. Rehabil. Eng.*, vol. 15, pp. 560-569, 2007.
- [23] M. Shoham, *et al.*, "Bone-mounted miniature robot for surgical procedures: concept and clinical applications," *IEEE Trans. Robot. Autom.*, vol. 19, pp. 893-901, 2003.
- [24] A. Romiti, M. Sorli, "Force and moment measurement on a robotic assembly hand," *Sensors and Actuators A*, vol. 32, pp. 531-538, 1992.
- [25] M. Sorli, S. Pastorelli, "Six-axis reticulated structure force/torque sensor with adaptable performances," *Mechatronics*, vol. 5, pp. 585-601, 1995.
- [26] C. Ferraresi, S. Pastorelli, N. Zhmud, "Static and dynamic behavior of a high stiffness Stewart platform-based force/torque sensor," *J. Robot. Syst.*, vol. 12, pp. 883-893, 1995.
- [27] R. Ranganath, *et al.*, "A force-torque sensor based on a Stewart platform in a near-singular configuration," *Mech. Mach. Theory*, vol. 39, pp. 971-998, 2004.
- [28] P. Bailey, "The merits of hexapods for robotics applications," in *Conf. on Next Steps for Industrial Robotics*, London, U.K., 1994, pp. 11-16.
- [29] J. Lauffer, *et al.*, "Milling machine for the 21st century-goals, approach, characterization and modeling," in *Proc. of SPIE - the Int. Society for Optical Eng. Smart Structures and Materials*, 1996, pp. 326-340.

- [30] S. M. Wang, K. F. Ehmann, "Error model and accuracy analysis of a six-dof Stewart platform," *ASME J. Manuf. Sci. Eng.*, vol. 124, pp. 286–295, 2002.
- [31] X. Yu, *et al.*, "Measuring data based non-linear error modeling for parallel machine-tool," in *IEEE Int. Conf. on Robot. and Automat.*, Seoul, South Korea, 2001, pp. 3535–3540.
- [32] M. Honegger, A. Codourey, E. Burdet, "Adaptive control of the hexaglide, a 6 dof parallel manipulator," in *Proc. of the IEEE Int. Conf. on Robot. and Automat.*, Albuquerque, USA, 1997, pp. 543-548.
- [33] G. Pritschow, K. H. Wurst, "Systematic design of hexapods and other parallel link systems," *CIRP Ann. – Manufacturing Technology*, vol. 46, pp. 291–295, 1997.
- [34] L. H. Larry, "Introduction," in *Compliant Mechanisms*, New York: John Wiley & Sons, Inc., 2001, ch. 1, pp. 1-18.
- [35] L. H. Larry, A. Midha, "A method for the design of compliant mechanisms with small-length flexural pivots," *ASME J. of Mech. Design*, vol. 118, pp. 121-125, 1996.
- [36] B. P. Trease, Yong-Mo Moon, S. Kota, "Design of Large-Displacement Compliant Joints," *Trans. of ASME*, vol. 127, pp. 788-798, 2005.
- [37] D. F. Machekposhti, N. Tolou, J. L. Herder, "A Review on Compliant Joints and Rigid-Body Constant Velocity Universal Joints Toward the Design of Compliant Homokinetic Couplings," *J. of Mech. Des.*, vol.137, iss. 3.
- [38] D. Zhang, "Architectures of Parallel Robotic Machines," in *Parallel Robotic Machine Tools*, New York: Springer, 2010, ch. 3, pp. 33-50.
- [39] G. Chen, Y. Gou, A. Zhang, "Synthesis of Compliant Multistable Mechanisms Through Use of a Single Bistable Mechanism," *J. of Mech. Design*, vol. 133, 2011.
- [40] F. E. Scire, E. C. Teague, "Piezodriven 50  $\mu\text{m}$  range stage with subnanometer resolution," *Rev. Sci. Instrum.*, vol. 49, pp. 1735–1740, 1978.
- [41] T. Tanikawa, T. Arai, P. Ojala, M. Saeki, "Two-finger micro-hand," in *Proc. of IEEE Int. Conf. Robot. and Automat.*, 1995, pp.1674–1679.
- [42] T. Arai, J. Herve, T. Tanikawa, "Development of 3-DOF micro-finger," in *Proc. of the 1996 IEEE/RSJ Int. Conf.*, 1996, vol. 2, pp. 981–987.
- [43] J. W. Ryu, D.-G. Gweon, K. S. Moon, "Optimal design of a flexure hinge based XY $\phi$  wafer stage," *Precis. Eng.*, vol. 21, pp. 18–28, 1997.
- [44] M. L. Culpepper, G. Anderson, "Design of a low-cost nano-manipulator which utilizes a monolithic, spatial compliant mechanism," *Precis. Eng.*, vol. 28, pp. 469–482, 2004.
- [45] Y. Li, Q. Xu, "Modeling and performance evaluation of a flexure-based XY parallel micromanipulator," *Mech. Mach. Theory*, vol. 44, pp. 2127–2152, 2009.

- [46] Y. K. Yong, T. F. Lu, "The effect of the accuracies of flexure hinge equations on the output compliances of planar micro-motion stages," *Mech. Mach. Theory*, vol. 43, pp. 347–363, 2008.
- [47] Y. K. Yong, T.-F. Lu, "Kinetostatic modeling of 3-RRR compliant micro-motion stages with flexure hinges," *Mech. Mach. Theory*, vol. 44, pp. 1156–1175, 2009.
- [48] Y. Tian, B. Shirinzadeh, D. Zhang, "A flexure-based five-bar mechanism for micro/nano manipulation," *Sens. Actuators A: Phys.*, vol. 153, pp. 96–104, 2009.
- [49] Y. Tian, B. Shirinzadeh, D. Zhang, X. Liu, D. Chetwynd, "Design and forward kinematics of the compliant micro-manipulator with lever mechanisms," *Precis. Eng.*, vol. 33, pp. 466–475, 2009.
- [50] Y. Yue, F. Gao, X. Zhao, Q. Ge, "Relationship among input-force, payload, stiffness and displacement of a 3-DOF perpendicular parallel micro-manipulator," *Mech. Mach. Theory*, vol. 45, pp. 756–771, 2010.
- [51] Y. Yue, F. Gao, X. Zhao, Q. Ge, "Relationship among input-force, payload, stiffness, and displacement of a 6-DOF perpendicular parallel micro-manipulator," *J. Mech. Robot.*, vol. 2, 2011.
- [52] Y. Dong, F. Gao, Y. Yue, "Modeling and experimental study of a novel 3-RPR parallel micro-manipulator," *Robotics and Computer-Integrated Manufacturing*, vol. 37, pp. 115-124, 2016.
- [53] G. W. Ellis, "Piezoelectric micromanipulators," *Science*, vol. 138, pp. 84, 1962.
- [54] A. Sharon, D. Hardt, "Enhancement of Robot Accuracy using Endpoint Feedback and a Macro-Micro Manipulator System," in *American Control Conf.*, San Diego, CA, USA, 1984, pp. 1836-1845.
- [55] A. Sharon, "THE MACRO/MICRO MANIPULATOR: AN IMPROVED ARCHITECTURE FOR ROBOT CONTROL," Ph.D. dissertation, Dept. Mech. Eng., MIT, MA, USA, 1988.
- [56] W. Dong, L. N. Sun, Z. J. Du, "Design of a precision compliant parallel positioner driven by dual piezoelectric actuators," *Sensors and Actuators A: Physical*, vol. 135, pp. 250-256, 2007.
- [57] Eric Ho, R. B. Gorbet, "A low cost macro-micro positioning system with SMA-actuated micro stage," *Trans. of the CSME*, vol. 31, no. 1, pp. 75-95, 2007.
- [58] J. Zhang, *et al.*, "Macro-micro driven ultra-precision positioning stage for conventional grinder," in *Intell. Robot. and Applicat.*, Heidelberg, Germany: Springer, 2008, pp. 848-857.
- [59] B. Yu, *et al.*, "Research on macro-micro dual-drive micro-location platform based on micro-vision," *Trans. of the Chinese Soc. for Agricultural Machinery*, vol. 39, pp. 125-129, 2008.

- [60] P. R. Ouyang, "A spatial hybrid motion compliant mechanism: Design and optimization," *Mechatronics* (2011), doi:10.1016/j.mechatronics.2010.12.009.
- [61] J. Feng, *et al.*, "A new macro-micro dual drive parallel robot for chromosome dissection," *J. of Mech. Sci. and Tech.*, vol. 26, pp. 187-194, 2012.
- [62] Y. Qin, *et al.*, "Design and kinematics modeling of a novel 3-DOF monolithic manipulator featuring improved Scott–Russell mechanisms," *J. Mech. Des.*, vol. 135, 2013.
- [63] L. H. Larry, "PSEUDO-RIGID-BODY MODEL," in *Compliant Mechanisms*, New York: John Wiley & Sons, INC., 2001, ch. 5, pp. 135-205.
- [64] Lung-Wen Tsai, "Position Analysis of Parallel Manipulators," in *Robot analysis: the mechanics of serial and parallel manipulators*, New York: Wiley, 1999, ch. 3, pp. 116-161.
- [65] H. D. Taghirad, "Jacobians: Velocities and Static Forces," in *Parallel robots: mechanics and control*, Boca Raton: CRC Press, 2013, ch. 2, pp. 118-119.
- [66] Lung-Wen Tsai, "Jacobian Analysis of Parallel Manipulators," in *Robot analysis: the mechanics of serial and parallel manipulators*, New York: Wiley, 1999, ch. 5, pp. 224-225.
- [67] Q. Xu, Y. Li, "Stiffness Modeling for an Orthogonal 3-PUU Compliant Parallel Micromanipulator," in *Proc. of the 2006 IEEE Int. Conf. on Mechatronics and Auto.*, China: Luoyang, 2006, pp. 124-129.
- [68] K. Yoshihiko, *et al.*, "Kinematic Analysis of Translational 3-DOF Micro Parallel Mechanism Using Matrix Method," in *Proc. of the 2000 IEEE/RSJ Int. Conf. on Intell. Robots and Systems*, 2000, pp. 786-792.
- [69] L. Sciavicco, B. Siciliano, "Differential Kinematics and Statics," in *Modeling and Control of Robot Manipulators*, New York: The McGraw-Hill Companies, Inc., 1996.
- [70] H. Bruyninckx, S. Demey, V. Kumar, "Generalized stability of compliantgrasps," in *Proc. of IEEE Int. Conf. on Robotics and Automation*, 1998, pp. 2396–2402.
- [71] C. M. Gosselin, "Stiffness mapping for parallel manipulators," *IEEE Trans. Robot. Autom.*, vol. 6, no. 3, pp. 377-382, 1990.
- [72] Q. Xu, Y. Li, "Kinematic Analysis of a New 3-DOF Translational Parallel Manipulator," in *Proc. of ASME 2005 Int. Design Engineering Technical Conf. and Computers and Information in Engineering Conf.*, Long Beach, California, 2005, pp. 24-28.
- [73] Q. Xu, Y. Li, "Kinematic Design of a Novel 3-DOF Compliant Parallel Manipulator for Nanomanipulation," in *Proc. of IEEE/ASME Int. Conf. on Advanced Intelligent Mechatronics*, 2005, pp. 93-98.

- [74] Q. Xu, Y. Li, “Kinematic Analysis and Design of a New 3-DOF Translational Parallel Manipulator,” *ASME J. Mech. Des.*, vol. 128, pp. 729-737, 2006.
- [75] J. P. Conti, *et al.*, “WORKSPACE VARIATION OF A HEXPOD MACHING TOOL,” NIST Interagency/Internal Report (NISTIR) – 6135, U.S., March 1998.
- [76] R. C. Hibbeler, “Bending,” in *Mechanics of Materials*, 9<sup>th</sup> ed. Upper Saddle River, NJ: Prentice –Hall, 2014, ch. 6, pp. 289-291.
- [77] J. M. Paros, L. Weisbord, “How to design flexure hinges,” *Machine Design*, vol. 37, pp. 151-156, 1965.
- [78] H. D. Taghirad, “Motion Representation,” in *Parallel robots: mechanics and control*, Boca Raton: CRC Press, 2013, ch. 2, pp. 35-37.
- [79] D. Zhang, “KINETOSTATIC ANALYSIS AND OPTIMIZATION OF PARALLEL AND HYBRID ARCHITECTURES FOR MACHINE TOOLS,” Ph.D. dissertation, Mech. Eng. Dept., Laval Univ., Quebec, BC, 2000.
- [80] X.-S. Yang, “Firefly algorithms for multimodal optimization,” in *Stochastic Algorithms: Foundations and Applications*, SAGA 2009, Lecture Notes in Computer Science, vol. 5792, pp. 169-178, 2009.
- [81] J. Kennedy, R. Eberhart, “Particle swarm optimization,” in *Proc. of IEEE Int. Conf. on Neural Networks*, Piscataway, NJ, 1995, pp. 1942-1948.
- [82] C. M. Gosselin, J. Angeles, “A global performance index for the kinematic optimization of robotic manipulators,” *ASME J. of Mech. Design*, vol. 113, pp. 220-226, 1991.
- [83] R. E. Stamper, Lung-Wen Tsai, G. C. Walsh, “Optimization of a Three DOF Translational Platform for Well-Conditioned Workspace,” in *Proc. of IEEE Int. Conf. on Robot. and Autom.*, Albuquerque, New Mexico, 1997.
- [84] C. A. Coello, “An updated survey of evolutionary multi-objective optimization techniques: state of the art and future trends,” in *Proc. of 1999 Congress on Evolutionary Computation*, 1999 © CEC99. doi: 10.1109
- [85] X.-S. Yang, “Multiobjective firefly algorithm for continuous optimization,” *Engineering with Computers*, vol. 29, iss. 2, pp. 175-184, 2013.

# Appendix

## A Matlab Code

### 1. Compliance calculation

```
%%Compliance calculation
clear all;close all;

%%Define structural parameters and compliant joint parameters
%Ti-6Al-4V alloy parameters
E=1.138e11;%Young's modulus
p=0.342;%Poisson's ratio
G=E/(2*(1+p));%shear modulus

%structural parameters of 3-UPS CPM
l1=5.5;
l2=6.5;
l3=13.5;
d0=67;

%parameters of compliant universal joint & spherical joint
t=0.5;
r=1.0;
w=10;

%parameters of compliant prismatic joint
h=1;
d=5;
l=11.5;
k2=0.312;

%%Calculate compliance matrix of basic compliant elements
%Define compliancexi C_hinge of right circular hinge
C_hinge=zeros(6);

% ch1 to ch8 are elements of C_hinge
ch1 = 9*pi*sqrt(r^5)/(2*E*w*sqrt(t^5)) +
3*pi*sqrt(r^3)/(2*E*w*sqrt(t^3));
ch2 = 12*pi*r^2/(E*w^3)*(sqrt(r/t) - 1/4);
ch3 = 9*pi*sqrt(r^3)/(2*E*w*sqrt(t^5));
```

```

ch4 = 12*r/(E*w^3)*(pi*sqrt(r/t) - (2+pi)/2);
ch5 = 1/(E*w)*(pi*sqrt(r/t) - pi/2);
ch6 = 12/(E*w^3)*(pi*sqrt(r/t) - (2+pi)/2);
ch7 = 9*pi*sqrt(r)/(2*E*w*sqrt(t^5));
ch8 = 9*pi*sqrt(r)/(4*G*w*sqrt(t^5));

% C_hinge with elements ch1 to ch8
C_hinge(1,1) = ch1;
C_hinge(2,2) = ch2;
C_hinge(3,3) = ch5;
C_hinge(4,4) = ch6;
C_hinge(5,5) = ch7;
C_hinge(6,6) = ch8;
C_hinge(1,5) = ch3;
C_hinge(5,1) = ch3;
C_hinge(2,4) = -ch4;
C_hinge(4,2) = -ch4;

%Define compliance matrix C_beam of cantilever
C_beam=zeros(6);

% ch1 to ch8 are elements of C_hinge
cb1 = 4*l^5/(E*w*h^3);
cb2 = 4*l^5/(E*h*w^3);
cb3 = 6*l^2/(E*w*h^3);
cb4 = 6*l^2/(E*h*w^3);
cb5 = 1/(E*h*w);
cb6 = 12*l/(E*w^3*h);
cb7 = 12*l/(E*h^3*w);
cb8 = 1/(G*k2*h^3*w);

% C_beam with elements cb1 to cb8
C_beam(1,1) = cb1;
C_beam(2,2) = cb2;
C_beam(3,3) = cb5;
C_beam(4,4) = cb6;
C_beam(5,5) = cb7;
C_beam(6,6) = cb8;
C_beam(1,5) = cb3;
C_beam(5,1) = cb3;
C_beam(2,4) = -cb4;
C_beam(4,2) = -cb4;

%%Compliance matrices of compliant joints adopted in the design
%For compliant universal joint
C1=C_hinge;
C2=C1;
%For compliant translational joint
r41=[0,0,d]';
r42=r41;

J41=[RotZ(-pi/2)*RotX(-pi/2),-RotZ(-pi/2)*RotX(-pi/2)*Skew(r41)];

```

```

        zeros(3), RotZ(-pi/2)*RotX(-pi/2)];
J42=[RotZ(pi/2)*RotX(-pi/2), -RotZ(pi/2)*RotX(-pi/2)*Skew(r42);
      zeros(3), RotZ(pi/2)*RotX(-pi/2)];

C41=J41*C_beam*J41';
C42=J42*C_beam*J42';
C4=C41+C42;
C3=C4;

%For compliant spherical joint
J51=[RotZ(-pi/2), zeros(3);
      zeros(3), RotZ(-pi/2)];
J52=eye(6);
J53=[RotX(pi/2)*RotY(pi/2), zeros(3);
      zeros(3), RotX(pi/2)*RotY(pi/2)];

C5=J51*C_hinge*J51'+J52*C_hinge*J52'+J53*C_hinge*J53';

%%Compliance matrix of one leg
%For leg 1
r1=[0,0,d0+l3]';
r2=r1;
r3=[0,0,d0-l1+l3]';
r4=[0,0,l2+l3]';
r5=[0,0,l3]';

J1=[eye(3), -Skew(r1);
     zeros(3), eye(3)];
J2=[RotZ(pi/2), -RotZ(pi/2)*Skew(r2);
     zeros(3), RotZ(pi/2)];
J3=[eye(3), -Skew(r3);
     zeros(3), eye(3)];
J4=[eye(3), -Skew(r4);
     zeros(3), eye(3)];
J5=[eye(3), -Skew(r5);
     zeros(3), eye(3)];

Jl1=[J1, J2, J3, J4, J5];

Cc=zeros(30);
Cc(1:6,1:6)=C1;
Cc(7:12,7:12)=C2;
Cc(13:18,13:18)=C3;
Cc(19:24,19:24)=C4;
Cc(25:30,25:30)=C5;

Cl1=Jl1*Cc*Jl1';

%For leg 2
J_1=[RotX(-pi/2), -RotX(-pi/2)*Skew(r1);
      zeros(3), RotX(-pi/2)];
J_2=[RotX(-pi/2)*RotZ(pi/2), -RotX(-pi/2)*RotZ(pi/2)*Skew(r2);

```

```

        zeros(3),RotX(-pi/2)*RotZ(pi/2)];
J_3=[RotX(-pi/2),-RotX(-pi/2)*Skew(r3);
      zeros(3),RotX(-pi/2)];
J_4=[RotX(-pi/2),-RotX(-pi/2)*Skew(r4);
      zeros(3),RotX(-pi/2)];
J_5=[RotX(-pi/2),-RotX(-pi/2)*Skew(r5);
      zeros(3),RotX(-pi/2)];
Jl2=[J_1,J_2,J_3,J_4,J_5];

Cl2=Jl2*Cc*Jl2';

%For leg 3
J__1=[RotY(pi/2),-RotY(pi/2)*Skew(r1);
       zeros(3),RotY(pi/2)];
J__2=[RotY(pi/2)*RotZ(pi/2),-RotY(pi/2)*RotZ(pi/2)*Skew(r2);
       zeros(3),RotY(pi/2)*RotZ(pi/2)];
J__3=[RotY(pi/2),-RotY(pi/2)*Skew(r3);
       zeros(3),RotY(pi/2)];
J__4=[RotY(pi/2),-RotY(pi/2)*Skew(r4);
       zeros(3),RotY(pi/2)];
J__5=[RotY(pi/2),-RotY(pi/2)*Skew(r5);
       zeros(3),RotY(pi/2)];
Jl3=[J__1,J__2,J__3,J__4,J__5];

Cl3=Jl3*Cc*Jl3';

%%Compliance of the overall compliant 3-UPS mechanism
C=C11+C12+C13;

```

## 2. Workspace evaluation

### TestPose function:

```

function results=TestPose(x,y,z,alpha,beta,gama)

%Geometrical parameters
R=89.5;
r=7.5;

%Elements of rotation matrix obtained from Pitch-Roll-Yaw
representation
R11=cos(beta)*cos(gama);
R21=cos(beta)*sin(gama);
R31=-sin(beta);
R12=sin(alpha)*sin(beta)*cos(gama)-cos(alpha)*sin(gama);
R22=sin(alpha)*sin(beta)*sin(gama)+cos(alpha)*cos(gama);
R32=sin(alpha)*cos(beta);
R13=cos(alpha)*sin(beta)*cos(gama)+sin(alpha)*sin(gama);
R23=cos(alpha)*sin(beta)*sin(gama)-sin(alpha)*cos(gama);
R33=cos(alpha)*cos(beta);

```

```

%Inverse kinematic calculation
d10=x^2+y^2+z^2+r^2*(R13^2+R23^2+R33^2)-
2*r*(x*R13+y*R23+z*R33)+2*R^2-...
    2*R*(x-R13*r)-2*R*(y-R23*r);
d20=x^2+y^2+z^2+r^2*(R12^2+R22^2+R32^2)-
2*r*(x*R12+y*R22+z*R32)+2*R^2-...
    2*R*(x-R12*r)-2*R*(z-R32*r);
d30=x^2+y^2+z^2+r^2*(R11^2+R21^2+R31^2)-
2*r*(x*R11+y*R21+z*R31)+2*R^2-...
    2*R*(y-R21*r)-2*R*(z-R31*r);

d1=sqrt(d10);
d2=sqrt(d20);
d3=sqrt(d30);

%Constraints:d[81.86,82.14]
if
(81.86<=d1)&&(d1<=82.14)&&(81.86<=d2)&&(d2<=82.14)&&(82.2023<=d3)
&&(d3<=82.4823)
    results=1;
else results=0;
end

```

### Workspace boundary function:

```

function G=WBoundary(i,j)

C=[89.5,89.5,89.5]';
e0=0.001;%e0 is the deviation tolerance from the workspace
boundary.
tho=0.4;%tho is the scalar representing the length of the search
vector.
tho0=tho/2;

while tho0>(e0/2)
    v1=tho*sin(j)*sin(i);
    v2=tho*sin(j)*cos(i);
    v3=tho*cos(j);
    v=[v1 v2 v3]'+C;
    if TestPose(v(1),v(2),v(3),0,0,pi/36)
        tho=tho+tho0;
    else tho=tho-tho0;
    end
    tho0=tho0/2;
end

v1=tho*sin(j)*sin(i);
v2=tho*sin(j)*cos(i);

```

```

v3=tho*cos(j);
v=[v1 v2 v3]'+C;
if TestPose(v(1),v(2),v(3),0,0,pi/36)==0
    tho=tho-tho0;
    v1=tho*sin(j)*sin(i);
    v2=tho*sin(j)*cos(i);
    v3=tho*cos(j);
end

G=[v1 v2 v3]'+C;

```

### Workspace search algorithm:

```

clear all;close all;

G=zeros(3,65160);
n=0;
%Spherical search algorithm for workspace points
for i=pi/180:pi/180:2*pi
    for j=0:pi/180:pi
        n=n+1;
        G(:,n)=WBoundary(i,j);
    end
end
end
xmax=max(G(1,:));
xmin=min(G(1,:));
yax=max(G(2,:));
yin=min(G(2,:));
zax=max(G(3,:));
zin=min(G(3,:));
v=(xmax-xmin)*(yax-yin)*(zax-zin)

```

### 3. Single-objective optimization

#### Stiffness optimization main program:

```

function [best]=firefly1(instr)

if nargin<1, instr=[60,40]; end
n=instr(1);%n is the number of fireflies.
MaxGeneration=instr(2);
rand('state',0);

range=[4,6,5,8,5,9];%range=[l1min l1max l2min l2max rmin rmax]

gamma=1.0;
m=0;

```

```

Trace=zeros (MaxGeneration,4);

[x1n,x2n,x3n,lightn]=init_ffa(n,range);%generating the initial
locations of n fireflies, [x1n x2n x3n] are respectively [l1 l2 r]
zn=lightn;

for i=1:MaxGeneration
    for j=1:length(x1n)
        zn(1,j)=-Complis(x1n(j),x2n(j),x3n(j));
    end %Complis is the objective function based on Appendix A

    [lightn,Index]=sort(zn);
    x1n=x1n(Index); x2n=x2n(Index); x3n=x3n(Index);
    x1o=x1n; x2o=x2n; x3o=x3n; lighto=lightn;
    m=m+1;

Trace(m,:)=[x1n(length(x1n)),x2n(length(x1n)),x3n(length(x1n)),li
ghtn(length(x1n))];

[x1n,x2n,x3n]=ffa_move(x1n,x2n,x3n,lightn,x1o,x2o,x3o,lighto,gamm
a,range); %ffa_move is a sub-function.

end
best=Trace;

```

### Firefly movement function:

```

function
[x1n,x2n,x3n]=ffa_move(x1n,x2n,x3n,lightn,x1o,x2o,x3o,lighto,gamm
a,range)

beta0=1;
alpha0=0.5;
theta=0.5;
ni=size(x1n,2); nj=size(x1o,2);

for i=1:ni
    for j=1:nj
        r=sqrt((x1n(i)-x1o(j))^2+(x2n(i)-x2o(j))^2+(x3n(i)-
x3o(j))^2);
        if lighto(j)>lightn(i)
            beta=beta0/(1+gamma*r^2);
            alpha=alpha0*theta^i;
            x1n(i)=x1n(i)+beta*(x1o(j)-x1n(i))+alpha*(rand-0.5);
            x2n(i)=x2n(i)+beta*(x2o(j)-x2n(i))+alpha*(rand-0.5);
            x3n(i)=x3n(i)+beta*(x3o(j)-x3n(i))+alpha*(rand-0.5);
        end
    end
end

```

```
end
[x1n,x2n,x3n]=findrange(x1n,x2n,x3n,range);
```

#### 4. Well-conditioned workspace optimization

##### Objective function:

```
function eta=Wkspace(l1,l2,r)

%x=[89.37,89,63],y=[89.37,89.63],z=[89.37,89.63]
a=89.37;
b=89.63;
num=5;
Idx=zeros(num^3,1);
rand('state',0);
x=a+(b-a)*rand(num,1);
y=a+(b-a)*rand(num,1);
z=a+(b-a)*rand(num,1);

m=0;
for i=1:length(z)
    X=x(i);
    for j=1:length(x)
        Y=y(j);
        for k=1:length(y)
            Z=z(k);
            m=m+1;
            Idx(m)=ConditionN(X,Y,Z,l1,l2,r);
        end
    end
end
end
s=sum(1./Idx);
eta=s*((b-a)*(b-a)*(b-a))/(num*num*num);
```

##### Sub-function of condition number computation:

```
function [idex]=ConditionN(x,y,z,l1,l2,r)

%%Calculation of Jacobian matrix
R=70+l1+l2;
B1=[x,y,z-r]';
B2=[x,y-r,z]';
B3=[x-r,y,z]';
A1=[R,R,0]';
A2=[R,0,R]';
A3=[0,R,R]';
```

```

ab1=B1-A1;
ab2=B2-A2;
ab3=B3-A3;

s1=ab1/norm(ab1);
s2=ab2/norm(ab2);
s3=ab3/norm(ab3);

b1=[0,0,-r]';
b2=[0,-r,0]';
b3=[-r,0,0]';

J=[s1',(cross(b1,s1))';%Here the micromanipulator keeps the
original orientation (0-0-0)
    s2',(cross(b2,s2))';
    s3',(cross(b3,s3))'];
idex=cond(J);

```

## 5. Main Program of Multi-objective Optimization

```

function firefly3(instr)

if nargin<1, instr=[80,20]; end
n=instr(1);%n is the number of fireflies.
MaxGeneration=instr(2);
rand('state',0);

range=[4,6,5,8,5,9];%range=[l1min l1max l2min l2max rmin rmax]

[x1n,x2n,x3n,zn]=init_ffa(n,range);%generating the initial
locations of n fireflies

for i=1:MaxGeneration
    k1=rand;
    k2=rand;
    w1=k1/(k1+k2);
    w2=k2/(k1+k2);
    for j=1:n
        zn(j)=-
(w1*Complis(x1n(j),x2n(j),x3n(j))*10^5)+w2*Wkspace(x1n(j),x2n(j),
x3n(j));
    end
    [light,Index]=sort(zn);
    x1n=x1n(Index);x2n=x2n(Index);x3n=x3n(Index);
    g1=x1n(n);g2=x2n(n);g3=x3n(n);
    x1o=x1n;x2o=x2n;x3o=x3n;
    for j=1:n
        zj(1)=Wkspace(x1o(j),x2o(j),x3o(j));
        zj(2)=- (Complis(x1o(j),x2o(j),x3o(j))*10^5);
    end
end

```

```

flag=0;
for k=1:n
    zk(1)=Wkspace(x1o(k),x2o(k),x3o(k));
    zk(2)=-(Complis(x1o(k),x2o(k),x3o(k))*10^5);
    %if light(k)>light(j)
    if zk(1)>zj(1)&&zk(2)>zj(2)

[x1o(j),x2o(j),x3o(j)]=ffa_move(x1o(j),x2o(j),x3o(j),...
    x1o(k),x2o(k),x3o(k),i,range);
        flag=1;
    end
end
if flag==0
    [x1n(j),x2n(j),x3n(j)]=ff_move(g1,g2,g3,i);
else x1n(j)=x1o(j);
    x2n(j)=x2o(j);
    x3n(j)=x3o(j);
end
end
end
fitnes=zeros(2,n);
for ii=1:n
    fitnes(1,ii)=-Complis(x1n(ii),x2n(ii),x3n(ii));
    fitnes(2,ii)=Wkspace(x1n(ii),x2n(ii),x3n(ii));
end
plot(fitnes(1,:),fitnes(2:,:), 'k.');
```

## B Table of Pareto Optimal Set

No.	$I_1$	$I_2$	$r$	Compliance	Global Condition Index
1	5.21545	5.31424	5.49962	-2.75165E-05	0.015736347
2	5.21818	5.31266	5.49975	-2.75163E-05	0.015736809
3	5.19618	5.32284	5.50173	-2.75185E-05	0.015726502
4	5.27347	5.34668	5.42803	-2.75060E-05	0.015909851
5	5.21818	5.31266	5.49975	-2.75163E-05	0.015736809
6	5.26179	5.68954	5.39519	-2.76546E-05	0.016156483
7	5.21818	5.31266	5.49975	-2.75163E-05	0.015736809
8	5.27858	5.34682	5.42502	-2.75055E-05	0.015917964
9	5.28047	5.3468	5.42384	-2.75052E-05	0.015921038
10	5.21818	5.31266	5.49975	-2.75163E-05	0.015736809
11	5.21818	5.31266	5.49975	-2.75163E-05	0.015736809
12	5.21545	5.31424	5.49962	-2.75165E-05	0.015736347
13	5.21818	5.31266	5.49975	-2.75163E-05	0.015736809
14	5.37969	5.98115	5.22682	-2.77320E-05	0.016659792
15	5.21818	5.31266	5.49975	-2.75163E-05	0.015736809
16	5.21545	5.31424	5.49962	-2.75165E-05	0.015736347
17	5.21545	5.31424	5.49962	-2.75165E-05	0.015736347
18	5.21545	5.31424	5.49962	-2.75165E-05	0.015736347
19	5.33824	5.98277	5.24985	-2.77374E-05	0.016601136
20	5.21818	5.31266	5.49975	-2.75163E-05	0.015736809
21	5.21818	5.31266	5.49975	-2.75163E-05	0.015736809
22	5.21818	5.31266	5.49975	-2.75163E-05	0.015736809
23	5.21818	5.31266	5.49975	-2.75163E-05	0.015736809
24	5.21818	5.31266	5.49975	-2.75163E-05	0.015736809
25	5.33824	5.98277	5.24985	-2.77374E-05	0.016601137
26	5.21545	5.31424	5.49962	-2.75165E-05	0.015736347
27	5.21545	5.31424	5.49962	-2.75165E-05	0.015736347
28	5.32148	6.53707	5.09135	-2.79265E-05	0.017132196
29	5.21545	5.31424	5.49962	-2.75165E-05	0.015736347
30	5.21818	5.31266	5.49975	-2.75163E-05	0.015736809
31	5.28047	5.3468	5.42384	-2.75052E-05	0.015921038
32	5.21545	5.31424	5.49962	-2.75165E-05	0.015736347
33	5.21818	5.31266	5.49975	-2.75163E-05	0.015736809
34	5.21818	5.31266	5.49975	-2.75163E-05	0.015736809
35	4.98112	7.75737	5.10838	-2.84855E-05	0.017512428
36	5.21818	5.31266	5.49975	-2.75163E-05	0.015736809
37	5.32159	6.53774	5.09126	-2.79268E-05	0.017132738
38	5.32234	7.68282	5.18759	-2.85490E-05	0.0175202
39	5.32166	6.53644	5.09132	-2.79262E-05	0.017132025
40	5.27858	5.34682	5.42502	-2.75055E-05	0.015917964

No.	$l_1$	$l_2$	$r$	Compliance	Global Condition Index
41	5.27858	5.34682	5.42502	-2.75055E-05	0.015917965
42	5.21545	5.31424	5.49962	-2.75165E-05	0.015736347
43	5.19645	5.32288	5.50152	-2.75185E-05	0.015727026
44	5.37974	5.98111	5.22673	-2.77320E-05	0.016659933
45	5.28047	5.3468	5.42384	-2.75052E-05	0.015921039
46	5.19618	5.32284	5.50173	-2.75185E-05	0.015726502
47	5.21818	5.31266	5.49975	-2.75163E-05	0.015736809
48	5.19644	5.32287	5.50154	-2.75185E-05	0.015726984
49	5.26181	5.68954	5.39518	-2.76546E-05	0.016156497
50	4.83666	7.7233	5.12078	-2.84496E-05	0.017430686
51	5.33214	5.34906	5.36036	-2.74831E-05	0.016059133
52	5.33214	5.34906	5.36036	-2.74831E-05	0.016059133
53	5.32242	6.51781	5.08939	-2.79161E-05	0.017125936
54	5.32242	6.51863	5.08913	-2.79164E-05	0.017126736
55	5.27454	6.89142	5.08415	-2.80903E-05	0.017294929
56	5.34775	6.77905	5.05073	-2.80300E-05	0.017323902
57	5.37983	5.96917	5.22341	-2.77245E-05	0.016658787
58	5.39148	5.95776	5.22534	-2.77218E-05	0.016655823
59	5.21547	5.31424	5.49961	-2.75165E-05	0.015736368
60	5.19645	5.32285	5.50156	-2.75185E-05	0.015726949
61	5.38507	5.9529	5.22783	-2.77196E-05	0.016645704
62	5.394	5.89212	5.24998	-2.77026E-05	0.016581712
63	5.28078	5.34674	5.42365	-2.75051E-05	0.015921504
64	5.27975	5.34625	5.42454	-2.75051E-05	0.015919133
65	5.19647	5.32284	5.50154	-2.75185E-05	0.015726991
66	5.21492	5.31461	5.49949	-2.75166E-05	0.015736467
67	5.19666	5.32283	5.50144	-2.75184E-05	0.015727263
68	5.21472	5.31501	5.49913	-2.75166E-05	0.015737202
69	5.43188	5.63231	5.30605	-2.76106E-05	0.016367086
70	5.33214	5.34906	5.36036	-2.74831E-05	0.016059133
71	5.21741	5.31439	5.49804	-2.75162E-05	0.015740255
72	5.33214	5.34906	5.36036	-2.74831E-05	0.016059133
73	5.35733	5.32766	5.38191	-2.74879E-05	0.016025001
74	5.31618	5.3132	5.41987	-2.74930E-05	0.015928952
75	5.37002	5.32064	5.37746	-2.74844E-05	0.016035758
76	5.31575	5.29669	5.43234	-2.74912E-05	0.015898096
77	5.37249	5.31656	5.38019	-2.74842E-05	0.016030224
78	5.34092	5.30403	5.40954	-2.74875E-05	0.01595538
79	5.37699	5.3167	5.3776	-2.74837E-05	0.016037261
80	5.33214	5.34906	5.36036	-2.74831E-05	0.016059133